



저작자표시-비영리-변경금지 2.0 대한민국

이용자는 아래의 조건을 따르는 경우에 한하여 자유롭게

- 이 저작물을 복제, 배포, 전송, 전시, 공연 및 방송할 수 있습니다.

다음과 같은 조건을 따라야 합니다:



저작자표시. 귀하는 원저작자를 표시하여야 합니다.



비영리. 귀하는 이 저작물을 영리 목적으로 이용할 수 없습니다.



변경금지. 귀하는 이 저작물을 개작, 변형 또는 가공할 수 없습니다.

- 귀하는, 이 저작물의 재이용이나 배포의 경우, 이 저작물에 적용된 이용허락조건을 명확하게 나타내어야 합니다.
- 저작권자로부터 별도의 허가를 받으면 이러한 조건들은 적용되지 않습니다.

저작권법에 따른 이용자의 권리는 위의 내용에 의하여 영향을 받지 않습니다.

이것은 [이용허락규약\(Legal Code\)](#)을 이해하기 쉽게 요약한 것입니다.

[Disclaimer](#)

공학박사 학위논문

A study on electrostatic soft ionic sensors  
and generators based on triboelectronics

정전발전 기반의 소프트한 이온성 센서  
및 발전 소자에 관한 연구

2021 년 2월

서울대학교 대학원

재료공학부

이 영 훈

A study on electrostatic soft ionic sensors  
and generators based on tribotronics

정전발전 기반의 소프트한 이온성 센서  
및 발전 소자에 관한 연구

지도교수 선 정 윤

이 논문을 공학박사 학위논문으로 제출함  
2020년 12월

서울대학교 대학원  
재료공학부  
이 영 훈

이영훈의 공학박사 학위논문을 인준함  
2020년 12월

위 원 장	_____	남 기 태
부 위 원 장	_____	선 정 윤
위 원	_____	최 인 석
위 원	_____	박 용 래
위 원	_____	최 덕 현



# Abstract

With rapidly growing attention to human-machine interfaces (HMIs), wearable devices have been attracted a great deal of interest. To boost progress in the field, a challenge is raised for devices to equip lightweight and compliant power supplies. Recently, self-powered devices by harvesting mechanical energy from human motions are considered to be an attractive approach to meet the growing need for a wearable and light weight power supply.

Triboelectric nanogenerators (TENGs), based on coupling effects of contact electrification and electrostatic induction, have been achieving rapid progress as a sustainable power source with various advantages of simple structure, low weight, and high energy conversion efficiency. However, TENGs still suffer from a lack of stretchability to be utilized as future wearable electronics and potentially broaden the range of its applications. Hydrogels, composed of hydrophilic polymer networks containing ample water, could help solve the challenges. Elastic solid structure and high ion solubility potentially enable hydrogels to act as soft ionic conductors in TENGs.

Here, we demonstrate that hydrogels are promising materials to be introduced into the field of tribotronics, resulting in maximizing the potential of TENGs and broadening the range of its applications. Feasibility of applying hydrogels as conducting layer in TENGs was investigated. Three soft ionic devices based on tribotronics were explored; transparent and deformable TENGs, soft ionic proximity sensors, and multi-functional ionic soft robots.

In first part, hydrogel based transparent and deformable TENGs were demonstrated by introducing hydrogels as ionic conductors into TENGs. In order to

reliably apply hydrogels as conducting layer of TENGs, issues of electrochemical reactions in hydrogels and relatively low hydrogel conductivity were studied. Working mechanism of the hydrogel based TENG was suggested in detail. Chemically anchoring hydrogels on dielectric elastomers ensured high deformability of the TENGs, resulting in easily applying the TENGs on human skin. Surface functionalization on the generator improved power generation and made the generator electrically and optically stable due to the self-cleaning effect. The attractive features open up exciting opportunities for TENGs as wearable electronics.

In second part, soft ionic proximity sensors were demonstrated based on tribotronics. While conventional proximity sensors have been suffered from lack of softness due to their working mechanism and structures, we suggest soft proximity sensors by applying hydrogels and tribotronics. Network of hydrogels in the sensor could detect the relative positions of nearby objects in a non-contact manner by comparing electric fields that originate from the objects. Electric field-based working mechanism allowed the sensors to equip the through-wall sensing capability. To accurately detect the relative position of an object, hydrogels were applied as shield layers to prevent electrical noise. The soft sensor is expected to expand the ways in which a person can perceive space by providing a new sensory modality that did not evolve naturally in human beings.

In third part, multi-functional ionic soft robots were demonstrated based on tribotronics. Working mechanisms of each function including adhesion, sensing, and vibrational cleaning, were studied in detail to combine the mutually complementary functions into a structure of TENGs without additional assembly. All of the functions could be realized based on a structure of TENGs without additional assembly. Thanks to high stretchability of ionic conductors, the robots could be expanded to

capture objects 68 times heavier than the robot. Adhesion capability of the robots was boosted by preventing from contamination using vibrational actuating and sensing capability. The approach pushes the boundaries of multi-functional robots in an attempt to combine mutually complementary functions into a single unit without modification of its simple structure.

**Keyword: tribotronics, hydrogels, soft ionics, soft robotics**

**Student Number: 2016-33811**

# Table of Contents

<b>Abstract</b> .....	i
<b>List of Figures</b> .....	ix
<b>Chapter 1. Introduction</b> .....	1
1.1. Research background.....	1
1.1.1. Tribotronics.....	1
1.1.2. Soft ionics .....	1
1.1.3. Hydrogels.....	2
1.1.4. Soft robotics.....	2
1.1.5. Goals and outline of this disseration.....	3
<b>Chapter 2. Transparent and deformable ionic communicators based on tribotronics</b> .....	5
2.1. Introduction.....	5
2.2. Experimental senction .....	7
2.2.1. Materials and specimen preparation.....	7

2.2.2. Fabrication of the hydrogel precursor solution.....	8
2.2.3. Fabrication of the STAICs.....	8
2.2.4. Wireless real-time communication .....	9
2.2.5. Characterization and measurement.....	9
2.3. Results and Discussion .....	11
2.3.1. Issues on hydrogel based TENGs.....	11
2.3.2. STAICs with high mechanical reliability .....	14
2.3.3. Triboelectric mechanism and characterization .....	20
2.3.4. STAICs with self-cleanability .....	28
2.3.5. Wireless real-time communications based on STAICs.....	34
2.4. Conclusion.....	38
<b>Chapter 3. Soft ionic proximity sensors.....</b>	<b>39</b>
3.1. Introduction.....	39
3.2. Experimental senction .....	42
3.2.1. Materials and specimen preparation.....	42
3.2.2. Preparation of hydrogel precursor solution .....	42

3.2.3. SIPS fabrication process.....	42
3.2.4. Mechanical testing.....	43
3.2.5. Characterization of sensing capability.....	43
3.2.6. Characterization of through-wall sensing capability .....	43
3.2.7. Demonstration of through-wall sensing capability.....	44
3.2.8. Demonstration of a wearable SIPS for spatial perception.....	44
3.3. Results and Discussion .....	45
3.3.1. Fabrication of a SIPS with high mechanical reliability.....	45
3.3.2. Sensing capability of the SIPS .....	49
3.3.3. Through-wall sensing capability of the SIPS .....	53
3.3.4. A wearable SIPS for spatial perception .....	58
3.4. Conclusion.....	63
<b>Chapter 4. Multi-functional ionic soft robots.....</b>	<b>64</b>
4.1. Introduction.....	64
4.2. Experimental senction .....	70
4.2.1. Materials and specimen preparation.....	71

4.2.2. Preparation of organogel precursor solution .....	71
4.2.3. Fabrication of ISWs.....	71
4.2.4. Characterization and measurement of electrostatic adhesion capturing.....	72
4.2.5. Demonstration of stretchable electrostatic adhesion net .....	72
4.2.6. Test of contamination .....	73
4.2.7. Characterization and measurement of electrostatic induction sensing .....	73
4.2.8. Characterization and measurement of electrostatic vibration cleaning.....	73
4.2.9. Recording of slingshot cleaning by a spider.....	74
4.3. Results and Discussion .....	74
4.3.1. Capturing by electrostatic adhesion.....	74
4.3.2. Sensing by electrostatic induction .....	82
4.3.3. Cleaning by electrostatic vibration.....	88
4.3.4. Multi-functional ionic spiderweb robots .....	93
4.4. Conclusion.....	95
<b>Chapter 5. Conclusion.....</b>	<b>96</b>

<b>Reference</b> .....	98
<b>Abstract in Korean</b> .....	106
<b>Curriculum Vitae</b> .....	113

# List of Figures

- Fig.2.1 **(a)** Equivalent circuit at equilibrium state. **(b)** Generated current and transmitted charges when a TENG is touched. **(c)** A schematic diagram showing interface between a hydrogel and an external Pt wire. **(d)** Equivalent circuit at transient state.
- Fig.2.2 Fabrication process of self-cleanable, transparent and attachable ionic communicators (STAICs).
- Fig. 2.3 **(a)** Cross-sectional structure of fabricated STAICs. Robust interfaces were formed between PDMS and hydrogel by applying chemical anchoring with benzophenone treatments. (Heptadecafluoro-1,1,2,2-tetrahydrodecyl)trichlorosilane (HDFS) coatings enhance triboelectric properties and provide self-cleaning ability. **(b)** X-ray photoelectron spectroscopy (XPS) analysis of HDFS-treated STAIC.
- Fig.2.4 **(a, b)** Fabricated STAIC was stretched with hands. **(c-g)** STAIC was subjected to different mechanical deformations sequentially and released. STAIC was rolled (c), folded (d), twisted (e), crumpled (f), and released from the deformations (g). (scale bar: 1 cm)
- Fig.2.5 **(a, b)** Transmittance spectra according to various weight ratio of thermal initiator (a) and accelerator (b) in STAIC. **(c)** Stress–strain curve of tensile test for a STAIC.
- Fig.2.6 Schematic diagram showing the electrical distribution and working mechanism of the STAIC. **(a)** Original status, **(b)** contact electrification to negative triboelectric charges on PDMS, and electrostatic induction during **(c)** detaching and **(d)** attaching of the counter material.
- Fig.2.7 Triboelectric performances were investigated with a pushing tester which can provide consistent contact area and speed.
- Fig.2.8 **(a)** Triboelectric series. **(b)** Output voltages from a STAIC when touched with different materials. **(c)** The effect of time interval between consecutive contacts on the electrical output performances and **(d)** averaged voltages. HDFS treatments for STAIC enhanced **(e)** 24.5% of output voltage and **(f)** 17.5% of output current. All error bars in the figure represent s.e.m. of the data.
- Fig.2.9 **(a)** Durability of a STAIC was tested for 25,600 cycles. **(b-d)** Anti-dehydration ability of a STAIC under a vacuum of 0.013 atm at room temperature. Normalized weight ratio of a STAIC and a hydrogel according to duration time (b). Triboelectric output voltages of STAICs before and after being placed under the vacuum for a week (c). Photographs showing contrasted extent of shrinkages of hydrogel and STAIC during the evaporation experiments (d). (scale bar: 1 cm)
- Fig.2.10 **(a)** Triboelectric outputs measured under 100%, 150% and 200% of applied tensile strain. **(b)** Triboelectric outputs were measured after 1,000 times of uniaxial stretching. 100%, 150% and 200% of strain were applied. **(c)** Effect of ion concentration on triboelectric outputs. **(d)** Output current density and output power density of a STAIC with various external loads. Electrical performance when

touching **(e)** outside and **(f)** inside of STAIC boundary which is attached on a touch screen. A STAIC was attached on top of a touch screen (this time, a resistive touch screen of an oscilloscope was used). A STAIC generated a voltage of 30 V when the screen was touched but did not hide the screen because the STAIC is highly transparent. All error bars in the figure represent s.e.m. of the data.

Fig.2.11 Self-cleanability of a STAIC. Static contact angles were observed for **(a)** non-treated surfaces and **(b)** HDFS treated surfaces. **(c)** Static contact angles were investigated for various plasma time. Advancing and receding contact angles measured with deionized water on **(d)** non-treated surfaces and **(e)** HDFS-treated surfaces. **(f)** Receding contact angle and **(g)** contact angle hysteresis were greatly influenced by HDFS treatments making the surface self-cleanable. **(h)** Transmittance of STAICs for a green visible light (550 nm). All error bars in the figure represent standard error of the mean of the data.

Fig.2.12 **(a)** Self-cleanability of HDFS-treated STAICs was explored by cleaning surfaces which were contaminated by activated charcoal powders. **(b, c)** Demonstration of self-cleanability of STAICs. Dust on HDFS-treated STAIC was removed easily by a water jet (scale bar: 1 cm).

Fig.2.13 **(a)** Contaminated areas and **(b)** average transmittances at 550 nm were measured according to the processes. Ten points on STAICs were randomly explored to calculate the average transmittance. **(c)** Output voltages of STAICs were investigated according to the cleaning processes. All error bars in the figure represent standard error of the mean of the data (scale bar: 1 cm).

Fig.2.14 **(a)** Measured output voltages and **(b)** averaged peak to peak voltages under humid conditions. All error bars in the figure represent s.e.m. of the data.

Fig.2.15 **(a)** STAICs were attached on the fingers and connected with wires to a controller board. A different order of a binary system was assigned to each finger, and the letters were pre-coded in the microcontroller. **(b)** Generated voltages of a STAIC by a gentle touch to a fabric and the skin.

Fig.2.16 **(a)** Block diagram of the communicator based on STAICs. STAICs were connected to a controller board which contains an RC low-pass filter, a microcontroller and a Wi-Fi module. **(b)** Demonstration of real-time communication with STAICs. "DREAM" was typed using combinations of finger touches.

Fig.3.1 **(a)** A wearable SIPS was developed to support human spatial perception in daily life. **(b, c)** The SIPS can identify the relative positions of nearby objects by comparing the intensity of the electric fields sensed by each hydrogel electric field receiver.

Fig.3.2 Conductive hydrogels were covalently anchored to an elastomer during 3D-printing for rapid and elaborate fabrication of a soft artificial electroreceptor (SIPS) with high mechanical reliability.

Fig.3.3 **(a)** In the absence of grafting agent activation, delamination occurs between the hydrogels and the elastomer during the printing process due to poor interfacial bonding. Scale bar, 250  $\mu\text{m}$ . **(b)** Grafting agent activation allows radicals in the elastomer to participate in free-radical polymerization of the hydrogel during printing, thus forming a tough interface between the hydrogel and elastomer layers.

(c) The SIPS was highly transparent to visible light of all colors because the rapidly fabricated hydrogel/elastomer interface scatters a negligible amount of visible light. Scale bar, 1 cm. (d, e) The hydrogel layer on the elastomer could be stretched more than 400% without delamination. To enhance the contrast between the hydrogel and elastomer, fluorescent dyes were added to the hydrogel. Scale bar, 1 cm.

Fig.3.4 (a, b) Schematic diagrams illustrating the sensing mechanism of the SIPS. An object will be charged due to contact electrification through contact with its surroundings (a). The electric fields originating from static charges on the surface of the object induce voltage in the hydrogel electric field receiver of the SIPS (b). Thus, by measuring the voltage across the external load connected between the receiver and ground, the intensity and polarity of the electric field can be estimated. (c) Pushing tester for vertical simple harmonic oscillation of the objects. The sensing capability of the SIPS was investigated with a pushing tester that provided vertical simple harmonic oscillation of the object. After cleaning, the object was charged by rubbing with the selected charging material. (d) The induced voltage closely traced the position of the object.

Fig.3.5 (a, b) The induced voltage was measured while varying the external load resistance (a) and oscillating frequency of the object (b). (c) Triboelectric series. The surface of a material can be positively or negatively charged after physical contact with other materials, due to contact electrification. Each material has a tendency to gain or lose electrons. Glass and PFA were selected as positively and negatively charged objects, respectively. (d) The induced voltage was measured while varying object and charging materials. (e) The induced voltage was measured while varying initial distance between the SIPS and the object. (f) Voltage induction in the SIPS according to hydrogel LiCl concentration. The sensing capability of the SIPS was insensitive to hydrogel LiCl concentration in the range of 2 mM to 2 M. The sensing capability of the SIPS was barely affected by ion concentration. Error bars represent SD (n=3).

Fig.3.6 (a) Schematic illustration of the mechanism of electric field transmission of a dielectric barrier. When an external electric field is applied, the dielectric becomes polarized and transmits the electric field, allowing the SIPS to detect an object behind the barrier. (b, c) The induced voltage was measured as the thickness (b) and relative permittivity (c) of the dielectric barrier were varied. Static electric fields have no effect on the sensing capability of the SIPS. Error bars represent SD (n=3).

Fig.3.7 (a) Schematic illustration of the mechanism of electric field shielding of a grounded conductor. An external electric field induces an accumulation of excess charges on the surface of the grounded conductor, preventing transmission of the electric field. (b) induced voltage was measured as the thickness of the hydrogel conductive shield was varied. (c) The lithium chloride (LiCl) concentration did not influence the shielding efficiency of the grounded hydrogel. Error bars represent SD (n=3).

Fig.3.8 (a, b) A SIPS with two hydrogel electric field receivers was placed in front of an oscillating pendulum. SIPSs can be used as proximity switches that can sense the presence of an object. (b) LEDs were programmed to be turned on when the induced voltages exceeded a threshold voltage (5 V). (c, d) A dielectric barrier was placed between the oscillating pendulum and the receiver on the left side. (d) The SIPS can be used to sense the presence of the object behind the dielectric barrier. (e, f) A conductive shield was placed between the oscillating pendulum and the receiver on the left side. (f) The conductive shield effectively blocked the transmission of the electric field originating from static charges on the surface of the pendulum. To

enhance the contrast between the hydrogels and background, fluorescent dyes were added to the hydrogel electric field receivers. Scale bar, 4cm.

Fig.3.9 **(a)** Without the conductive shield, the sensing capability of the SIPS shows anisotropy because of the data line connected to the electric field receiver. **(b)** When the data line is covered with a hydrogel conductive shield, the sensing capability of the SIPS shows isotropy. Error bars represent SD (n=3).

Fig.3.10 **(a)** The wearable SIPS was attached to the hollow of the hand. **(b, c)** Schematic describing each 3D-printed layer in a wearable SIPS. **(b)** Exploded view of the SIPS composed of hydrogels printed on elastomer layers. **(c)** A sensing layer with four hydrogel electric field receivers was sandwiched between two shielding layers. The bottom shielding layer blocks electrical noise from a hand and the top shielding layer prevents signal distortion by the data line. **(d)** By comparing the intensity of the electric fields sensed by each hydrogel receiver, the SIPS can be used to identify the relative position of the object. Error bars represent SD (n=3). Scale bar, 2 cm.

Fig.3.11 A wearable SIPS for spatial perception. **(a, b)** By wearing the SIPS, a person can perceive spatial information related to a static **(a)** and dynamic **(b)** object via auditory signals.

Fig.4.1 **(a)** Spiders can sense and clean using their webs alone, and these functions act synergistically to capture their prey. **(b)** Ionic spiderwebs (ISWs) emulating the capturing strategies of a spider.

Fig.4.2 ISWs emulating the optimized capturing strategies of spiders. Spiders have used their own unique capturing strategies. ISWs are made to emulate spider's outstanding capturing strategies.

Fig.4.3 **(a)** Schematic illustration describing the structural design of a fabricated ISW. **(b)** Magnified image of an ISW. Transparent organogel is encapsulated with translucent silicone rubber. Scale bar, 200  $\mu\text{m}$ . **(c)** Chemical structures of an ionically conductive organogel consisting of EG dissolving LiCl and PAAm chains cross-linked by MBAAm.

Fig.4.4 Fabrication process of an ISW. **(a-f)** Pre-stretched silicone tubes **(a)** were treated with air plasma **(b)** and released to obtain wrinkled surfaces **(c)**. Treated tubes were immersed in a solution with HDFS for self-assembly monolayer coating **(d)** [25]. Organogel precursor solution was injected into the tube **(e)** followed by 365 nm UV irradiation in inert condition for 5 minutes **(f)**. Scale bar, 1  $\mu\text{m}$ .

Fig.4.5 **(a)** Anti-dehydration capability of ISWs under harsh conditions. Organogel with a vapor pressure of 0.5 kPa evaporates relatively slower than hydrogel with a vapor pressure of 2.3 kPa [90]. Surface treatment prevented evaporation of organogel by lowering the vapor permittivity of silicone rubber [108]. **(b)** Exploded view of orb spiderwebs. Spiders spin adhesive, stretchable, and translucent capture thread on strong structural thread. **(c, d)** Stress-strain curve of tensile test. **(c)** Stiffness and extensibilities of nylon thread were 2.2 GPa and 0.21, respectively. **(d)** Stiffness and extensibilities of ISW were 640 kPa and 1.9, respectively. Error bars represent SD (n=3).

Fig.4.6 **(a-c)** Schematic diagrams illustrating the working mechanism of electrostatic adhesion capturing in the OFF-state ( $V_{\text{applied}} = 0$ ) (a) and ON-state ( $V_{\text{applied}} > 0$ ) (b) with a cross-sectional view (c). The electric field generated by the potential difference between a pair of ISWs induces polarization in a target, leading to electrostatic adhesion capture.

Fig.4.7 **(a)** Leakage current of ISW. In a wide range of LiCl concentrations from 0.15 mM to 1.5 M, there was insignificant leakage current. **(b)** Breakdown voltages of ISW. Maximum applied voltages that ISW can endure were measured. The average breakdown voltage was measured as 16.3 kV. **(c)** Dielectric breakdown behavior of ISW. When breakdown occurs, sudden increase of the leakage current causes the destruction of ISW. Therefore, leakage current was measured, so that the applied voltage could be shut down when increase of leakage current is detected.

Fig.4.8 **(a-c)** Adhesion force was investigated as a function of applied voltages (a), target materials (b), and ion concentrations in the organogel (c). Error bars in the figures represent SD ( $n = 5$ ).

Fig.4.9 **(a, b)** Adhesion force was investigated as tilt angle (a) and applied strain (b). **(c)** Four pairs of ISWs capturing a 6.8 g aluminum plate. When 50% strain was applied, the ISWs captured a 13.6 g aluminum plate. Error bars in the figures represent SD ( $n = 5$ ).

Fig.4.10 **(a)** Air circulation system that scatters dense dust to accelerate contamination. **(b)** Normalized electrostatic adhesion forces of ISWs after exposure to contaminants in the ON-state and OFF-state. **(c)** Contaminated surfaces of ISWs. Scale bar, 150  $\mu\text{m}$ . Error bars represent SD ( $n = 5$ ).

Fig.4.11 **(a, b)** Schematic diagrams showing the working mechanism of electrostatic induction sensing. **(c, d)** Schematic describing a detailed sensing mechanism (c) and graph of induced voltage over time (d). Even if charged objects exist around the ISW, they do not affect the sensing capability of ISW unless they move. **(e, f)** Experimental results describing the effect of static objects around the ISW. (e) Recovery time is the time required for the induced voltage to converge to zero after the approaching object stopped. (f) As the resistance of external load increased from 1 to 20 gigohm, recovery time increased from 2.5 to 37.9 s.

Fig.4.12 **(a)** A pushing tester providing consistent control of the moving speed and gap distance for electrostatic induction sensing. **(b)** Induced voltage in ISWs is investigated as a function of the gap distance between an ISW and a target. **(c, d)** Peak-to-peak voltages induced by a glass target were measured using an external load with resistance ranging from 1 megohm to 20 gigohms (c) and various charging materials (d). Error bars represent SD ( $n = 5$ ).

Fig.4.13 **(a)** A block diagram showing how the ISW senses the approach of a target and then interacts with a preprogrammed computer. **(b, c)** A green LED was turned on when the induced voltage exceeded a threshold voltage (0.1 V). Scale bar, 5 mm.

Fig.4.14 **(a-c)** Schematic diagrams showing the working mechanism of electrostatic vibration cleaning in the initial (a), attracted ( $V_{\text{applied}} > 0$ ) (b), and released ( $V_{\text{applied}} \rightarrow 0$ ) (c) states.

Fig.4.15 **(a)** To determine a resonant frequency of the ISW, the frequency of the applied voltage was swept from 20 to 116 Hz. **(b)** Resonant frequencies were measured using different length threads. **(c)** The adhesion force of a contaminated ISW was recovered as vibration cleaning removed contaminants. Error bars represent SDs,  $n = 5$ . Scale bar, 300  $\mu\text{m}$ . **(d)** An x-ray photoelectron spectrometer (XPS) was used to characterize the HDFs on surfaces of ISWs. **(e)** Wrinkles were formed on the surface of ISWs to enhance their hydrophobicity. Scale bar, 1  $\mu\text{m}$ . **(f)** Static contact angles depending on surface treatment. Error bars represent SDs,  $n = 3$ .

Fig.4.16 Cleaning capabilities of pristine and surface-treated ISWs. A droplet hanging on surface-treated ISWs was removed by vibration, whereas a droplet remained on the pristine ISWs.

Fig.4.17 Ionic spiderwebs. **(a, b)** ISW woven in the form of an orb web (a) and exploded view (b). Scale bar, 3 cm. **(c)** ISWs are passively camouflaged in a variety of environment such as a forest, fallen leaves, a brick wall, and the floor of a building. Scale bar, 4 cm. **(d)** An ISW is initially covered with dust (i). The dust is removed (ii). The ISW senses the approach of a target and then converted to capturing mode (iii). Leaf, PMMA, glass, and aluminum were sequentially captured by the ISW (iv). The targets were released from the ISW (v).

# Chapter 1. Introduction

## 1.1. Research background

### 1.1.1. Tribotronics

Tribotronics is a research field based on coupling the effects of contact electrification and electrostatic induction [1]. Tribotronics has been applied as a generator converting mechanical energy to electrical energy and a self-powered touch sensor. It has been achieving rapid progress as a sustainable power source with various advantages of simple structure (basically a couple of contact materials and electrodes), low weight, and high energy conversion efficiency [2] for use in practical devices. Since the first report in 2012 [3], there has been an explosive development for harvesting various types of mechanical energy from activities such as walking [4], talking [5], and typing [6] for wearable electronics.

### 1.1.2. Soft ionics

Soft ionics is a research field based on ionic conduction with soft materials. Especially, hydrogels have been spotlighted as soft materials for ionics. Under electric fields, ions in a hydrogel can be transported, which is called as ionic currents. Mobile ions dissolved in the water enable a hydrogel to act as an ionic conductor with a conductivity of up to  $\sim 10$  S/m [7]. Although a hydrogel has a higher resistivity than other soft electrical materials, the increases in electrical resistance with strain are orders of magnitude lower, because configuration changes in a polymer network rarely affect the migration of mobile ions [8]. Thus, hydrogels can be used as electrodes when a high degree of stretchability is required, such as in soft robots.

### 1.1.3. Hydrogels

Hydrogels are composed of water and hydrophilic polymer chains arranged in a network structure [7, 9, 10]. Cross-linked polymer chains render hydrogels into a three-dimensional elastic solid. The configuration of the polymer network can be adjusted so that it can endure mechanical strain of up to  $\sim 1,000\%$  [11]. The elastic modulus of hydrogels is in the range of 1-100 kPa, which is softer than that of other compliant materials, owing to the large volume fraction of water [9]. A hydrogel is biocompatible if its polymer network consists of non-toxic polymers [10]. Thus, hydrogels can be introduced into the field of soft robotics to broaden the range of biological applications. As with water, the transparency of a hydrogel is up to  $\sim 99\%$ , even in the bulk state, because the polymer network of the hydrogel absorbs a negligible amount of visible light [12]. This high degree of transparency allows optical information to be transmitted through a hydrogel. Since hydrogels can respond to diverse external stimuli via interactions between the polymer network and water, they endow soft robots with increased functionality [13, 14].

### 1.1.4. Soft robotics

Soft robotics is a research field dealing with robots composed of highly compliant materials. While rigid bodied robots are designed to efficiently carry out preplanned tasks in mostly industrial fields, soft robots are designed to compliantly handle unplanned tasks near people in daily life. The desire for compliant and safe robots has led to the development of soft robots [15]. Since the continuously deformable bodies of soft-bodied robots give them a high degree of freedom, they can flexibly handle irregular tasks in a less complicated manner than traditional robots. In addition, they can safely and comfortably interact with humans because

they are composed of compliant materials that have an elastic modulus similar to that of the soft tissues found in biological systems. Thus, there has been rapid progress in the development of compliant materials to meet the growing need for soft robots.

#### 1.1.5. Goals and outline of this dissertation

Purpose of this dissertation is introducing hydrogels into the field of tribotronics to maximize the potential of TENGs and broaden the range of its applications. This dissertation covers research on soft ionic devices based on tribotronics. This dissertation is composed of three parts.

In Chapter 2, Highly transparent (99.6%) and stretchable (330%) TENGs were developed by introducing hydrogels into TENGs. Working mechanism of the hydrogel based TENGs was suggested in detail. Potential issues of electrochemical reactions in hydrogels and relatively low hydrogel conductivity were investigated. The TENGs could be fabricated by chemically anchoring hydrogels on contact materials. To maintain high electrical output performance and high transmittance of the TENGs, self-cleaning effect was applied to the TENG. The TENGs served as a thimble-type human-machine communicator by harvesting gentle touches with fingers.

In Chapter 3, soft ionic proximity sensors based on tribotronics were demonstrated. Hydrogels in the sensor could detect the relative positions of nearby objects in a non-contact manner by sensing the electric fields that originate from the objects. To accurately detect the relative position of an object by comparing the voltage signals from networks of hydrogel electric field receivers, hydrogel shield layers were applied to prevent electrical noise. By wearing the sensors, a person could receive spatial information of a nearby object in real time via auditory signals.

In Chapter 4, multi-functional ionic soft robots were demonstrated based on tribotronics. Working mechanisms of each function including adhesion, sensing, and vibrational cleaning, were studied in detail to combine the mutually complementary functions into a single unit with a simple structure. A potential issue of electrochemical reactions in ionic conductors was investigated. All of the functions could be realized based on a structure of TENGs without additional assembly. Thanks to high stretchability of ionic conductors, the robots could be expanded to capture objects bigger than the robot. Furthermore, adhesion capability of the robots was boosted by vibrationally cleaning contamination and preventing contamination based on sensing capability.

# **Chapter 2. Transparent and deformable triboelectric nanogenerators**

## **2.1. Introduction**

With the advent of sensor networks at the interface between humans and machines [16], wireless and wearable/attachable electronics have emerged, including smart watch/glasses [17] or electronic/ionic skin that mimics the properties of human skin [18, 19]. Several challenges are raised for devices that are desired to become smaller/lighter, flexible/stretchable, and even transparent, while still requiring power sources. Batteries are the most commercialized portable power sources, but are relatively heavy and face critical lifetime limitations if they are made smaller or flexible [20]. As an alternative, harvesting mechanical energy from human motions is considered to be an attractive approach to meet the growing need for a wearable and lightweight power supply [21].

There have been extensive efforts to harvest mechanical energy based on piezoelectric, electromagnetic, and electrostatic effects [22]. Recently, triboelectric nanogenerators (TENGs), based on coupling the effects of contact electrification and electrostatic induction [23], have been achieving rapid progress as a sustainable power source with various advantages of simple structure (basically a couple of contact materials and electrodes), low weight, flexibility, and high energy conversion efficiency [24] for use in practical devices. Since the first report by Wang and colleagues in 2012 [25], there has been an explosive development for harvesting various types of mechanical energy from activities such as walking [26], talking [27], and typing [28] for wearable electronics. In addition, surface treatment, which is a key for maximizing contact electrification and higher output power, has enabled

TENGs to come close to commercialization [29]. Although there has been an increased interest in harvesting human motion without reducing degree of freedom (DOF) and transmittance, these applications have been struggling to provide both transmittance and stretchability due to the absence of proper electrodes. Using electrodes based on graphene [30], nanowire (NW) [31], and indium tin oxide (ITO) [32], there have been valuable efforts to increase both DOF and transmittance of TENGs for wearable electronics, but TENGs still suffer from a lack of stretchability and transmittance.

Hydrogels, which are the aggregation of crosslinked polymer networks in water [33], have been highlighted because of its promising properties such as biocompatibility [34], solubility [35], and so on. Specifically, a recent research by Sun and colleagues has greatly broadened the applications of hydrogel with extraordinary mechanical [36], optical, and electrical [37] properties, enabling its application to new functions, such as electrodes, actuators [37], and sensors [38]. These fascinating properties make hydrogels a promising material type for various research fields.

Here, hydrogel based transparent and deformable TENGs were demonstrated by introducing hydrogels as ionic conductors into TENGs. In order to reliably apply hydrogels as conducting layer of TENGs, issues of electrochemical reactions in hydrogels and relatively low hydrogel conductivity were investigated. Working mechanism of the hydrogel based TENG was suggested in detail. we secure the robust adhesion by chemical bonding between the contact material polydimethylsiloxane (PDMS) and hydrogel, which is the electrode with benzophenone treatments. Without sacrificing output performance and the transmittance, functionalization with (heptadecafluoro-1,1,2,2-tetrahydrodecyl)

trichlorosilane (HDFS) ensures that the contact surface, which could otherwise become contaminated, is clean. In addition, in order to acquire both transparency and strong chemical bonding, we have investigated the relationship between the gelation time on the elastomer and the interface transmittance during chemically strong bonding. We further explore applications for not only harvesting finger touches for electricity but also for self-cleanable, transparent, and attachable ionic communicators (STAICs). Combination of touches of five fingers with thimble-type STAICs can express words to wireless electronics.

## **2.2. Experimental section**

### **2.2.1. Materials and specimen preparation.**

Unless otherwise indicated, the STAICs were made using lithium chloride-containing polyacrylamide hydrogel as the primary material. PDMS (Dow corning, MS-1003) was used as the contact material. Acrylamide (AAM; Sigma, A8887) and lithium chloride (LiCl; sigma, L4408) were used as base materials for the hydrogel and the ionic charge carrier. N,N-methylenebisacrylamide (MBAA; Sigma, M7279) was used as the cross-linking agent for the AAm gel. APS (Sigma, A9164) and N,N,N',N'-tetramethylethylenediamine (TEMED; Sigma, T7024) were used as the photoinitiator and accelerator for the gelation reactions, respectively. (Heptadecafluoro-1,1,2,2-tetrahydrodecyl)trichlorosilane (HDFS; JSI Silicone Co., H5060.1) was used as the surface fluorination agent. Activated charcoal (Sigma, 242276) was used as artificial dust. VHB 4910 (3 M) was used as the double-sided tape. A Pt electrode was used for the measurement of STAICs electrical characteristic and Ag coated Cu wire was used for the electrical circuit. Dog-bone-shaped

specimens were cut with a laser cutting system (ULS, VLS 3.50) with the dimensions suggested by the ISO 37-4 standard for measuring stretchability.

### 2.2.2. Fabrication of the hydrogel precursor solution.

Unless otherwise indicated, the ionic hydrogel was synthesized by dissolving AAm monomer and LiCl in DI water. The molar concentrations of AAm and LiCl aqueous solutions were 4 and 16M for all experiments. 0.05 wt% of the cross-linker MBAA, 0.7 wt% of the initiator APS and 0.35 wt% of the accelerator TEMED, with respect to the weight of the AAm monomer, were mixed and degassed.

### 2.2.3. Fabrication of the STAICs

PDMS (Dow corning, MS-1003) was prepared by molding the mixture of base and curing agents (5:1 by weight) followed with a 50° C treatment in an oven for 24 hours. Bottom PDMS was shaped with the wall near the rim with the dimensions of 0.5 mm and 1.0 mm (height × thickness) on 0.5 mm × 40 mm × 40 mm (height × length × width) and top PDMS was shaped with dimensions of 0.1 mm × 40 mm × 40 mm (width × length × thickness). We used acrylic as templates. The cured PDMS was dipped in 15 wt% benzophenone in ethanol solution for 10 min and cleaned with methanol to activate the elastomer surfaces [39]. To bond between the edges of top and bottom PDMS, the edges of bottom and top PDMSs were treated with air plasma for 10 s. The area that did not need to be treated was masked with a polyimide tape. Hydrogel solution was poured on the activated bottom PDMS and covered with top PDMS. Hydrogel forms chemical bond to the PDMSs by directly curing hydrogel precursor onto the benzophenone absorbed PDMS surfaces followed by 365 nm UV irradiation for an hour. The top STAIC surface was treated by air plasma for 30 s. Reactive oxygen radicals produced by air plasma attack the methyl groups (Si-CH<sub>3</sub>) and substitutes them with silanol groups (Si-OH). A small

amount of HDFS (JSI Silicone Co. Korea) dissolved in hexane (1:3) and OH-terminated STAICs were placed into the glass container, and then heated at 40 °C in an oven for 90 min. A self-assembled monolayer (SAM) was formed via the vapor. A Pt electrode was inserted through capsulated PDMS to the hydrogel to measure electrical characteristic of STAICs.

#### 2.2.4. Wireless real-time communication.

Prepared STAICs on transparent double-sided tape (Very High Bond; 3M, 4910) were attached on each finger. Each wire from the STAICs was connected to the low-pass RC filter; 10M ohm resistor and 1 nF capacitor were used. Through the low-pass RC filter, it was connected to a channel of the microcontroller (Arduino uno, Arduino Co) with a Wi-Fi shield (SOLLAE SYSTEMS Co, PHPoC). The microcontroller and the Wi-Fi shield were connected to a battery. The microcontroller was wirelessly connected to a computer (Microsoft, Surface Pro4).

#### 2.2.5. Characterization and measurement.

The electrical voltage and current of STAICs were measured by using an oscilloscope (1 M $\Omega$ , MDO3052, Tektronix) with a voltage probe (40 M $\Omega$ , TPP0850, Tektronix) and a low-noise current preamplifier (Stanford research systems, SR570), respectively. A pushing tester (Junil Tech, JIPT-100) was used to create vertical compressive force with an aluminum plate as a contact material. All tests were performed under the pressure of 37.5 kPa, a gap of 13 mm, and a frequency of 4 Hz. All measurements were performed after about 1,000 pre-contacts to obtain a stable electric signal and were performed at room temperature. Impedance was measured using a Precision LCR Meter (Agilent, E4980A) (under input 1 V and 1 MHz). For the tensile test, a universal-testing-machine (Instron, 3343) was used, with the strain rate fixed at 60 mm/min. Cyclic stretching was performed during 1,000 cycles (Z-

tec, ZBT-300). The optical transmittance, of which reflectance was not considered, in the 300–800 nm range was measured by UV–vis spectroscopy (Agilent, Cary-60). Unless otherwise indicated, surface activation to form hydroxyl terminated of PDMS surfaces was performed with a plasma processing system (FEMTO SCIENCE, COVANCE-1MPR) under 200 W, 30 s, 15 sccm after rinsing with ethanol followed by N<sub>2</sub> blow drying. The contact angles between 10 µL drops of high-purity water and STAICs were measured using a contact angle analyzer (FEMTOFAB, Smart Drop) at room temperature. The average values of three measurements at different positions of the sample were used. For qualitative estimation of SAMs on STAICs, XPS data were monitored (KRATOS, AXIS-HSi). For analysis of the contamination area of the STAICs, an image processing program (ImageJ) was used.

## 2.3. Results and Discussion

### 2.3.1. Issues on hydrogel based TENGs

To utilize hydrogels as conducting layer of TENGs, two possible issue might be considered, which are electrochemical reaction and relatively low conductivity of hydrogels.

To investigate electrochemical reaction in hydrogels, equivalent circuit of the STAIC is described in Fig. 2.1a-c. At equilibrium state, voltage generated by static charges on dielectric layer is carried entirely by the two electrical double layer (EDL) and dielectric layer,  $V_t = V_D + V_{EDL}$ , where  $V_D$  is the voltage across dielectrics and  $V_{EDL}$  is the voltage across EDL. According to the generated voltage, the both capacitors meet the same amount of charge,  $C_D V_D = C_{EDL} V_{EDL}$ , where  $C_D$  and  $C_{EDL}$  are capacitance of dielectric layer and EDL, respectively. Commonly, thickness of TENG dielectric layer is hundreds of micrometers and distance between ion and electron at EDL is less than 1 nm, which resulting in relatively quite low capacitance of dielectric layer and high capacitance of EDL. In addition,  $V_{EDL}$  can be calculated experimentally. When a fabricated TENG was contacted, the amount of transferred charge was about 54.8 nC. Considering capacitance of EDL at an inserted wire into hydrogel is about 0.8 uF,  $V_{EDL}$  is quite less than 0.1 V. Thus, it is expected that voltage across the EDL can be within electrochemical window.

To investigate effect of relatively low hydrogel conductivity on output performance of TENGs, equivalent circuit of the STAIC is described in Fig. 2.1d. At transient state, voltage induced by a charged object is carried entirely by the two hydrogel and external load,  $V_t = V_{gel} + V_{load}$ , where  $V_{gel}$  is the voltage across the hydrogel and  $V_{load}$  is the voltage across the external load. Voltage across the external load, or generated voltage, would be affected by the hydrogel resistance if resistance of the hydrogel is similar scale to that of the external load, However, resistance of a hydrogel was 360  $\Omega$ –22 k $\Omega$  (the size of a sample was 150 mm  $\times$  20

mm × 3 mm) [38] and resistance of external load used in research field of TENGs is from a few MΩ to GΩ. Thus, it is expected that relatively low hydrogel conductivity makes neglectable effects on voltage across the external load. It will be discussed in detail later.

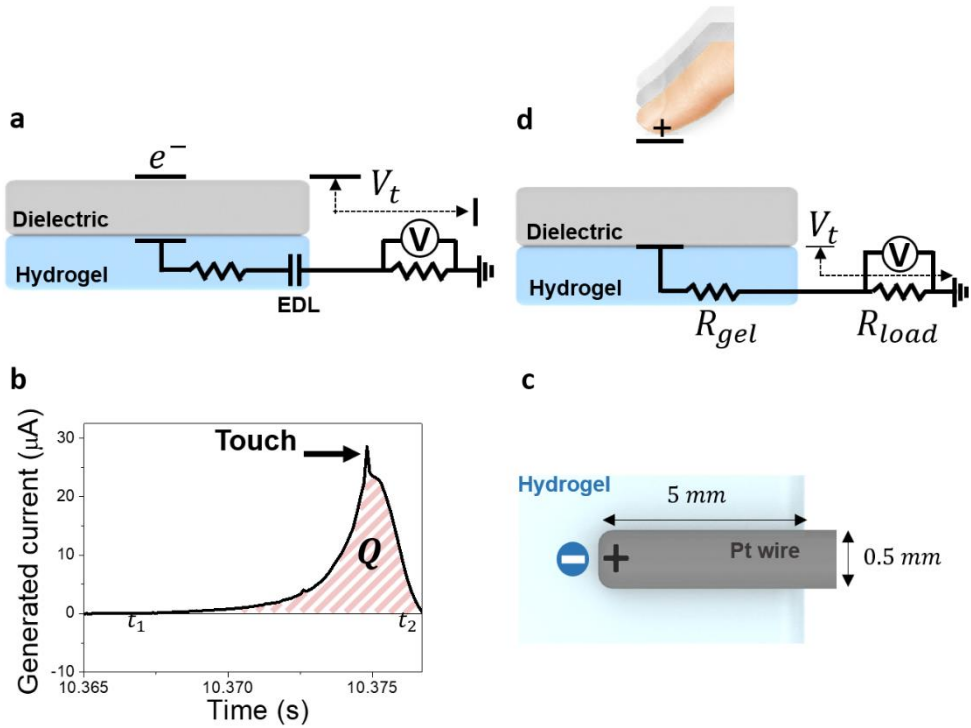


Fig. 2.1 (a) Equivalent circuit at equilibrium state. (b) Generated current and transmitted charges when a TENG is touched. (c) A schematic diagram showing interface between a hydrogel and an external Pt wire. (d) Equivalent circuit at transient state.

### 2.3.2. STAICs with high mechanical reliability

PDMS and hydrogel have extremely different affinities to water, resulting in weak physical bonding [40]. A mismatch of Young's modulus can cause defects between layers. For high reliability, it is essential to chemically anchor these to each other. We explored mechanically stable STAICs that are chemically bonded between the hydrogel and the contact material for high reliability. By applying benzophenone treatment shown in Fig. 2.2, we ensured that the hydrogel is covalently and robustly anchored to the elastomer, as shown in Fig. 2.2 (see Experimental section for details). Also, in order to maximize contact electrifications [29, 41, 42] resulting in high output power, many researchers have investigated the effects of physical surface treatment, such as nano/microstructure. However, this led to a decrease of transmittance [29] and durability [41] because of diffused reflection and wear, respectively. Thus, not only should the contact electrification be maximized, but also the transmittance. By using an HDFS chemical surface treatment, we formulated an approach to meet both of these requirements. The schematics for the fabricated STAICs are shown in Fig. 2.3a (see Experimental section for details of the fabrication steps). Perfluorination also helps to reduce reflectance of the surface [43]. Surface fluorination on STAICs by HDFS treatment, as shown in Fig. 2.3b, affects both the self-cleaning ability and stable electrical output power, which will be discussed later. Together with the non-treated STAICs surface used as a comparison, the functionalized STAICs were characterized by X-ray photoelectron spectroscopy (XPS) in order to elucidate the elemental compositions. As shown in Fig. 2.3b, a strong electron peak from the fluorine 1s orbital confirms the presence of fluorine on the STAICs, unlike for the non-treated STAICs. As shown in Fig. 2.4, the STAICs are not only stretchable, but can also be rolled, folded, twisted, and crumpled without

any mechanical failure, which illustrates a high stretchability and softness. Furthermore, due to the chemical anchoring between benzophenone-treated PDMS and hydrogel, no delamination was observed during mechanical tests as shown in Fig. 2.4g. However, this chemical bonding exhibits a challenging side effect of becoming opaque at the chemically bonded interface between PDMS and hydrogel. One possible reason for this is that the high oxygen content included in the porous elastomer disturbs the gelation of hydrogel on PDMS. We provide the simple solution by controlling the gelation time to minimize the effect of oxygen. Fig. 2.5a,b distinctly show the difference in the transmittance as a function of the concentration of ammonium persulfate (APS) used as the thermal initiator and N,N,N',N'-tetramethylethylenediamine (TEMED) as the crosslinking accelerator, which easily controls the gelation time, resulting in a transmittance difference. An increase in APS concentration by 0.1wt%, 0.3wt%, 0.5wt%, and 0.8wt% led to an increase in transmittance at 550 nm by 30.2%, 55.8%, 95.2%, and 99.6%, respectively. It is simple but a vital point for ensuring transmittance and a mechanically reliable, chemically anchored hydrogel–elastomer hybrid system. Although there are various types of PDMS, Sylgard-184 polymer has been widely used in the TENG field. However, Sylgard-184 has limited stretchability, up to 160% [44, 45]. Therefore, we have used MS-1003 to enhance the stretchability up to 330% without sacrificing transmittance of STAICs. As-prepared STAICs were cut into dog-bone shapes (insets of Fig. 2.5c) by using a laser cutter for tensile testing. The typical nominal stress and strain curves are shown in Fig. 2.5c. Young's modulus of 238.8 kPa and a strain of 3.3 make STAICs attractive attachable devices.

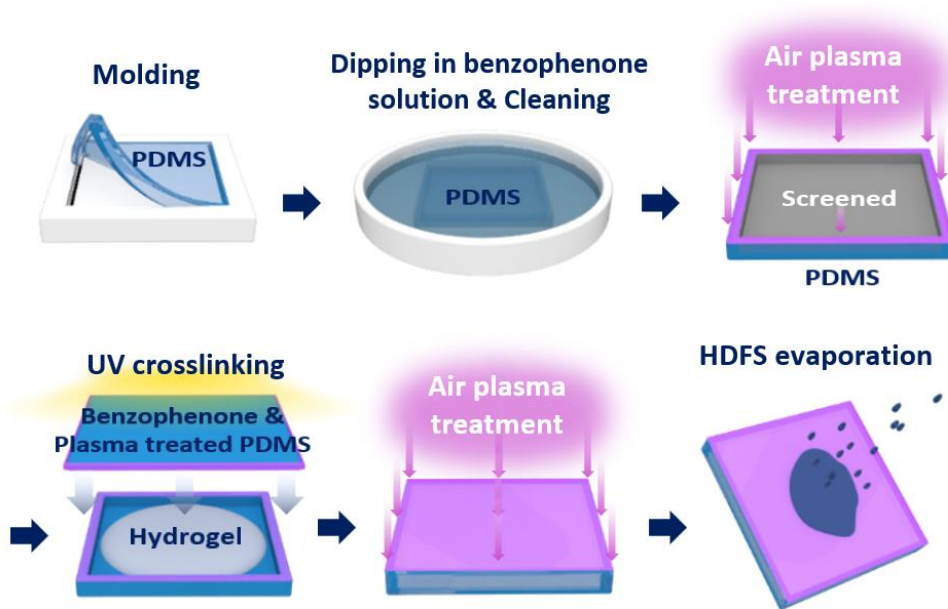


Fig. 2.2 Fabrication process of self-cleanable, transparent and attachable ionic communicators (STAICs).

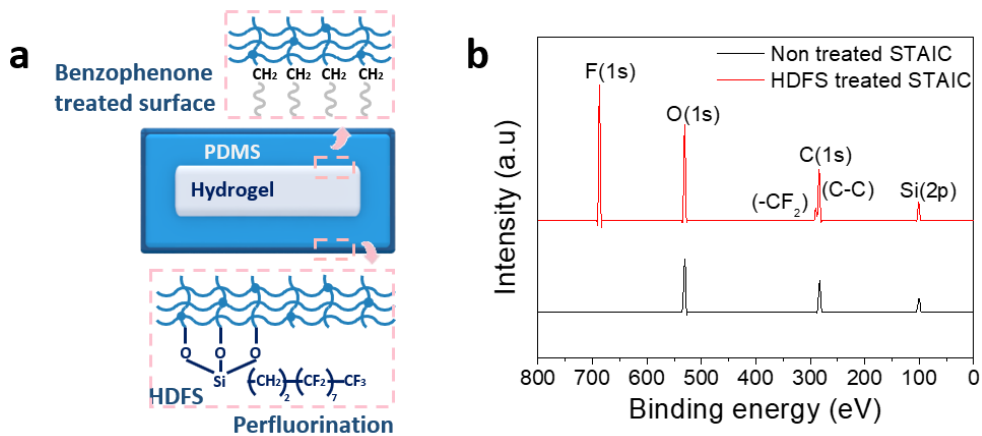


Fig. 2.3 **(a)** Cross-sectional structure of fabricated STAICs. Robust interfaces were formed between PDMS and hydrogel by applying chemical anchoring with benzophenone treatments. (Heptadecafluoro-1,1,2,2-tetrahydrodecyl)trichlorosilane (HDFS) coatings enhance triboelectric properties and provide self-cleaning ability. **(b)** X-ray photoelectron spectroscopy (XPS) analysis of HDFS-treated STAIC.

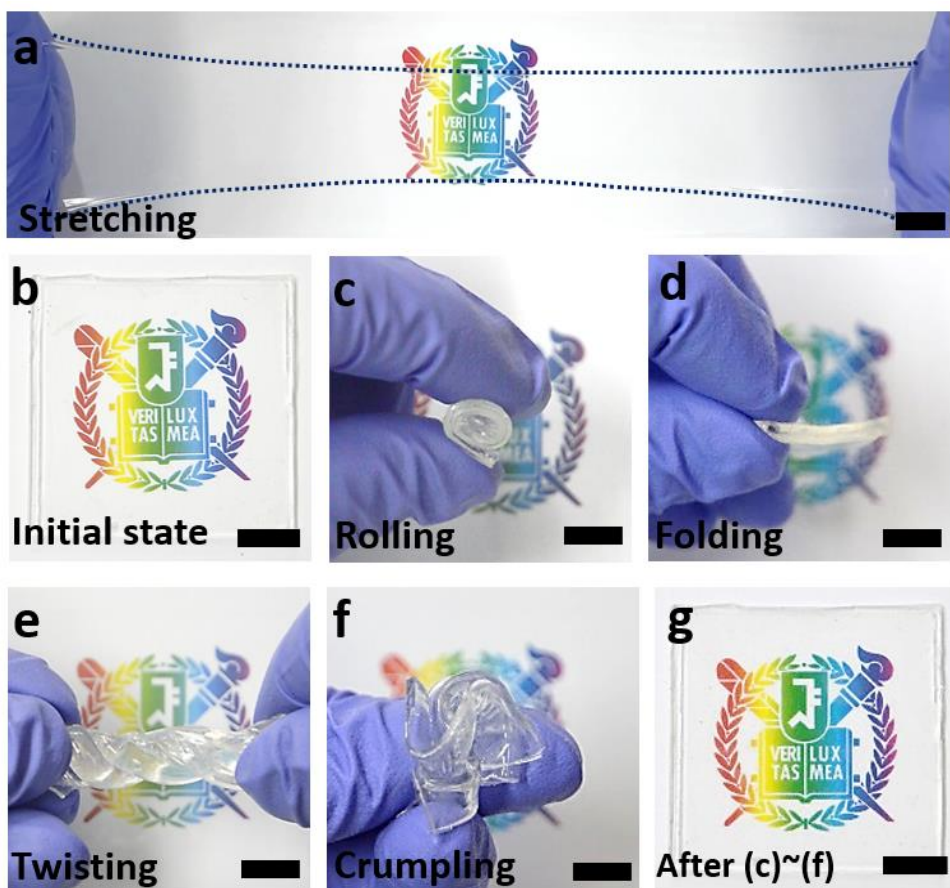


Fig. 2.4 (a, b) Fabricated STAIC was stretched with hands. (c-g) STAIC was subjected to different mechanical deformations sequentially and released. STAIC was rolled (c), folded (d), twisted (e), crumpled (f), and released from the deformations (g). (scale bar: 1 cm)

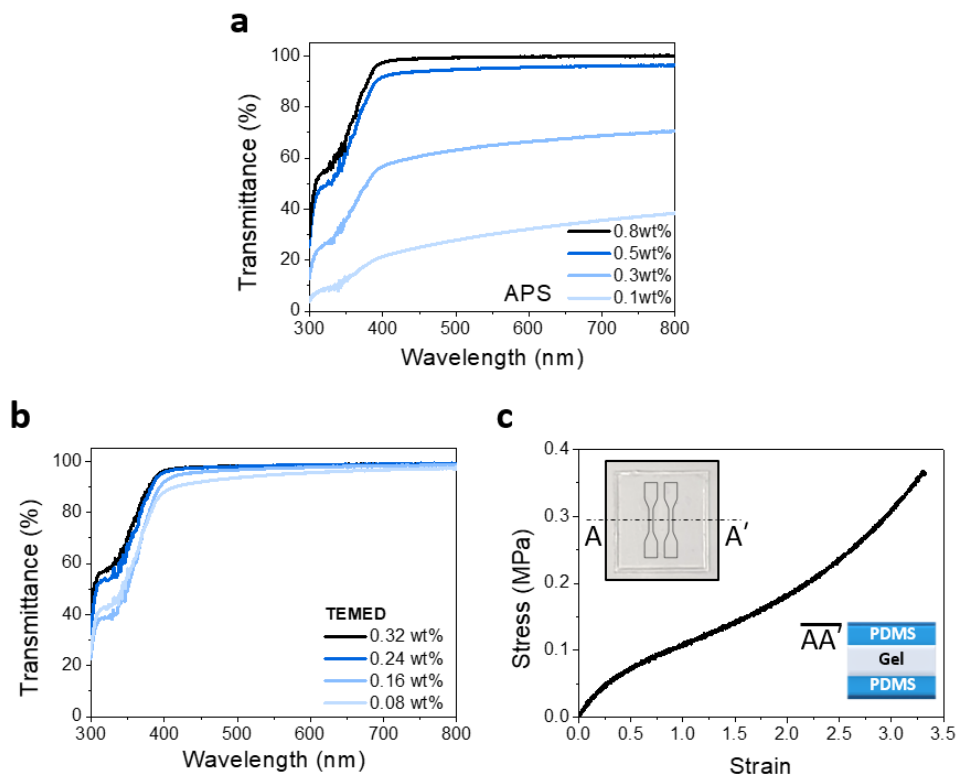


Fig. 2.5 Transmittance spectra according to various weight ratio of (a) thermal initiator and (b) accelerator in STAIC. (c) Stress-strain curve of tensile test for a STAIC.

### 2.3.3. Triboelectric mechanism and characterization.

STAICs are operated based on contact electrification and electrostatic induction. Figure 2.6 shows operational mechanism of STAICs. In the initial state, there is no electric potential between the STAIC and the counter object prior to the contact between them (Fig. 2.6a). When the counter object encounters the STAIC, contact electrification occurs between them because of their relatively different electron affinities (Fig. 2.6b). When detaching, transferred charges on the contact surface attract the positive ions and repel the negative ions, which repels the electrons of inserted Pt wire due to electrical equilibrium; here, the ions in the hydrogel act as a medium. Meanwhile, the counter object obtains electron from the ground (Fig. 2.6c). After full separation, the attaching counter object makes the electron flow back in the reverse direction by electrostatic induction. Meanwhile, the counter object repel electron to the ground, enhancing the output power by helping electrostatic induction of the STAIC (Fig. 2.6d). This mechanism shows that the hydrogel can be used in tribotronics as an ionic conductor, and that our system provides good contact materials for achieving reliable and high electrical output power.

Fig. 2.7 shows the experimental process for electrical output performance. We chose an aluminum plate as a contact material. Different contact materials were investigated, as shown in Fig. 2.8a,b. Larger difference between electron affinities of contact materials led to higher triboelectric voltage outputs. In addition, the effect of time interval between consecutive contacts on the electrical output performance was investigated (Fig. 2.8c,d). Longer duration time after detachment caused lower output voltages, which comes from charge leakage. Fig. 2.8e,f show the electrical output performance depending on existence of HDFS treatment on STAICs. 24.5%

of output voltage and 17.5% of output current were increased, which is possibly due to the fluorine layer that was formed by HDFs and had larger electron binding energy than PDMS [46]. Surface modification by HDFs also protects contact surfaces from contamination during multiple instances of contact, resulting in stable electrical outputs. Notably, STAICs showed very stable outputs over 25,600 cycles as shown in Fig. 2.9a. Figure 2.9b-d show that STAICs have good anti-dehydration ability under harsh conditions relative to the bare hydrogel due to the outer coating of PDMS. Bare hydrogel noticeably shrinks after 3 h in a desiccator and its weight decreases by 72.5%, while that of the STAIC decreases by only 2.8%. Electrical outputs of the STAICs were examined under various uniaxial strains as shown in Fig. 2.10a. When 200% of strain was applied, the output voltages slightly increased from 252 to 277 V because of the reduced distance between the charged surface and the electrode. Degradations in electrical outputs by mechanical fatigues were tested after being strained 1,000 times with strains of 100%, 150%, and 200% (Fig.2.10b). The STAICs did not show any degradation in electrical output by mechanical fatigues. Resistance may be an issue for the use of hydrogel as an electrode of TENGs. Fig. 2.10c shows the effect of LiCl concentration on triboelectric performance. The results show that there were no significant electrical output changes caused by the change of LiCl concentration. The resistance of hydrogel which contains 0.01–1 M of LiCl has been reported in the previous paper [38], and the resistance was 360  $\Omega$ –22 k $\Omega$  (the size of a sample was 150 mm  $\times$  20 mm  $\times$  3 mm). Inherent impedance of STAICs can be calculated by Thévenin's theorem. To obtain a maximum power transfer point and estimate inherent impedance of STAICs, we varied external load. As shown in Fig. 2.10d, the output current decreased as the external resistance increased up to 1 G $\Omega$ . As a result, the maximum power density (4.22 W/m<sup>2</sup>) was

obtained with an external load of 13 M $\Omega$ . The maximum power transfer happens when the external load is the same with inherent impedance of STAICs, so we can conclude that the inherent impedance of STAICs is 13 M $\Omega$ . Since this inherent impedance of the STAIC is much higher than the impedance of hydrogel, the performances of the STAICs were not influenced by the concentration of LiCl in the hydrogel. High transparency of STAICs allows the electrical power to be generated, without impeding the optical information. We have demonstrated the need for transparency by attaching a STAIC on top of a touch screen (Fig. 2.10e,f). A STAIC generated electrical power when the screen was touched, but did not hide the screen because the STAIC is highly transparent.

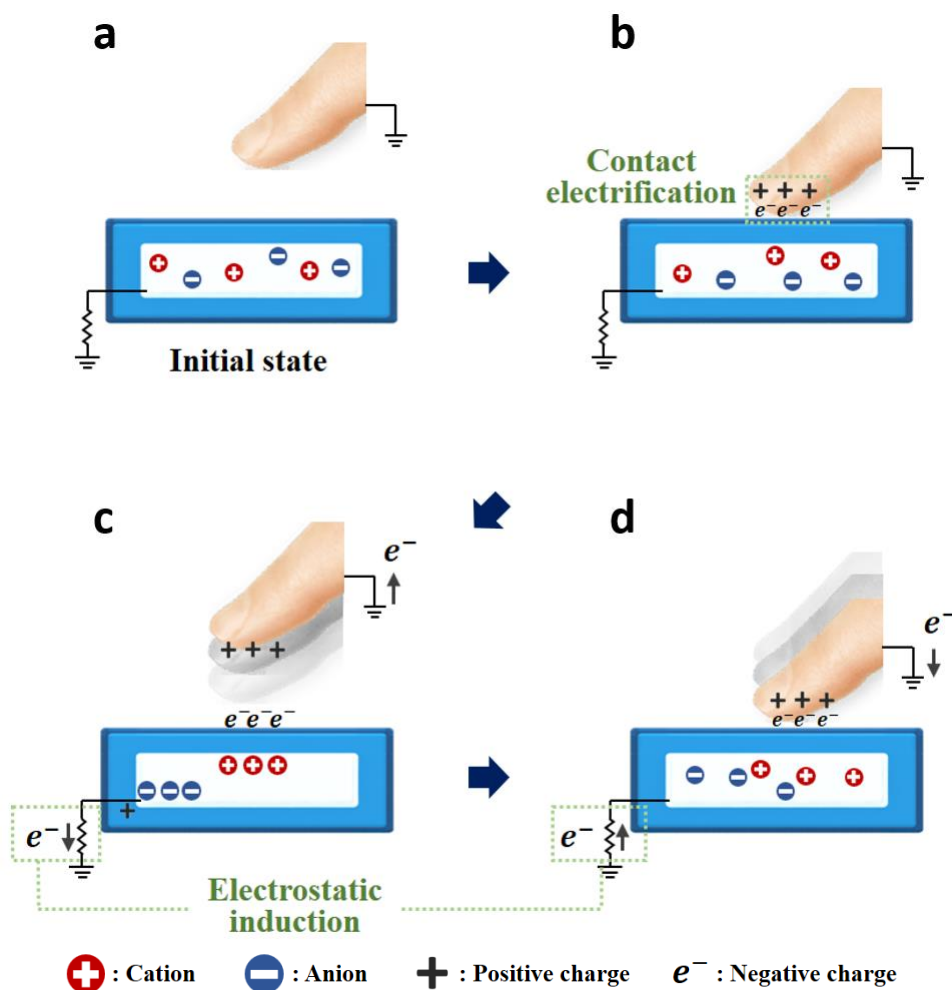


Fig. 2.6 Schematic diagram showing the electrical distribution and working mechanism of the STAIC. (a) Original status, (b) contact electrification to negative triboelectric charges on PDMS, and electrostatic induction during (c) detaching and (d) attaching of the counter material.

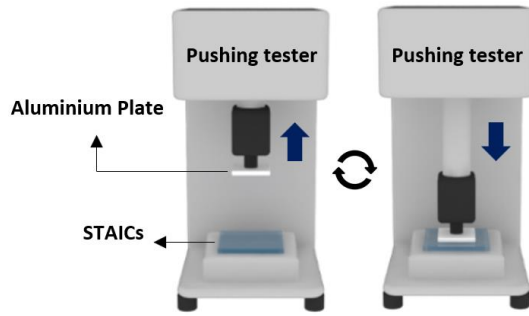


Fig. 2.7 Triboelectric performances were investigated with a pushing tester which can provide consistent contact area and speed.

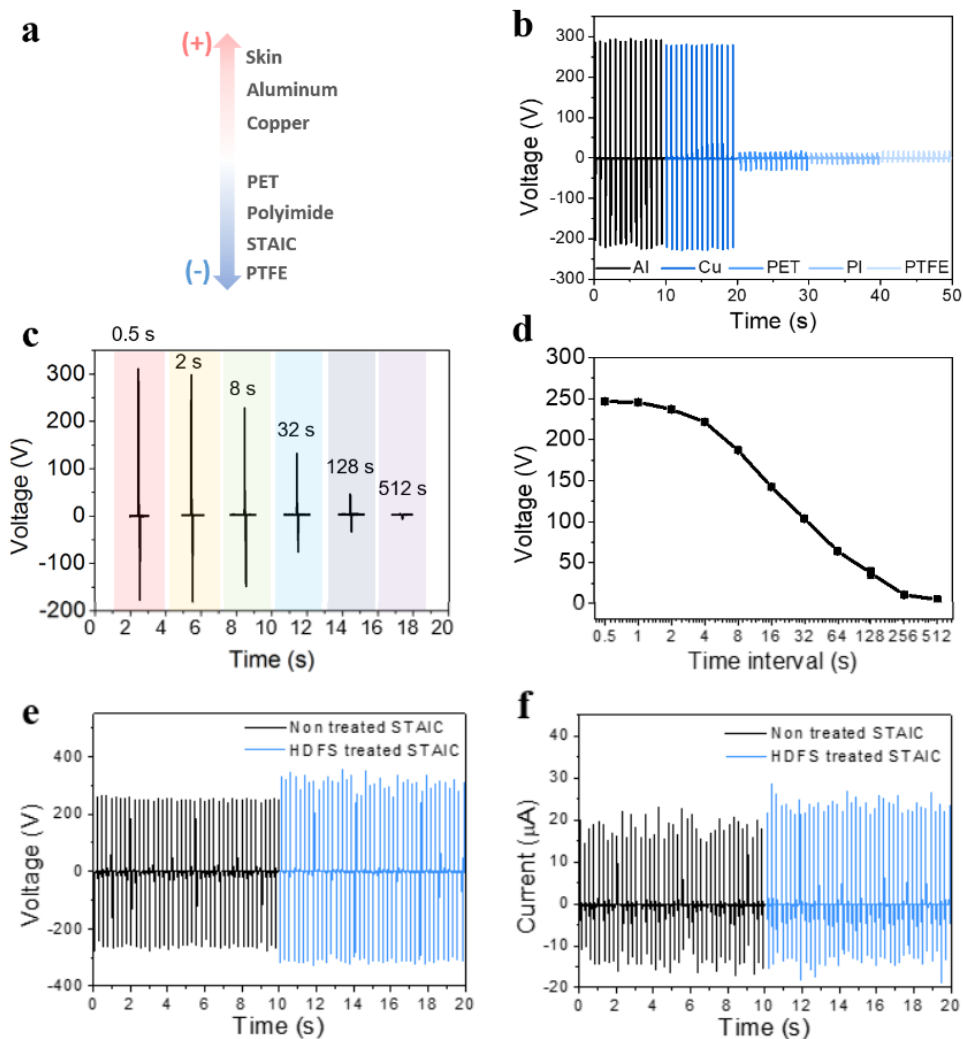


Fig. 2.8 (a) Triboelectric series. (b) Output voltages from a STAIC when touched with different materials. (c) The effect of time interval between consecutive contacts on the electrical output performances and (d) averaged voltages. HDFS treatments for STAIC enhanced (e) 24.5% of output voltage and (f) 17.5% of output current. All error bars in the figure represent s.e.m. of the data.

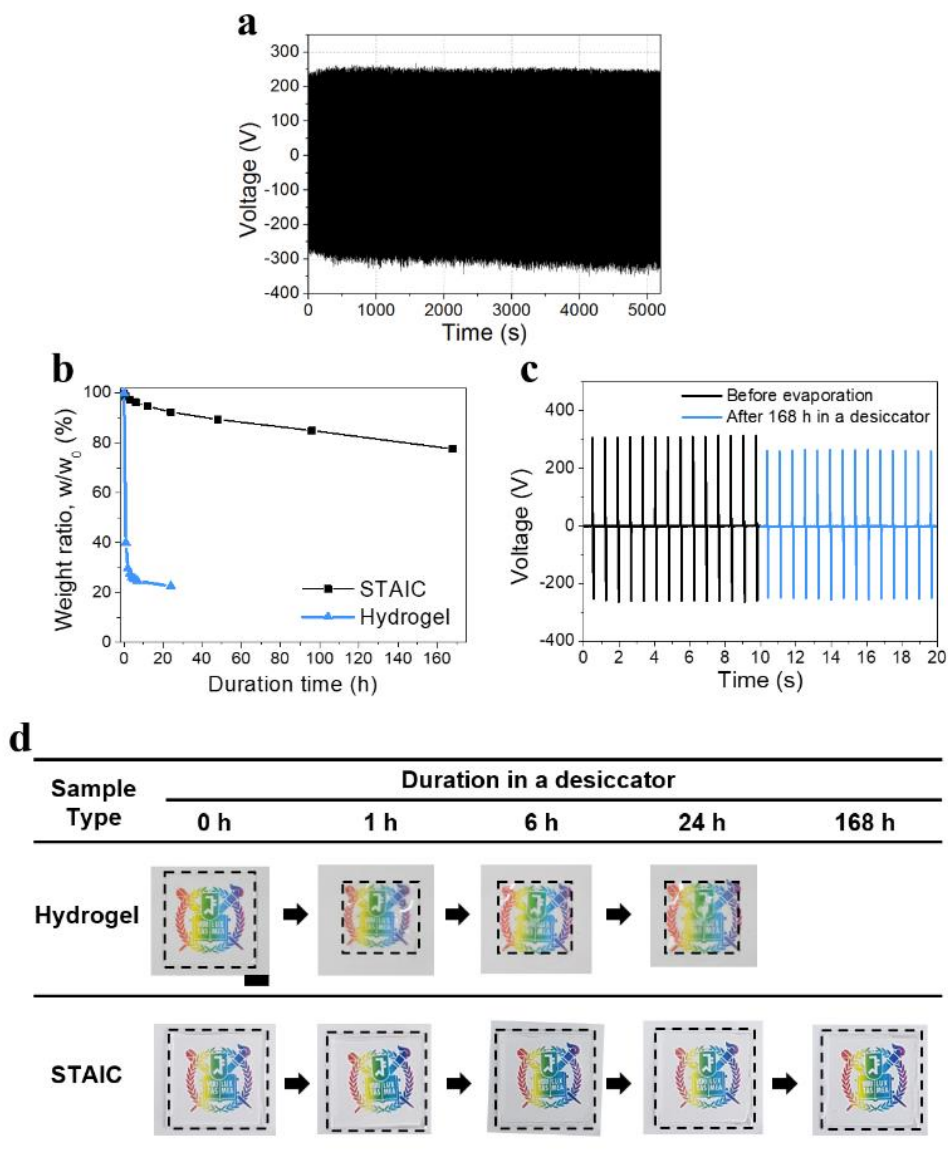


Fig. 2.9 (a) Durability of a STAIC was tested for 25,600 cycles. (b-d) Anti-dehydration ability of a STAIC under a vacuum of 0.013 atm at room temperature. Normalized weight ratio of a STAIC and a hydrogel according to duration time (b). Triboelectric output voltages of STAICs before and after being placed under the vacuum for a week (c). Photographs showing contrasted extent of shrinkages of hydrogel and STAIC during the evaporation experiments (d). (scale bar: 1 cm)

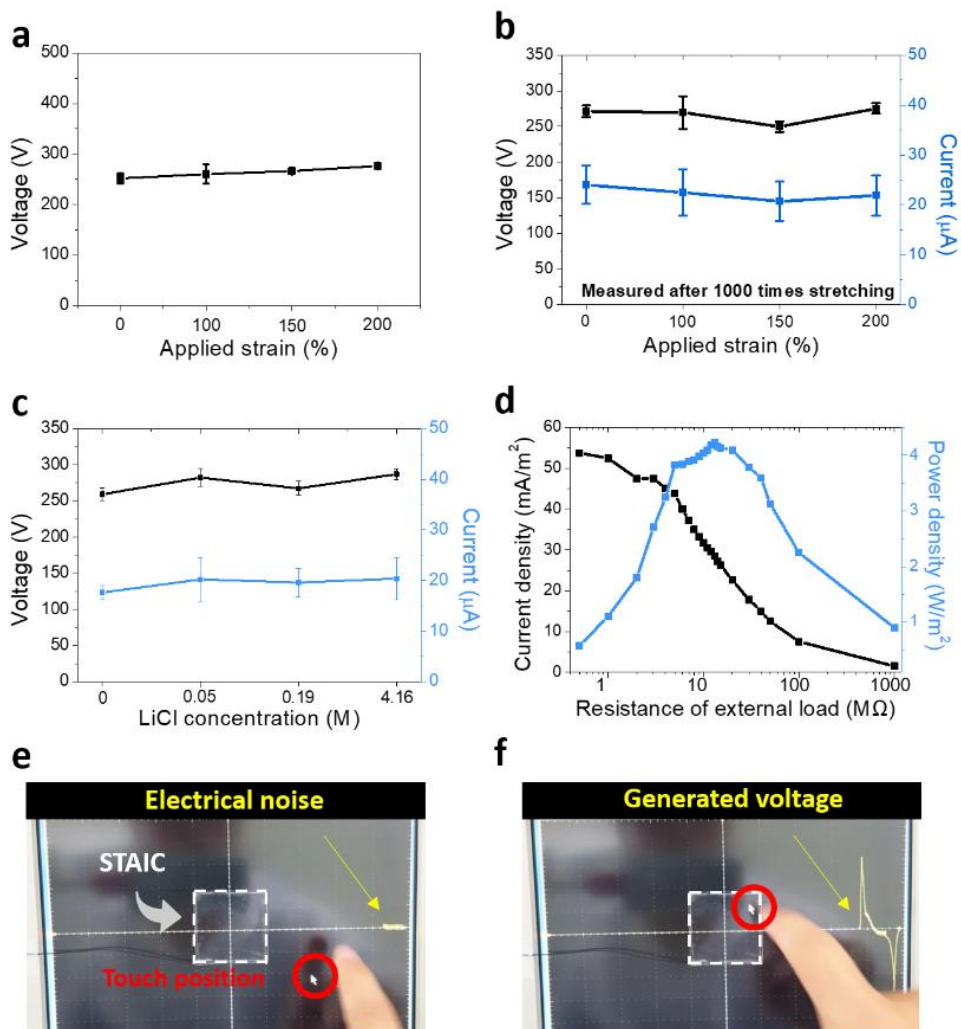


Fig. 2.10 (a) Triboelectric outputs measured under 100%, 150% and 200% of applied tensile strain. (b) Triboelectric outputs were measured after 1,000 times of uniaxial stretching. 100%, 150% and 200% of strain were applied. (c) Effect of ion concentration on triboelectric outputs. (d) Output current density and output power density of a STAIC with various external loads. Electrical performance when touching (e) outside and (f) inside of STAIC boundary which is attached on a touch screen. A STAIC was attached on top of a touch screen (this time, a resistive touch screen of an oscilloscope was used). A STAIC generated a voltage of 30 V when the screen was touched but did not hide the screen because the STAIC is highly transparent. All error bars in the figure represent s.e.m. of the data.

#### 2.3.4. STAICs with self-cleanability

TENGs with polymer surfaces easily get contaminated during operation, resulting in a decrease of electrical output performances and transparency. Self-cleanability was achieved in STAICs by perfluorination through HDFs deposition with air plasma treatment. Fig. 2.11a, b show photographs of a static contact angle of a water droplet on non-treated STAICs and on HDFs-treated STAICs. As shown in Fig. 2.11c, the static contact angle of water was not influenced by HDFs treatment with various plasma times. Fluorine functionalization normally makes the surface exhibit a higher contact angle [47], but because PDMS is adequately hydrophobic, the static contact angle was not significantly changed by the functionalization. Fig. 2.11d, e show advancing and receding contact angles on the non-treated (Fig. 2.11d) and HDFs-treated surfaces (Fig. 2.11e). The HDFs-treated surface showed higher receding contact angles (Fig. 2.11f) making contact angle hysteresis smaller (Fig. 2.11g). Because a water droplet can be detached easily from a hydrophobic surface that has a high receding contact angle, HDFs treatments making the surface self-cleanable. Fig. 2.11h shows the change of transmittance at the wavelength of 550 nm of the STAICs by HDFs treatment with various plasma times. The transmittance of STAICs was not influenced by the HDFs treatments and showed nearly 99% at all times. Compared to previous studies on modified surfaces with nano–micro patterning [29], this HDFs surface treatment has an advantage of retaining its transparency. The self-cleanability of STAICs was demonstrated by applying activated charcoal powder, which adheres well, as the simulated contaminant on each STAICs. Fig. 2.12a shows the cleaning behaviors of non-treated and the HDFs treated STAICs according to the following procedure. In the initial state, photographs indicate that both the non-treated and treated STAICs show good

transparency. By using ImageJ, photographs with dimensions of 30 mm by 30 mm were converted to 16-bit grayscale images to accurately show the contaminated (black) and uncontaminated (white) areas. An abundant amount of activated charcoal powder was spread on each horizontally placed STAIC. As shown in Fig. 2.12b, each STAIC was covered with activated charcoal powder and tilted by approximately 45° relative to the horizontal line. Approximately 5 mL of water in a syringe was shot twice onto each surface (Fig. 2.12c). Water droplets contacted the powder and removed contaminants by the rolling down. Subsequent water drops cleaned the surface, showing self-cleaning behavior that is generated by the HDFS treatment. Followed by the water jet, each STAIC was cleaned with ethanol by ultrasonication for 10 s and 5 min. To quantitatively investigate the self-cleaning effect, the contaminated area on each surface was estimated by using ImageJ (Fig. 2.13a). After the water jet process for HDFS-treated STAICs, the contaminated area was reduced to as low as 35.6%p, compared to 93.6%p remaining in the case of non-treated STAICs. After ultrasonication in ethanol for 10 s and 5 min, contamination areas of HDFS-treated STAICs were reduced to as low as 15.2%p and 6.0%p, compared to 31.0%p and 19.3%p in the case of non-treated STAICs. To further investigate the self-cleaning effect, UV–vis spectroscopy was used to study the transmittance of the STAICs (Fig. 2.13b). Average transmittance was obtained by randomly scanning selected points 10 times. After the water jet process for the HDFS-treated STAICs, average transmittance was increased to 55.1%p, compared to the increase of 14.5%p in the case of non-treated STAICs. After ultrasonication in ethanol for 10 s and 5 min, the average transmittance of HDFS-treated STAICs was increased to as high as 82.7%p and 94.4%p, compared to the increase of 55.8%p and 69.6%p in the case of nontreated STAICs. Moreover, since contaminated contact surface reduces

triboelectric performance [48, 49], output voltages of STAICs were investigated after each cleaning process, as shown in Fig. 2.13c. Due to the self-cleaning ability of HDFS-treated STAICs, the output voltage of HDFS-treated STAICs was enhanced to 19.4%p after the water jet, compared to remaining at 0.4%p for the non-treated STAICs. The electrical output performance was suitably recovered to as high as 67.0%p and 78.2%p after the further ultrasonication cleaning process, compared to the increase of 28.6%p and 57.5%p of non-treated STAICs. Thus, HDFS treatments on STAICs can provide optical and electrical stability.

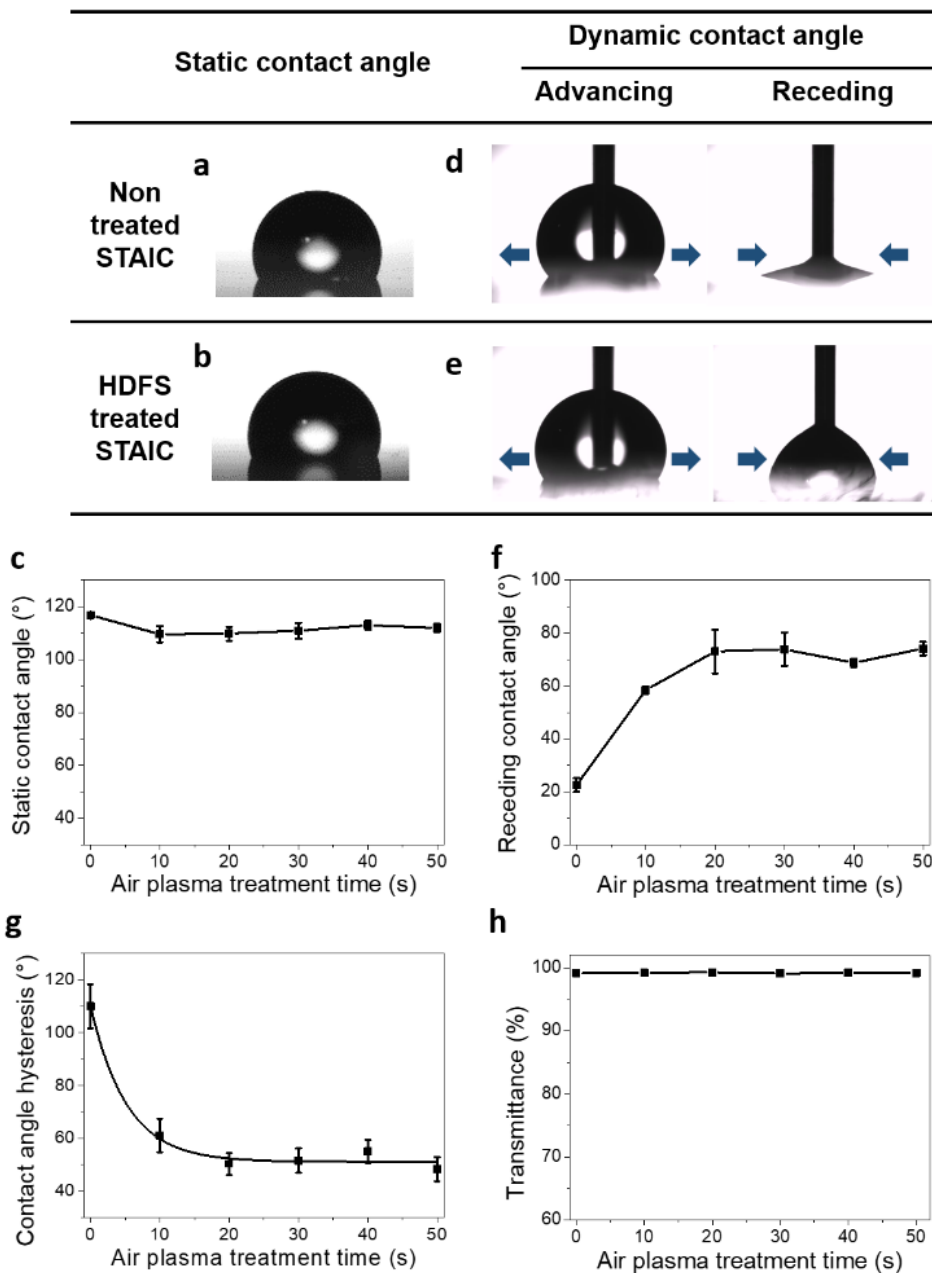


Fig. 2.11 Self-cleanability of a STAIC. Static contact angles were observed for **(a)** non-treated surfaces and **(b)** HDFS treated surfaces. **(c)** Static contact angles were investigated for various plasma time. Advancing and receding contact angles measured with deionized water on **(d)** non-treated surfaces and **(e)** HDFS-treated surfaces. **(f)** Receding contact angle and **(g)** contact angle hysteresis were greatly influenced by HDFS treatments making the surface self-cleanable. **(h)** Transmittance of STAICs for a green visible light (550 nm). All error bars in the figure represent standard error of the mean of the data.

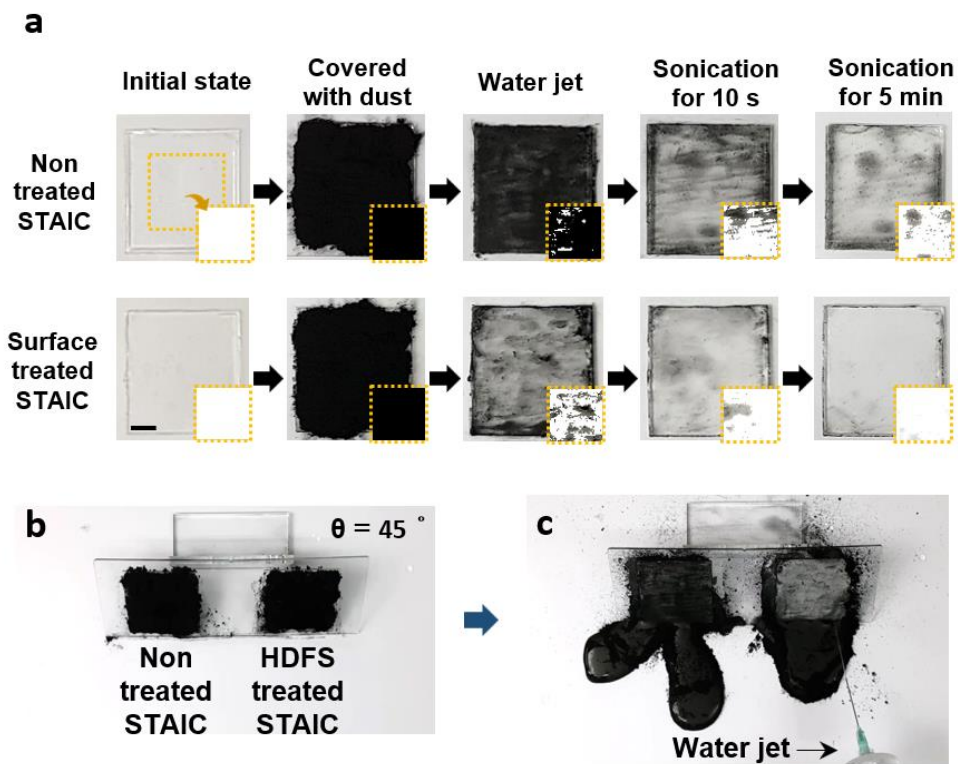


Fig. 2.12 (a) Self-cleanability of HDFS-treated STAICs was explored by cleaning surfaces which were contaminated by activated charcoal powders. (b, c) Demonstration of self-cleanability of STAICs. Dust on HDFS-treated STAIC was removed easily by a water jet (scale bar: 1 cm).

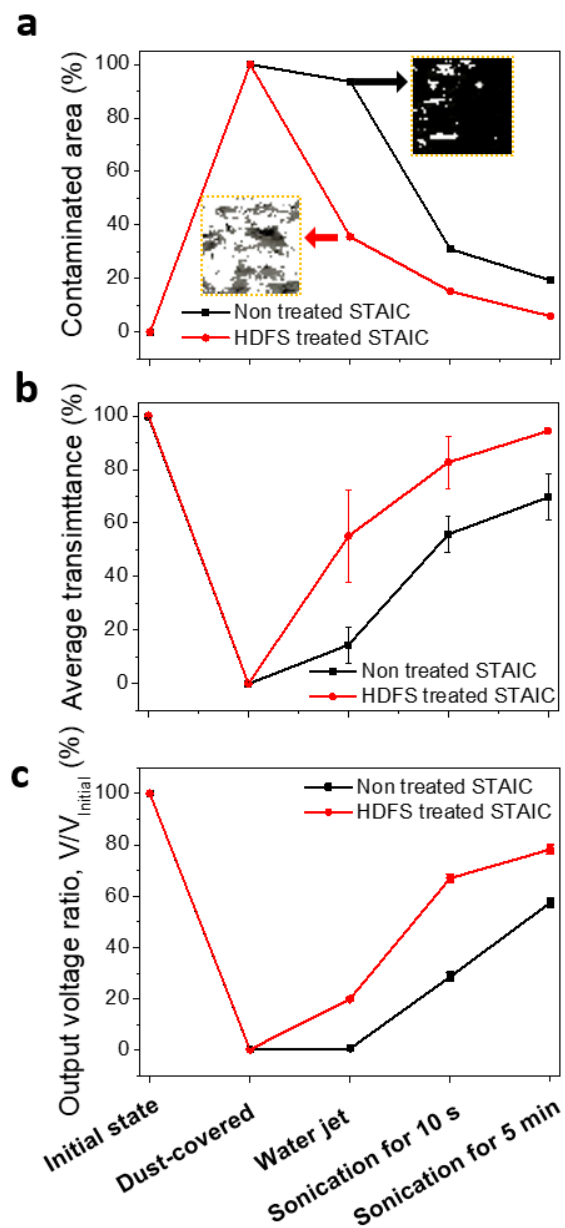


Fig. 2.13 (a) Contaminated areas and (b) average transmittances at 550 nm were measured according to the processes. Ten points on STAICs were randomly explored to calculate the average transmittance. (c) Output voltages of STAICs were investigated according to the cleaning processes. All error bars in the figure represent standard error of the mean of the data (scale bar: 1 cm).

### 2.3.5. Wireless real-time communication based on STAICs.

To apply STAIC to human skin, effects of sweat from the skin are required to be considered. The effect of humidity on triboelectric performance was investigated in Fig. 2.14. The output voltage decreased from about 270 to 50 V as the relative humidity increased from 20% to 80%. However, a STAIC can operate under a high relative humidity of 80%, because it can still generate detectable voltages. A thimble-type wireless real-time communicator was produced for human-machine interfaces based on STAICs. STAICs were attached to fingers as shown in Fig. 2.15. Thumb, index, middle, ring, and little fingers were coded to signal  $2^0$ ,  $2^1$ ,  $2^2$ ,  $2^3$ ,  $2^4$  with a microcontroller for real-time communication, respectively. The combinations of the signals from each finger were interpreted to an alphabet as shown in the inset of Fig. 2.15a. Prior to the communication, we checked the triboelectric property of STAICs on a finger by touching skin and clothes. The STAICs successfully harvested electrical energy from a gentle touch to skin (61.6 V) and fabric (13.0 V) (Fig. 2.15b). A circuit was then fabricated to make real-time communication between the STAICs and a wireless computer, as shown in Fig. 2.16a. STAICs were connected to a microcontroller through a low-pass RC filter to decrease electrical noise. Fig. 2.16b shows a demonstration of a wireless real-time communicator based on STAICs. To input letter “D”, a value of 4 is needed, which is given by a single touch of the middle finger (22) (Fig. 16b i). For writing “R”, a value of 18 is needed, requiring simultaneous touch of the index (21) and little finger (24) (Fig. 16b ii). Writing “E”, “A”, and “M” is based on the same mechanism. The word “DREAM” was successfully typed with STAICs.

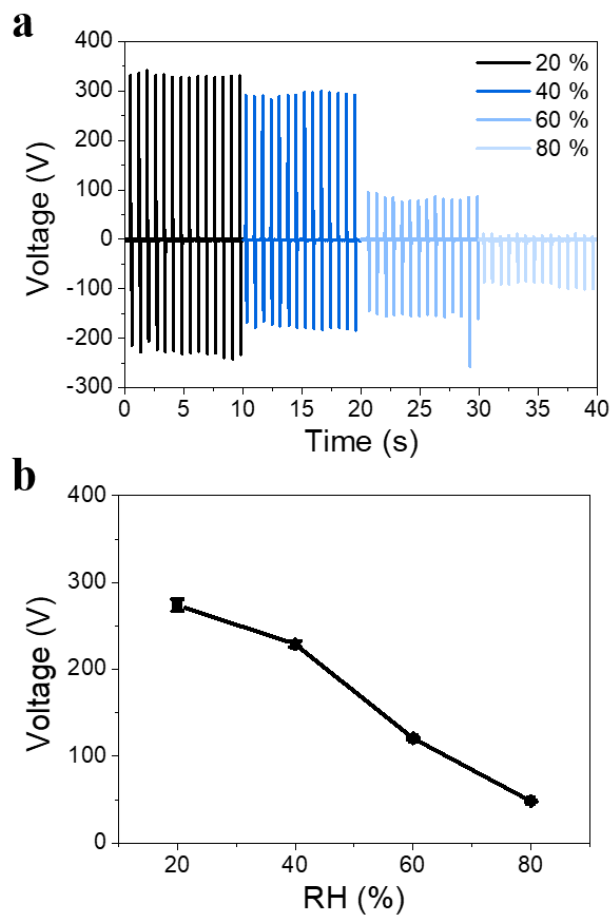


Fig. 2.14 (a) Measured output voltages and (b) averaged peak to peak voltages under humid conditions. All error bars in the figure represent s.e.m. of the data.

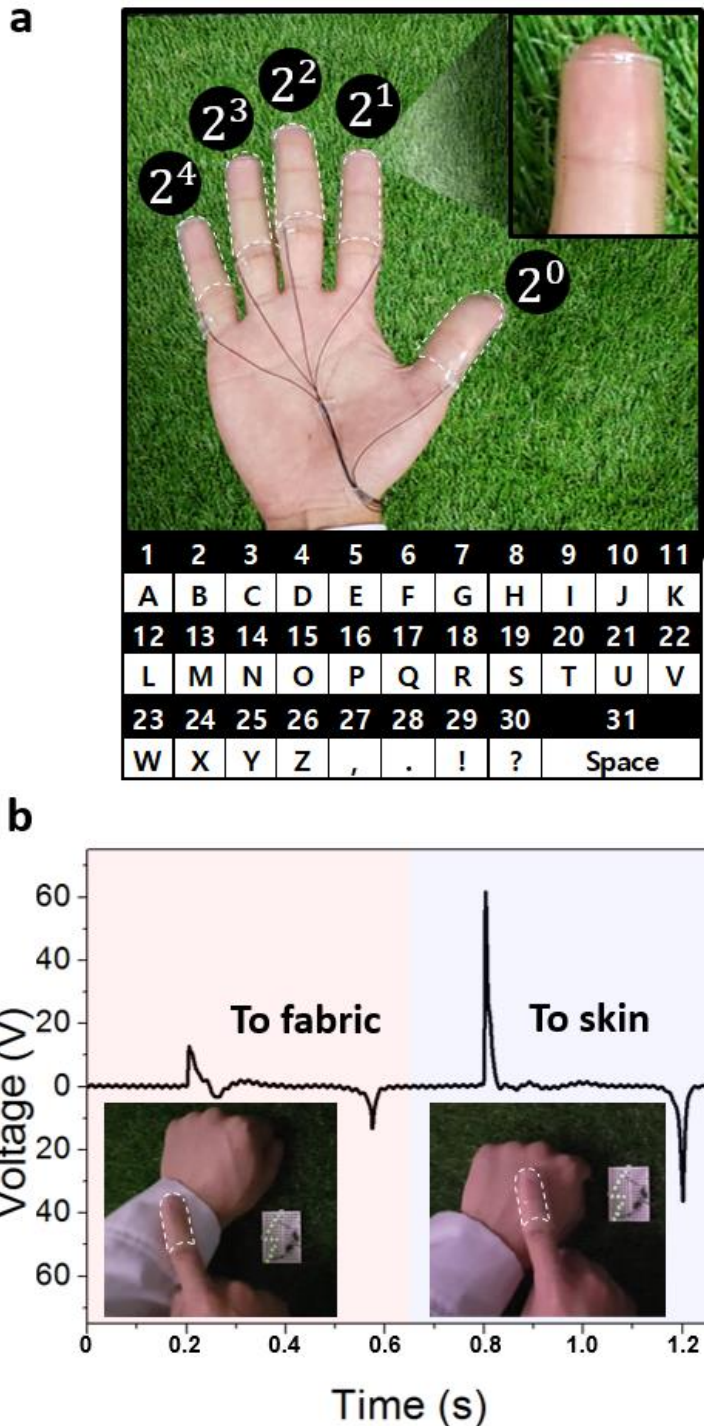


Fig. 2.15 (a) STAICs were attached on the fingers and connected with wires to a controller board. A different order of a binary system was assigned to each finger, and the letters were pre-coded in the microcontroller. (b) Generated voltages of a STAIC by a gentle touch to a fabric and the skin.

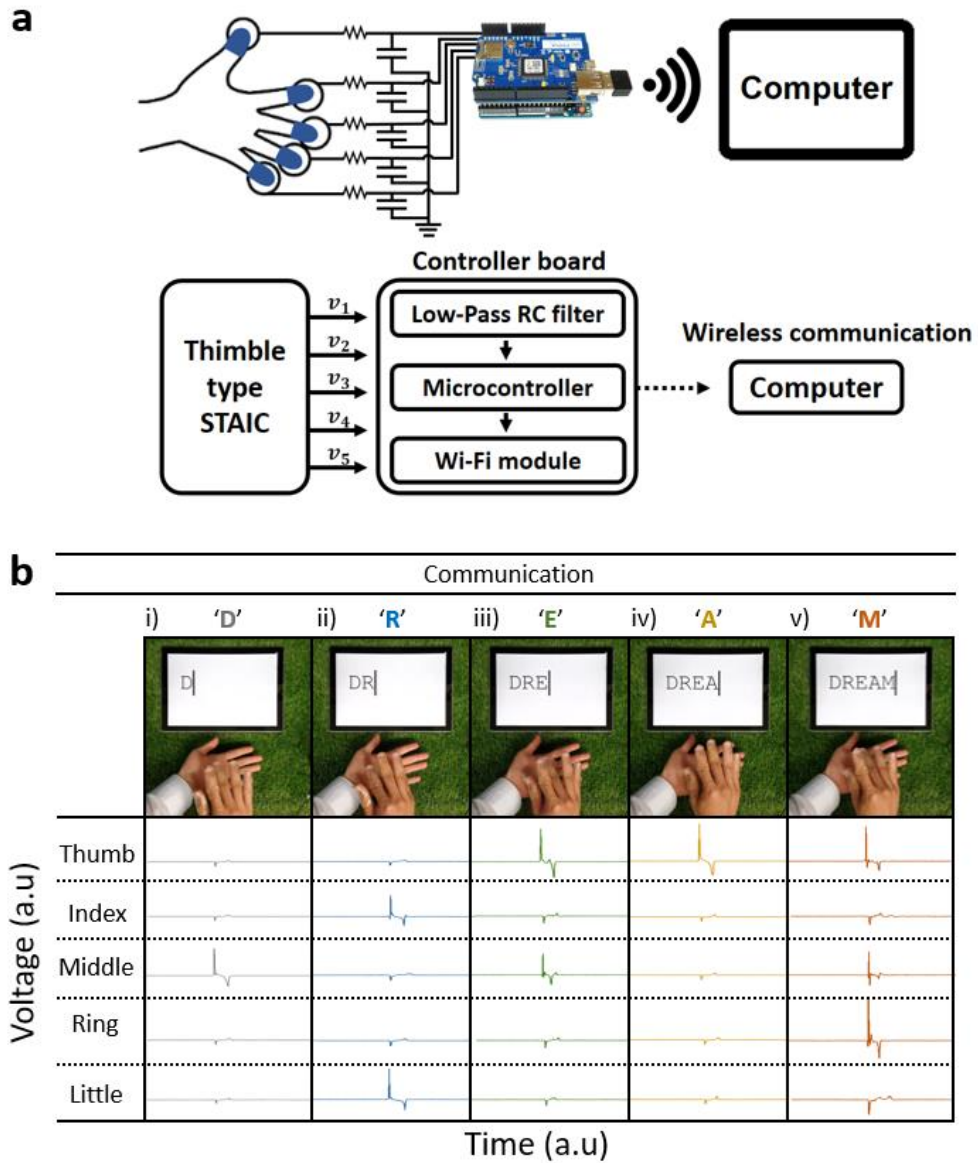


Fig. 2.16 **(a)** Block diagram of the communicator based on STAICs. STAICs were connected to a controller board which contains an RC low-pass filter, a microcontroller and a Wi-Fi module. **(b)** Demonstration of real-time communication with STAICs. “DREAM” was typed using combinations of finger touches.

## 2.4. Conclusion

Highly transparent (99.6%) and stretchable (330%) STAICs were fabricated by reliably applying a hydrogel as a conducting layer of a TENG. Working mechanism of the hydrogel based TENG was suggested in detail. Potential issues of electrochemical reactions in hydrogels and relatively low hydrogel conductivity were investigated. Mechanical reliability was secured by chemical bonding between the ionic conductor and contact material, which is critical for the functionality and durability of hydrogel electronics. By controlling gelation time, both high transmittance and a robust hydrogel–PDMS interface were secured, preventing the light scattering on the interface of the chemically bonded layers. Additionally, HDFs surface treatment ensured an increased electrical output power (increase of output voltage by 24.5% and of output current by 17.5%) without sacrificing the transmittance in comparison with non-treated STAICs. Self-cleanability was attained by HDFs surface treatment, leading to recovered transmittance (40.6%p increase) and electrical output voltage (19.4%p increase) compared to the non-treated STAICs at the water jet step after simulated dust covering. Due to the stable transmittance and stretchability, STAICs served as a thimble-type, wireless, real-time, human–machine communicator by harvesting gentle touches with fingers. Remarkably, the attractive features of STAICs open up exciting opportunities not only for self-powered, transparent, attachable HMIs for wireless sensor networks but also for broader applications of stretchable ionics, soft robotics, and self-powered monitoring systems for biomechanical motion.

## Chapter 3. Soft ionic proximity sensors

### 3.1. Introduction

Human beings recognize the relative positions of surrounding objects using their visual, tactile, and auditory sensory abilities [50]. Visual sensation based on binocular disparity plays an especially vital role in spatial perception [51]. The distance, a few centimeters, between both of a person's eyes means that each retina generates a different two-dimensional image; the brain then recognizes the relative positions of objects by comparing the two images. However, people who are blind or visually impaired cannot rely on visual sensation to perceive space. Such individuals have to depend on tactile sensation to recognize surrounding objects. However, groping around is potentially dangerous because it inevitably involves contact with unwanted objects. Thus, artificial sensory systems that can support spatial perception in daily life are needed.

One option to meet this challenge is non-contact sensing technologies (i.e., radio detection and ranging (RADAR) [52], light detection and ranging (LIDAR) [53, 54], and sound navigation ranging (SONAR) [55, 56], which allow for detection of objects in the environment without any physical contact. To perceive space, these sensors emit waves, such as electromagnetic waves and sound waves. By receiving the waves reflected by nearby objects, the exact position of the objects can be estimated. Based on their non-contact sensing capability, these sensors have been applied to various machines, including aircraft, ships, submarines, and self-driving cars, for object localization [57, 58]. However, to detect the position of an object, these sensors require precisely aligned wave transmitters and receivers. The inherent

limitations of such systems make it difficult for conventional non-contact sensors to be made with soft materials that could comfortably interface with the human body.

Here, we introduce a soft ionic proximity sensors (SIPS) for non-contact spatial perception (Fig. 3.1). While conventional proximity sensors have been suffered from lack of softness due to their working mechanism and structures, we suggest soft proximity sensors by applying hydrogels and tribotronics. Ionically conductive hydrogels were used as the soft electric field receivers of the SIPS. Based on electrostatic induction, these receptors can detect the electric field that originates from static charges on the surface of an object. By comparing the intensity of electric fields sensed by each hydrogel receiver, the relative position of the nearby object can be estimated in the same manner as by the animals. Because the SIPSs sense the electric fields originating from objects, they do not require any transmitters that would necessitate maintenance of precise alignment with the receivers. Thus, the receptors can maintain their sensing capability even though they are made of soft materials, and have the advantage of neglectable power consumption compared with conventional non-contact sensing technologies. Moreover, because an electric field can be transmitted through dielectric materials, a SIPS can be used to detect objects behind a wall.

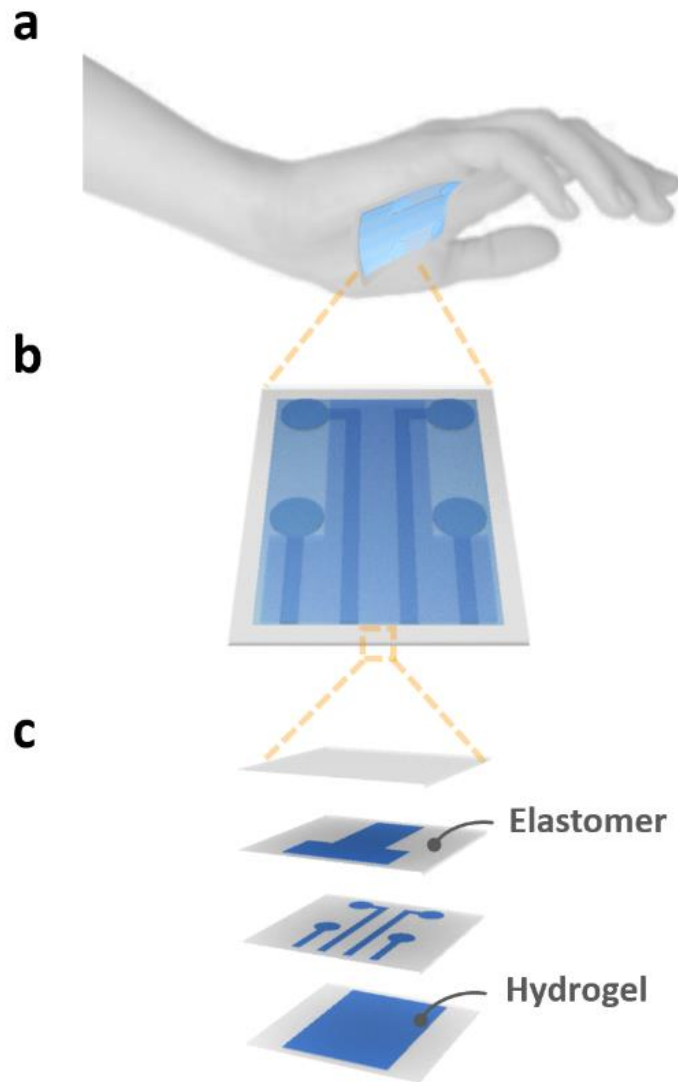


Fig. 3.1 **(a)** A wearable SIPS was developed to support human spatial perception in daily life. **(b, c)** The SIPS can identify the relative positions of nearby objects by comparing the intensity of the electric fields sensed by each hydrogel electric field receiver.

## 3.2. Experimental section

### 3.2.1. Materials and specimen preparation.

SIPs were fabricated using a polyacrylamide hydrogel containing lithium chloride (LiCl). Acrylamide (AAM, A8887, Merck) and N, N-methylenebisacrylamide (MBAAM, M7279, Merck) were used as a monomer and cross-linker for the hydrogel, respectively. Lithium chloride (LiCl, L4408, Merck) was used as an ionic charge carrier. Lithium phenyl-2,4,6-trimethylbenzoylphosphinate (LAP, 900889, Merck) and benzophenone (BP, B9300, Merck) were used as a photo initiator and ultraviolet-assisted grafting agent, respectively. Very high bond tapes (VHB, 4905, 3M) were used as elastomers in the SIPs.

### 3.2.2. Preparation of hydrogel precursor solution.

A hydrogel precursor solution was prepared by dissolving AAM and LiCl in deionized water. The molar concentrations of the AAM and LiCl were both 2 M; 1.55 wt% of MBAAM and 1.24 wt% of LAP with respect to the weight of AAM were added to the solution.

### 3.2.3. SIPS fabrication process

The VHBs were immersed in BP solution (15 wt % in ethanol) for 10 min for swelling-driven absorption. Then, the VHBs were washed with ethanol and completely dried with nitrogen gas. The grafting agent-absorbed VHBs were treated with a 365 nm ultraviolet (UV) lamp (UVGL-25, UVP) for 10 seconds. Hydrogel electric field receivers with a diameter of 2 cm and a thickness of 200  $\mu\text{m}$  were printed on the grafting agent activated VHBs using a digital light processing 3D printer (Litho Advanced 3D printer, Illuminoid). During printing, the hydrogel precursor solution was exposed to 385 nm UV light for 10 s. After printing, the

fabricated hydrogel/elastomer hybrids were washed with ethanol and completely dried with nitrogen gas. To enhance the contrast between the hydrogels and elastomers, fluorescent dyes (R6626, Merck) were added to some of the hydrogels.

#### 3.2.4. Mechanical testing

For uniaxial-tensile tests of the hydrogel/elastomer hybrids, a 200  $\mu\text{m}$  thick hydrogel was printed on the VHB. The test was carried out using a universal testing machine (3343, Instron) with a receding rate of 1 cm/min.

#### 3.2.5. Characterization of sensing capability

A hydrogel electric field receiver that was 2 cm in diameter and 200  $\mu\text{m}$  in thickness was connected to an external load of 5 G $\Omega$ . An electrometer (6517A, Keithley) was used to measure the induced voltage across the external load. A pushing tester (LW139.138-40, Labworks), a linear power amplifier (PA-138, Labworks) and a function generator (33612A, Agilent) were used to provide vertical simple harmonic oscillation of the objects. The initial distance, amplitude, and frequency of the oscillating object were 3 cm, 1 cm, and 2 Hz, respectively. To prevent ambient electrical noise, measurements were conducted in a Faraday cage. To simulate a charged target, the perfluoroalkoxy alkane (PFA) object was charged by rubbing it with polypropylene (PP).

#### 3.2.6. Characterization of through-wall sensing capability

To characterize the through-wall sensing capability of the SIPS, dielectric barriers and hydrogel conductive shields were placed between the receivers and the object, respectively. The dielectric barriers were 50  $\times$  50  $\times$  15 mm (length  $\times$  width  $\times$  thickness) in size. The relative permittivities of the barrier materials were measured using dielectric constant measurement fixture (16451B, Keysight). The hydrogel conductive shield, 50  $\times$  50  $\times$  0.2 mm (length  $\times$  width  $\times$  thickness) in size, was

fabricated using a 3D printer and connected to ground. To investigate the effect of the data line on the sensing capability, the receiver was connected to a data line with a size of  $50 \times 5 \times 0.2$  mm (length  $\times$  width  $\times$  thickness).

### 3.2.7. Demonstration of through-wall sensing capability

Two hydrogel electric field receivers were prepared, both of which were  $20 \times 20 \times 5$  mm (length  $\times$  width  $\times$  thickness). Both receivers were connected to the external load with indium tin oxide-coated polyethylene terephthalate film (639303, Merck). LabView (National Instruments) was used to turn on LEDs when the induced voltage exceeded a threshold voltage. The distance between the pendulum and the receiver was 2 cm. To demonstrate the through-wall sensing capability of the SIPS, a dielectric barrier and conductive shield were placed between the receiver and the pendulum. A 2 mm thick piece of paper was used as the dielectric barrier, and a 2 mm thick piece of grounded aluminum was used as the conductive shield.

### 3.2.8. Demonstration of a wearable SIPS for spatial perception

The sensing and shielding layers of the wearable SIPS were fabricated using the 3D printer. The sensing layer comprised four hydrogel electric field receivers with a diameter of 1 cm. The hydrogel conductive shield of the top shielding layer was designed to cover all data lines in the sensing layer. The hydrogel conductive shield of the bottom shielding layer was designed to cover all data lines and receivers in the sensing layer. The wearable SIPS was assembled by stacking the bottom shielding layer, sensing layer, top shielding layer, and cover layer, in that order. Silver-plated copper wires were used to connect the hydrogels of the SIPS to the external loads and ground. LabView was used to generate auditory signals when a nearby object was detected.

### 3.3. Results and Discussion

#### 3.3.1. Fabrication of a SIPS with high mechanical reliability.

Based on their high ionic conductivity and stretchability, hydrogels are promising materials as soft conductors for the SIPS [59-66]. Moreover, elastomers are suitable for use as soft insulators because they can effectively block the migration of mobile ions in a hydrogel without deteriorating the hydrogel's stretchability [67-70]. However, because hydrogels and elastomers exhibit quite different hydrophobicity, a poor interface between the two can undergo delamination under mechanical strains, thus limiting the wearable applications of the SIPS [59, 60, 71]. This issue becomes especially critical when 3D-printing technology is used to print a hydrogel directly on an elastomer for rapid and elaborate fabrication. Even though there have been valuable efforts to adhere hydrogels with elastomers [71-75], it remains challenging to form a robust interface between the two during 3D printing to secure mechanical reliability.

To fabricate a mechanically reliable SIPS using 3D printing technology, we covalently anchored hydrogels to elastomers during the printing process (Fig. 3.2). First, a pre-shaped elastomer was immersed in a solution with an ultraviolet-assisted grafting agent for swelling-driven absorption (Fig. 3.2a). Thereafter, the grafting agent absorbed elastomer was treated with 365 nm ultraviolet (UV) light for 10 seconds to promote radical formation at polymer chains (Fig. 3.2b). Then, the hydrogel was directly printed on the UV-treated elastomer using a digital light processing (DLP) 3D printer (Fig. 3.2c). During the printing process, radicals of the elastomer participate in free-radical polymerization of the hydrogel, thus forming a covalently cross-linked robust interface. Finally, the SIPS was assembled by stacking the printed layers (Fig. 3.2d).

To facilitate rapid and elaborate fabrication, it is necessary to minimize the UV irradiation time during printing. Thus, high-efficiency photoinitiators are used to cure the hydrogel within a short period of time [76-78]. However, the quantum efficiency of the ultraviolet-assisted grafting agent in the elastomer is much lower than that of the hydrogel photoinitiator [79]. This discrepancy causes the grafting agent to activate after the hydrogel is cured when the hydrogel precursor and the grafting agent absorbed elastomer are simultaneously exposed to UV light during printing. In this case, the radicals of the elastomer cannot participate in the free-radical polymerization of the hydrogel, resulting in poor interfacial bonding between hydrogel and elastomer (Fig. 3.3a). To solve this problem, we developed a strategy to activate the grafting agent before printing. This strategy secures the mechanical reliability of the SIPS while still allowing for rapid and elaborate fabrication (Fig. 3.3b). From grafting agent activation to printing, the overall time required to fabricate each layer of the SIPS is less than 1 minute (see Experimental section for details). Furthermore, the resolution of the printed hydrogel is up to 50  $\mu\text{m}$ , which is sufficient to print the elaborate hydrogel network of the SIPS. Although the hydrogel/elastomer interface could be translucent during the covalent cross-linking process [68], the fabricated SIPS is as transparent as the individual elastomer and hydrogel because the rapidly fabricated hydrogel/elastomer interface scatters a negligible amount of visible light (Fig. 3.3c). Moreover, the robust interface can withstand a mechanical strain of more than 300% without delamination, allowing the SIPS to be used in wearable applications (Fig. 3.3d, e).

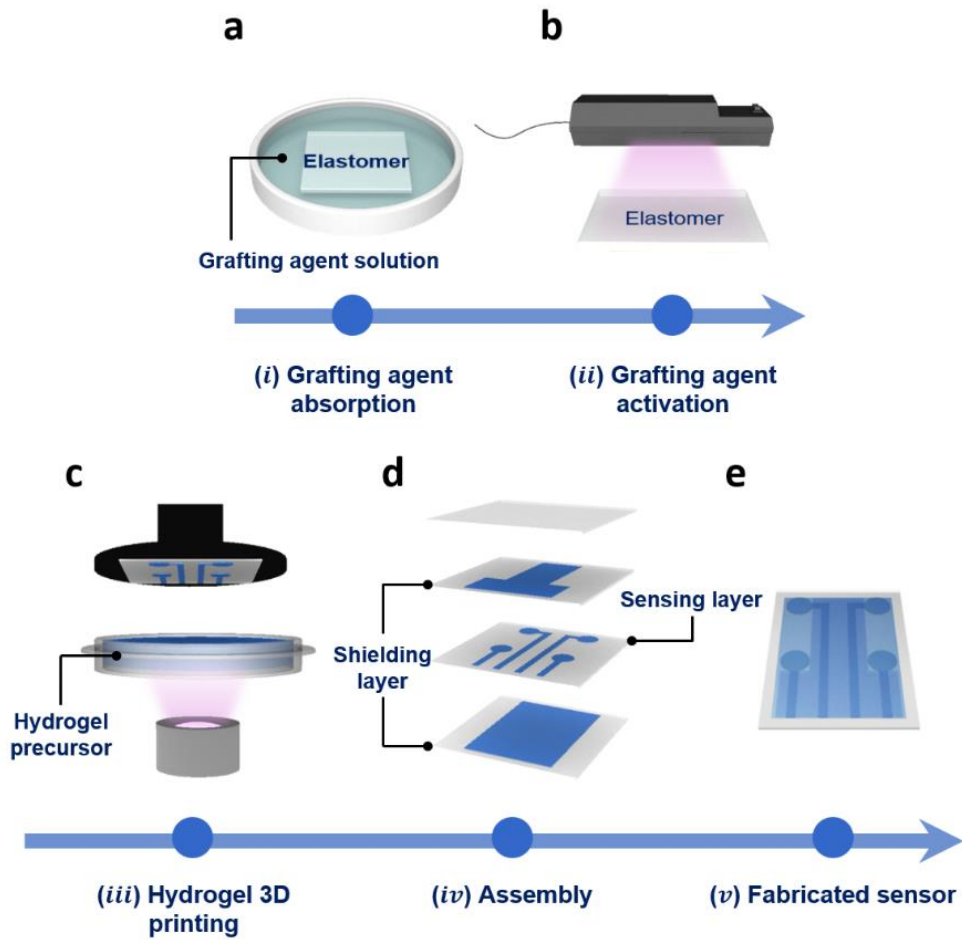


Fig. 3.2 Conductive hydrogels were covalently anchored to an elastomer during 3D-printing for rapid and elaborate fabrication of a soft artificial electroreceptor (SIPS) with high mechanical reliability.

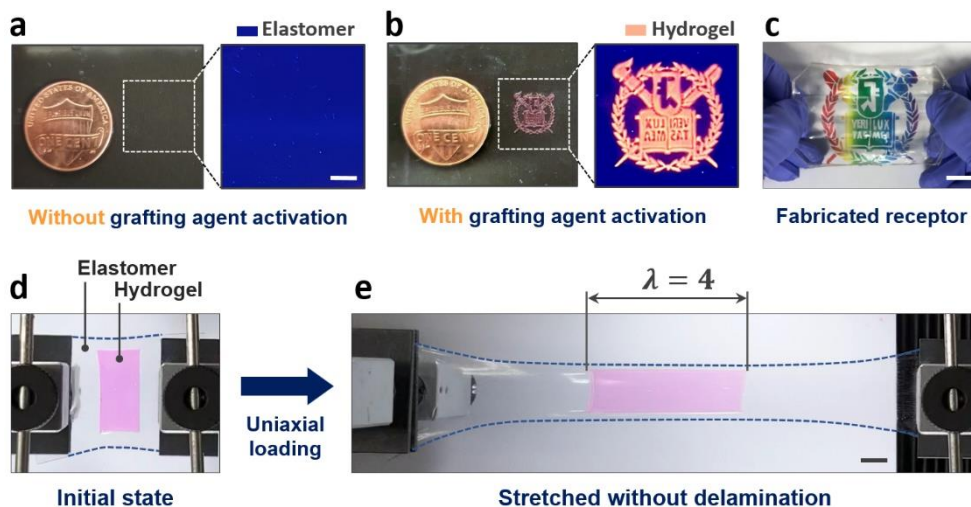


Fig. 3.3 (a) In the absence of grafting agent activation, delamination occurs between the hydrogels and the elastomer during the printing process due to poor interfacial bonding. Scale bar, 250  $\mu\text{m}$ . (b) Grafting agent activation allows radicals in the elastomer to participate in free-radical polymerization of the hydrogel during printing, thus forming a tough interface between the hydrogel and elastomer layers. (c) The SIPS was highly transparent to visible light of all colors because the rapidly fabricated hydrogel/elastomer interface scatters a negligible amount of visible light. Scale bar, 1 cm. (d, e) The hydrogel layer on the elastomer could be stretched more than 400% without delamination. To enhance the contrast between the hydrogel and elastomer, fluorescent dyes were added to the hydrogel. Scale bar, 1 cm.

### 3.3.2. Sensing capability of the SIPS

Based on electrostatic induction, the SIPS can sense an electric field originating from static charges on the surface of an object. Because contact with its surroundings causes the object to be charged through contact electrification, almost all objects have static charges on their surfaces (Fig. 3.4a) [67, 68, 80-82]. When an object is close to the receptor, electric fields originating from the object's surface charges induce voltage in the hydrogel electric field receiver of the SIPS (Fig. 3.4b). Therefore, by measuring the voltage across the external load connected between the receiver and ground, the intensity and polarity of the electric field can be estimated.

To experimentally characterize the sensing capability of the SIPS, a charged object was fixed on a pushing tester that provided consistent vertical simple harmonic oscillation (see Experimental section and Fig. 3.4c for details). When the pushing tester generated vertical oscillation of the object, the induced voltage closely traced the relative position of the object with various amplitudes (Fig. 3.4d). This finding reveals the outstanding potential of the SIPS to detect the movement of nearby objects without making physical contact. The induced voltage was measured as the resistance of the external load was varied. When the resistance of the external load increased from 1 M $\Omega$  to 50 G $\Omega$ , the induced voltage increased by more than 130-fold (Fig. 3.5a). This result indicates that the sensitivity of the SIPS can be maximized by greatly increasing the resistance of the external load. Moreover, when the resistance of the external load was extremely high, the sensing capability of the SIPS was barely affected by the relative speed between the object and the receptor (Fig. 3.5b). The induced voltage was stably maintained at around 720 mV<sub>pp</sub> even when the oscillation frequency of the object was increased 4-fold.

To investigate the effect of charging materials on the sensing capability of the SIPS, perfluoroalkoxy alkane (PFA) and glass were charged using various materials including alumina, cotton, polypropylene (PP), polyimide (PI) and polytetrafluoroethylene (PTFE) (Fig. 3.5c). As the difference in electron affinity between the charging materials and the object increased (Fig. 3.5d), the density of the object surface charge increased, and a higher voltage was induced across the external load. Meanwhile, even though the electron affinity of glass and alumina are quite similar, perceptible values of 23 mV<sub>pp</sub> were still observed when the glass object was charged with alumina [67]. This finding indicates that objects in the vicinity can be sensed using the SIPS as far as they are charged. In addition, the receptor can more sensitively detect an object's movement when that object is close to the SIPS (Fig. 3.5e). This is because the strength of the electric field over the receptor increases as the distance between the object and the SIPS decreases. Moreover, the conductivity of the hydrogel can be controlled by varying the ion concentration [59-61]. However, the sensing capability of the SIPS was barely affected by ion concentration, even when the LiCl concentration decreased from 2 M to 2 mM, because the resistance of the external load is much higher than that of the hydrogel (Fig. 3.5f).

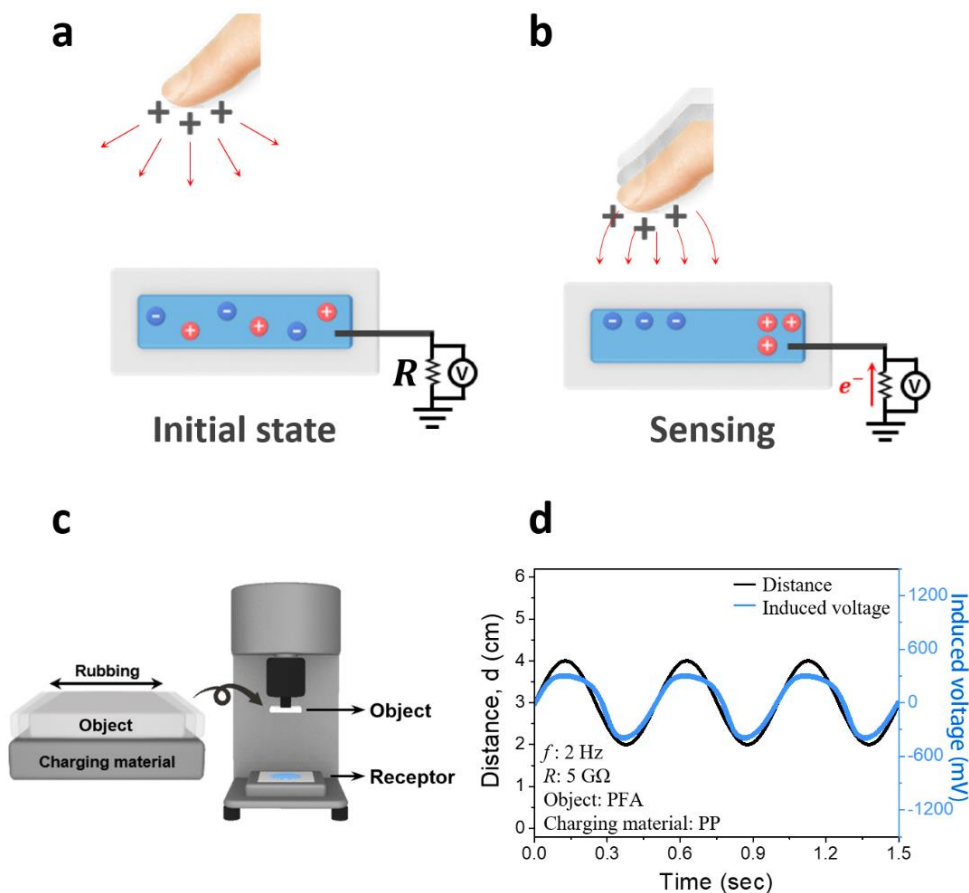


Fig. 3.4 (a, b) Schematic diagrams illustrating the sensing mechanism of the SIPS. An object will be charged due to contact electrification through contact with its surroundings (a). The electric fields originating from static charges on the surface of the object induce voltage in the hydrogel electric field receiver of the SIPS (b). Thus, by measuring the voltage across the external load connected between the receiver and ground, the intensity and polarity of the electric field can be estimated. (c) Pushing tester for vertical simple harmonic oscillation of the objects. The sensing capability of the SIPS was investigated with a pushing tester that provided vertical simple harmonic oscillation of the object. After cleaning, the object was charged by rubbing with the selected charging material. (d) The induced voltage closely traced the position of the object.

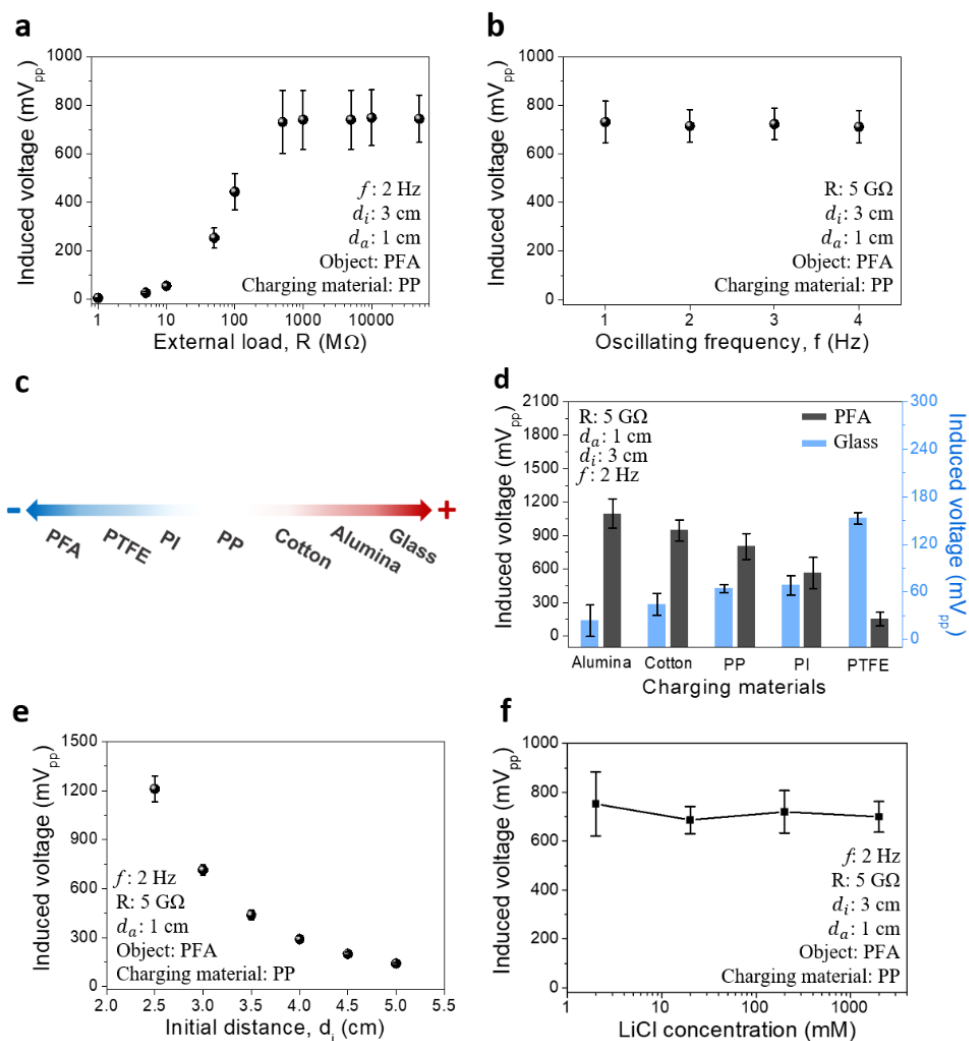


Fig. 3.5 (a, b) The induced voltage was measured while varying the external load resistance (a) and oscillating frequency of the object (b). (c) Triboelectric series. The surface of a material can be positively or negatively charged after physical contact with other materials, due to contact electrification. Each material has a tendency to gain or lose electrons. Glass and PFA were selected as positively and negatively charged objects, respectively. (d) The induced voltage was measured while varying object and charging materials. (e) The induced voltage was measured while varying initial distance between the SIPS and the object. (f) Voltage induction in the SIPS according to hydrogel LiCl concentration. The sensing capability of the SIPS was insensitive to hydrogel LiCl concentration in the range of 2 mM to 2 M. The sensing capability of the SIPS was barely affected by ion concentration. Error bars represent SD ( $n=3$ ).

### 3.3.3. Through-wall sensing capability of the SIPS

Under an external electric field, a dielectric material becomes polarized and transmits the electric field [83]. Thus, even if the object is behind a dielectric barrier, the SIPS can still detect object movement (Fig. 3.6a). Moreover, because the relative permittivity of the dielectric barrier is higher than that of air, the barrier can act as a medium to effectively transmit the electric field. Thus, when a barrier is placed between the SIPS and the object, the electric field that originates from the object reaches the receptor more strongly, inducing a higher voltage across the external load.

To investigate the through-wall sensing capability of the SIPS, barriers with various thicknesses and relative permittivity were placed between the object and the receptor. When the thickness of the barrier increased from 2.7 to 16.44 mm, the induced voltage increased from 606.7 to 2003.3 mV (Fig. 3.6b). Moreover, the induced voltage increased by 32.5% when the relative permittivity of the barrier increased from 2.1 to 4.6 (Fig. 3.6c).

Even though the electric field can be transmitted through a dielectric material, it cannot be transmitted through a grounded conductor. When the external electric field is applied, excess charges accumulate on the surface of the grounded conductor, preventing transmission of the electric field (Fig. 3.7a). Thus, the grounded conductor can be used as an effective electric field shield that can prevent unwanted electric fields from reaching the SIPS. To characterize the shielding capability of the grounded conductor, hydrogels with various thicknesses and LiCl concentrations were placed between the object and the SIPS. Irrespective of hydrogel thickness, more than 99% of the electric field was blocked by the hydrogel conductive shield (Fig. 3.7b). Even when the hydrogel conductive shield was just

200  $\mu\text{m}$  thick, the induced voltage decreased from 776.6 to 1.33 mV. In addition, the shielding capability of the grounded hydrogel was barely diminished even when the LiCl concentration decreased from 2 M to 2 mM (Fig. 3.7c).

To demonstrate the through-wall sensing capability, the SIPS with two electric field receivers was placed in front of an oscillating pendulum (Fig. 3.8a, b). When the induced voltage exceeded a threshold voltage due to the nearby pendulum, the connected computer lit up light emitting diodes (LEDs) corresponding to the receiver. Because the electric field can be transmitted through dielectric materials, the SIPS could be used to detect the movement of the pendulum even when a barrier was placed between the SIPS and the pendulum (Fig. 3.8c, d). When the electric field originating from the pendulum was transmitted through a 2 mm-thick piece of paper and induced a voltage that exceeded the threshold voltage of 5 V, a green LED turned on, indicating the presence of the pendulum. In contrast, when a 2mm-thick piece of grounded aluminum was placed between the SIPS and the pendulum, the electric fields that originated from the pendulum were blocked by excess charges on the surface of the aluminum (Fig. 3.8e, f). Thus, only a voltage far below the threshold voltage was induced across the external load, and the LED remained off.

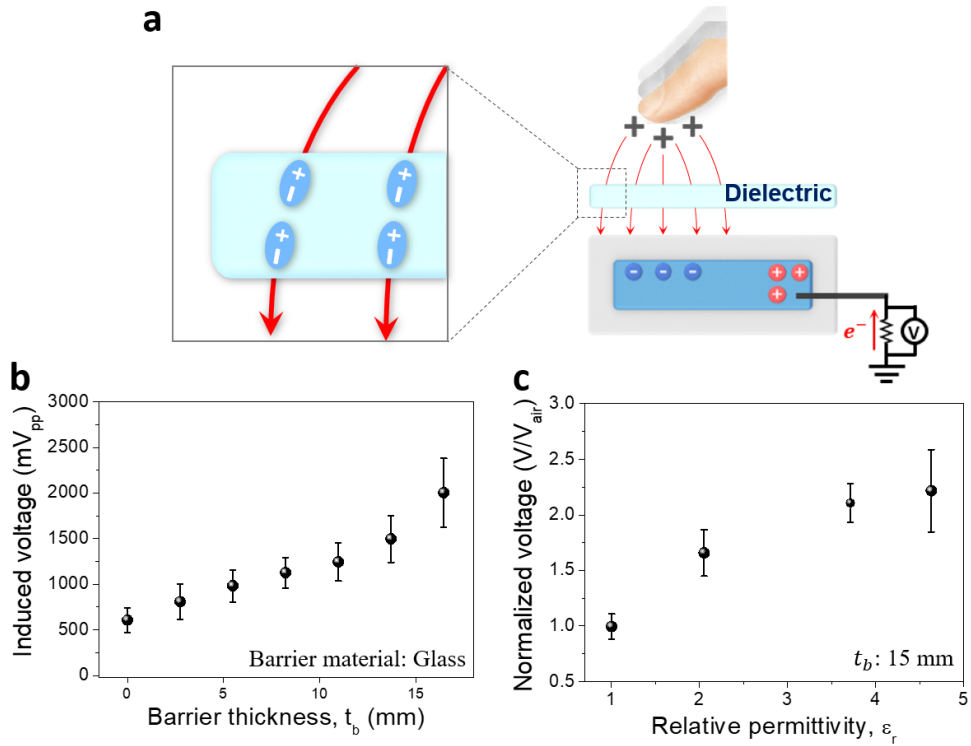


Fig. 3.6 **(a)** Schematic illustration of the mechanism of electric field transmission of a dielectric barrier. When an external electric field is applied, the dielectric becomes polarized and transmits the electric field, allowing the SIPS to detect an object behind the barrier. **(b, c)** The induced voltage was measured as the thickness (b) and relative permittivity (c) of the dielectric barrier were varied. Static electric fields have no effect on the sensing capability of the SIPS. Error bars represent SD ( $n=3$ ).

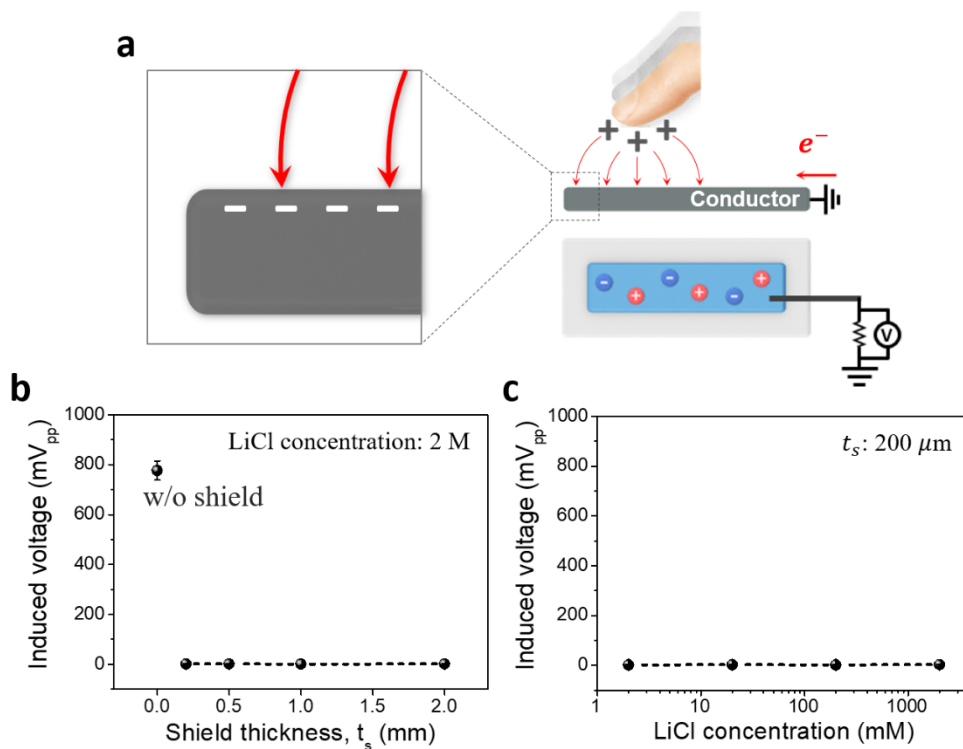


Fig. 3.7 **(a)** Schematic illustration of the mechanism of electric field shielding of a grounded conductor. An external electric field induces an accumulation of excess charges on the surface of the grounded conductor, preventing transmission of the electric field. **(b)** induced voltage was measured as the thickness of the hydrogel conductive shield was varied. **(c)** The lithium chloride (LiCl) concentration did not influence the shielding efficiency of the grounded hydrogel. Error bars represent SD ( $n=3$ ).

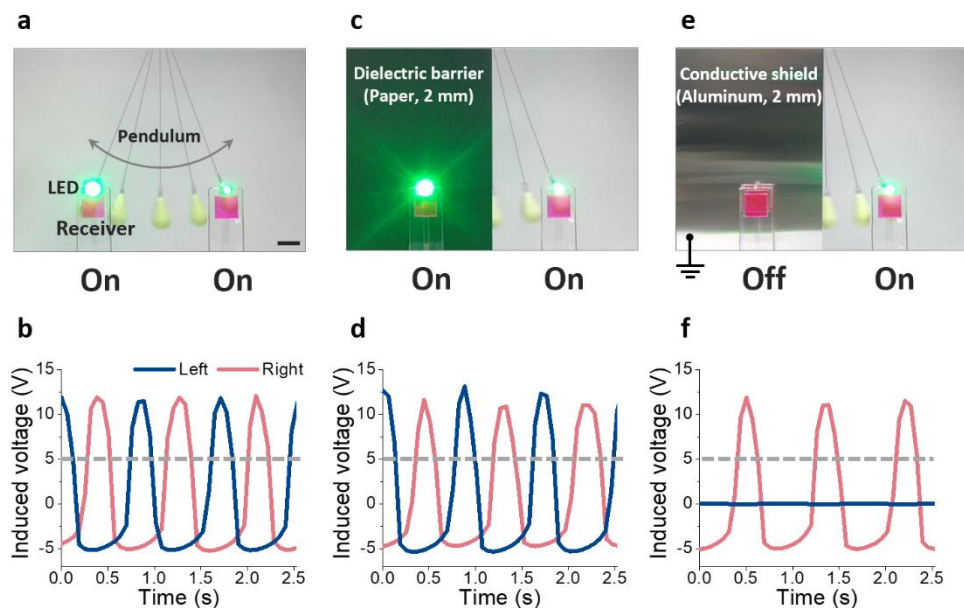


Fig. 3.8 **(a, b)** A SIPS with two hydrogel electric field receivers was placed in front of an oscillating pendulum. SIPSs can be used as proximity switches that can sense the presence of an object. **(b)** LEDs were programmed to be turned on when the induced voltages exceeded a threshold voltage (5 V). **(c, d)** A dielectric barrier was placed between the oscillating pendulum and the receiver on the left side. **(d)** The SIPS can be used to sense the presence of the object behind the dielectric barrier. **(e, f)** A conductive shield was placed between the oscillating pendulum and the receiver on the left side. **(f)** The conductive shield effectively blocked the transmission of the electric field originating from static charges on the surface of the pendulum. To enhance the contrast between the hydrogels and background, fluorescent dyes were added to the hydrogel electric field receivers. Scale bar, 4cm.

#### 3.3.4. A wearable SIPS for spatial perception

To enable transmission of the voltage signal from the electric field receiver to the external load, the receiver is connected to a data line (Fig. 3.9a). However, even if the data line is encapsulated with an elastomer, it can also act as an electric field receiver because the electric field can be transmitted through the elastomeric encapsulation. Undesirable transmission can cause distortion of the voltage signal by the data line. However, to accurately detect the relative position of an object by comparing the voltage signals from networks of hydrogel electric field receivers, the voltage induction must be a function of only distance to the object, regardless of the object direction. Thus, the hydrogel conductive shield was used to prevent the object-originated electric field from reaching the data line (Fig. 3.9b). Thus, the SIPS was capable of consistently detecting the object regardless of its direction when the data line was covered by the conductive shield.

To support human spatial perception in daily life, a wearable SIPS was fabricated using a 3D printer (Fig. 3.10a). The SIPS was composed of four different layers: a cover layer, two shielding layers, and a sensing layer (Fig. 3.10b, c). The sensing layer was composed of four hydrogel electric field receivers printed on the elastomer, and the shielding layers were composed of a hydrogel conductive shield printed on the elastomer. To accurately detect nearby objects, the sensing layer was sandwiched between the two shielding layers. The bottom shielding layer blocks electrical noise from the subject's hand, and the top shielding layer prevents data lines from distorting the voltage signal. By comparing the amplitude of the voltage induced in each hydrogel electric field receiver, the SIPS could be used to estimate the relative position of an object (Fig. 3.10d). In addition, the SIPS with four hydrogel receivers could distinguish between eight relative object positions, and the

addition of extra receivers to the sensing layer would potentially allow the SIPS to identify more complex spatial relationships.

To characterize the wearability of the SIPS, it was attached to the hollow of the subject's hand (Fig. 3.10a). Because the SIPS was composed of soft materials only, it could be deformed smoothly and comfortably with the skin. The robust hydrogel/elastomer interface allowed the SIPS to withstand mechanical strain caused by hand movements without notable delamination. Moreover, high transparency enabled continuous inspection of the skin covered by the receptor [69].

To support human spatial recognition, the wearable SIPS was programmed to transmit spatial information of a nearby object via auditory signals (Fig. 3.11a, b). Auditory signals with frequencies of 0.5, 1.0, 1.5, and 2 kHz corresponded to relative positions of right, back, front and left, respectively. The threshold voltage was set at 0.3 V in order to distinguish object-related signals from ambient noise. When the amplitudes of all voltage signals were below the threshold voltage, the SIPS remained in the standby-state. The SIPS turned to the alert-state when more than one amplitude of the voltage signals exceeded the threshold voltage, and the auditory signal corresponding to the object's position was transmitted to the person wearing the receptor. Thus, by wearing the SIPS, a person who is blind or visually impaired can recognize the relative positions of surrounding objects without any unwanted physical contact.

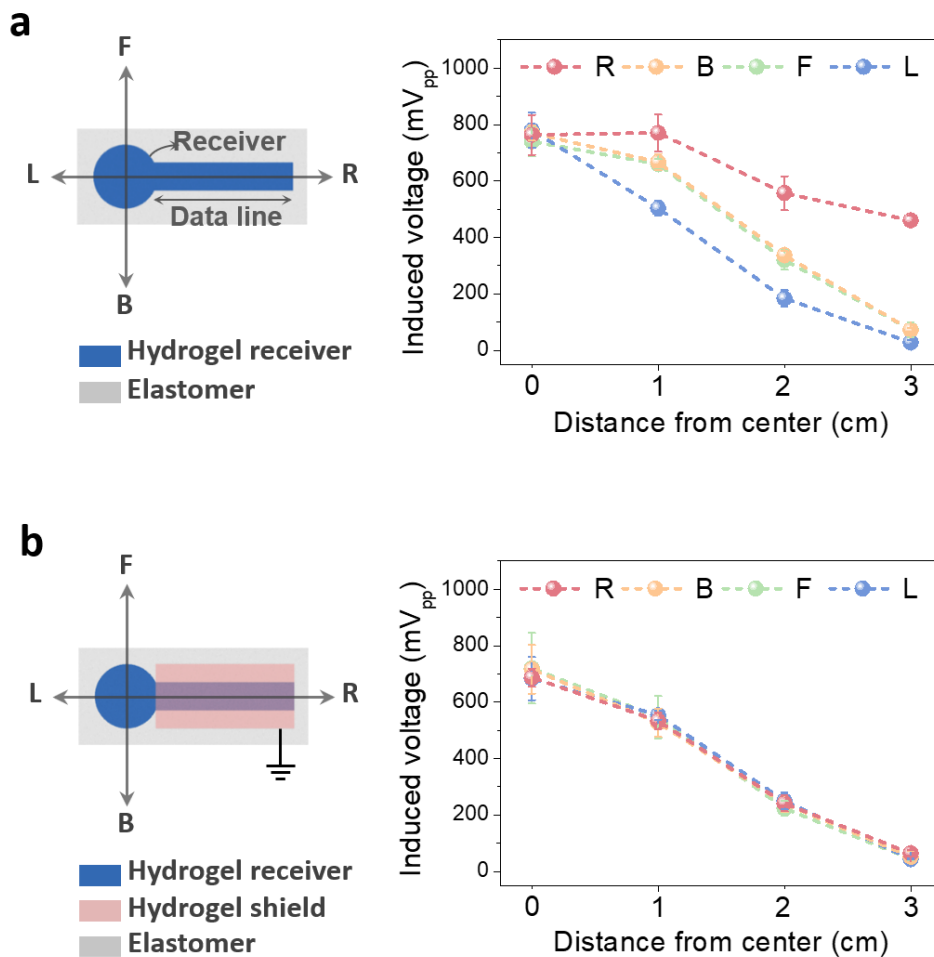


Fig. 3.9 **(a)** Without the conductive shield, the sensing capability of the SIPS shows anisotropy because of the data line connected to the electric field receiver. **(b)** When the data line is covered with a hydrogel conductive shield, the sensing capability of the SIPS shows isotropy. Error bars represent SD ( $n=3$ ).

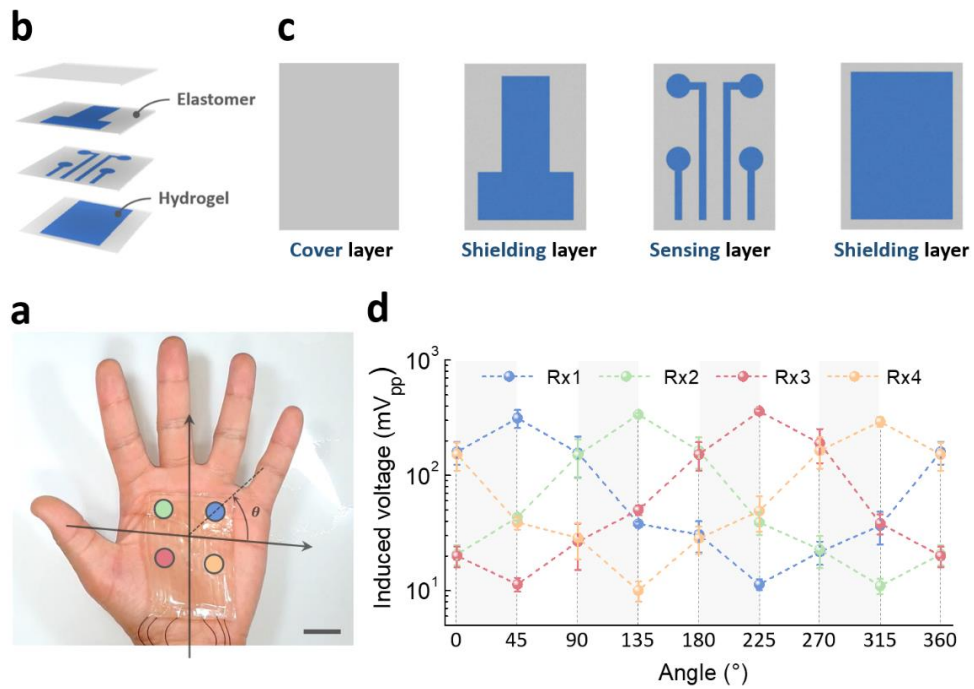


Fig. 3.10 **(a)** The wearable SIPS was attached to the hollow of the hand. **(b, c)** Schematic describing each 3D-printed layer in a wearable SIPS. **(b)** Exploded view of the SIPS composed of hydrogels printed on elastomer layers. **(c)** A sensing layer with four hydrogel electric field receivers was sandwiched between two shielding layers. The bottom shielding layer blocks electrical noise from a hand and the top shielding layer prevents signal distortion by the data line. **(d)** By comparing the intensity of the electric fields sensed by each hydrogel receiver, the SIPS can be used to identify the relative position of the object. Error bars represent SD ( $n=3$ ). Scale bar, 2 cm.

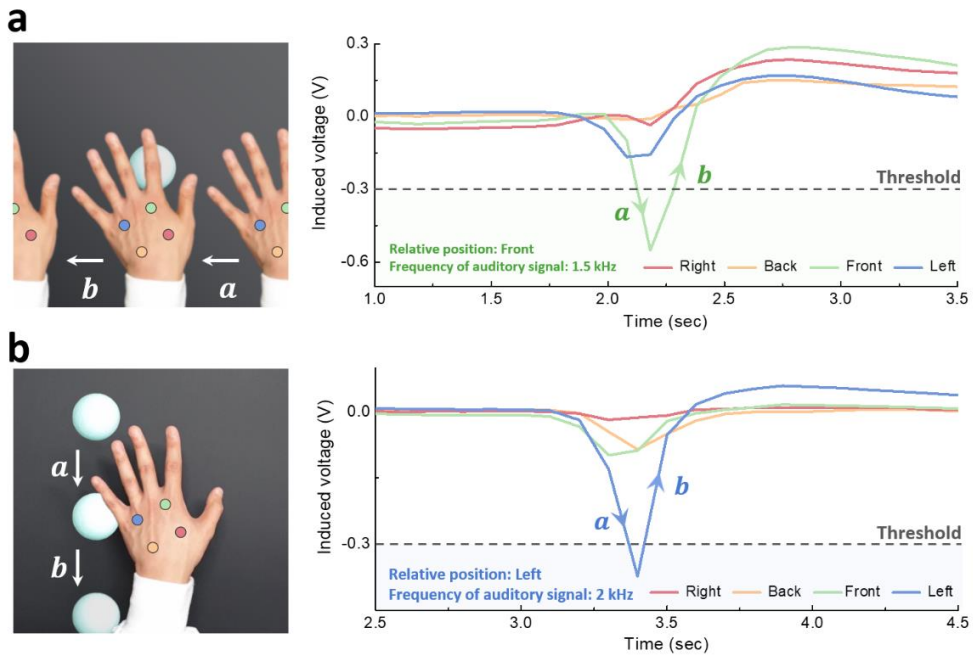


Fig. 3.11 A wearable SIPS for spatial perception. **(a, b)** By wearing the SIPS, a person can perceive spatial information related to a static (a) and dynamic (b) object via auditory signals.

### **3.4. Conclusion**

Inspired by how rays locate their prey, we developed a SIPS that emulate the ability to sense electric fields. As with the animal's electroreceptors, ion-conductive hydrogels were used as soft electric field receivers. For rapid and elaborate fabrication, network of hydrogel receivers was 3D-printed on an elastomer. By covalently anchoring the hydrogels to the elastomer during the printing process, a robust hydrogel/elastomer interface capable of withstanding the mechanical strain caused by human movement was formed. In the same manner as the electroreceptors of the animals, the fabricated SIPS could detect the relative position of nearby objects by comparing the intensity of the object-originated electric fields sensed by each hydrogel receiver in the network. Because electric fields can be transmitted through dielectric materials, the SIPS could be used to detect objects even if they were behind a wall. Moreover, the sensing capability of the SIPS was boosted more than 130-fold based on the theoretical analysis. By wearing the SIPS, a person can receive spatial information related to a nearby object in real time via auditory signals. The artificial electroreceptor expands the way in which humans can perceive space by providing a new sensory modality that did not evolve naturally in human beings.

## **Chapter 4. Multi-functional ionic soft robots**

### **4.1. Introduction**

Most robots are built using rigid materials. These robots are designed to efficiently carry out preplanned task but the robots are struggling to operate in unstructured environments because they are composed of discrete links and joints. Desire for compliant robots has led to the development of soft-bodied robots [84-92]. Since the continuously deformable bodies of soft-bodied robots give them a high degree of freedom, they can flexibly handle irregular tasks in a less complicated manner than traditional robots. In addition, they can safely and comfortably interact with humans because they are composed of compliant materials that have an elastic modulus similar to that of the soft tissues found in biological systems.

While the individual soft components, such as actuators, sensors, and so on, have been tremendously well-researched, the effort to combine individual components into a single system remains in its infancy. Systemization of the well-established individual components is an essential prerequisite for real-world application of hydrogel-based soft robotics. Beyond simple physical combining, complementary interactions between all components promise to fulfill the maximum potential of soft robotics - the ability to operate without further intervention. At the same time, the systemization process should not deteriorate the compliancy of the soft robots; care must be taken to preserve their unique features

In nature, spiders use adhesive, stretchable, and translucent webs to capture their prey. However, sustaining the capturing capability of these webs can be challenging because the webs inevitably invite contamination, thus reducing its

adhesion force. To overcome these challenges, spiders have developed strategies of using webs to sense prey and vibrationally clean contaminants (Fig. 4.1a) [93-104].

In this Chapter, multi-functional ionic soft robots, equipping abilities to capture, sense, and actuate, were demonstrated based on electrostatics inspired by capturing strategies of spiders (Fig. 4.1 and 4.2). Adhesion capability of the robots was boosted by preventing from contamination using vibrational actuating and sensing capability. The mutually complementary multi-functions were combined into a structure of TENGs without additional assembly. A potential issue of electrochemical reactions in ionic conductors was investigated. The robot was fabricated with ionically conductive and stretchable organogel encapsulated with silicone rubber to form a strand shape (Fig. 4.3 and 4.4) [105-107]. The organogel consists of covalently cross-linked polyacrylamide (PAAm) chains and ethylene glycol (EG) dissolving lithium chloride (LiCl) (Fig. 4.3c). Plasma etching and (heptadecafluoro-1,1,2,2-tetrahydrodecyl) trichlorosilane (HDFS) treatment of the silicone rubber markedly boosted cleaning capability and prevented evaporation of the organogel, which enhanced the durability of ISWs (Fig. 4.5a) [85, 108]. In addition, similar to the structural thread of spiderwebs, nylon thread was used as the framework for ISWs to reinforce their mechanical properties (Fig. 4.6b-d).

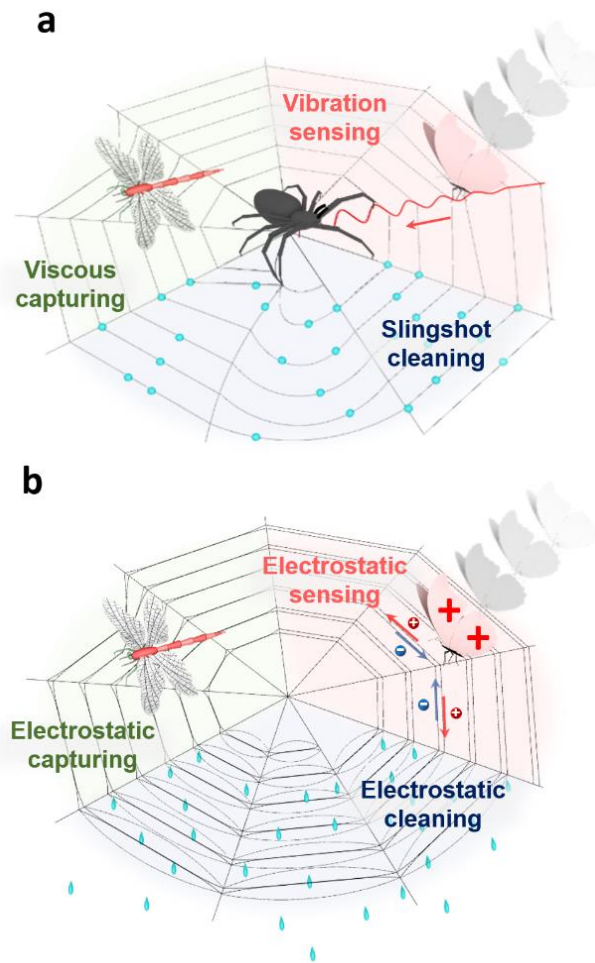


Fig. 4.1 (a) Spiders can sense and clean using their webs alone, and these functions act synergistically to capture their prey. (b) Ionic spiderwebs (ISWs) emulating the capturing strategies of a spider.

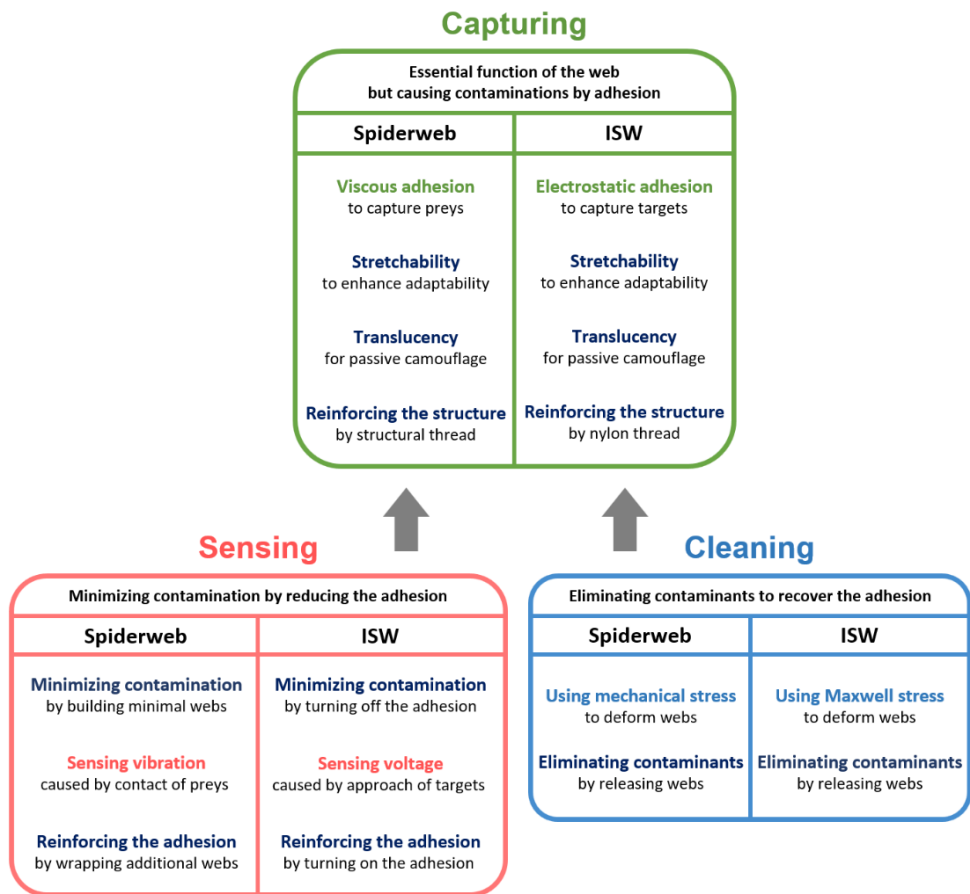


Fig. 4.2 ISWs emulating the optimized capturing strategies of spiders. Spiders have used their own unique capturing strategies. ISWs are made to emulate spider's outstanding capturing strategies.

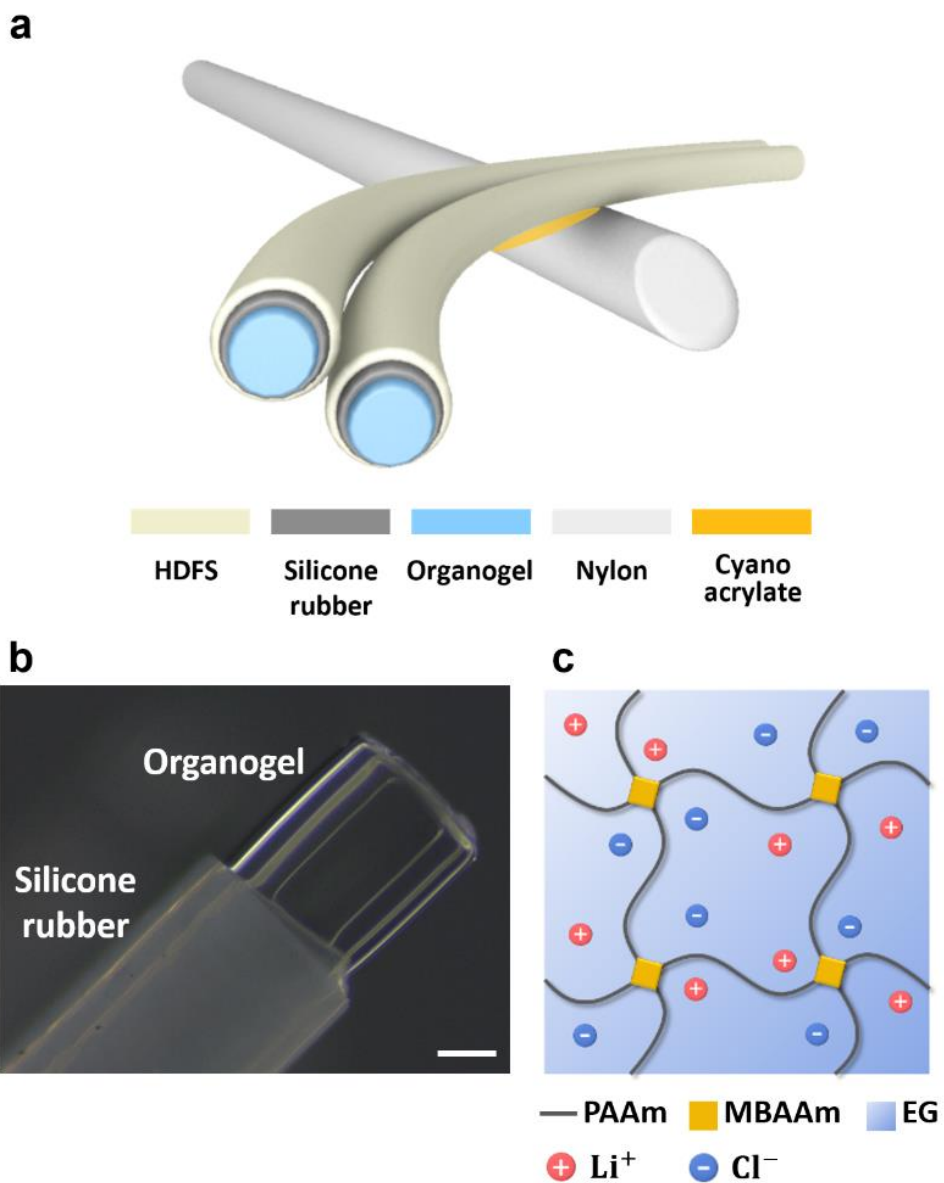


Fig. 4.3 **(a)** Schematic illustration describing the structural design of a fabricated ISW. **(b)** Magnified image of an ISW. Transparent organogel is capsulated with translucent silicone rubber. Scale bar, 200  $\mu\text{m}$ . **(c)** Chemical structures of an ionically conductive organogel consisting of EG dissolving LiCl and PAAm chains cross-linked by MBAAm.

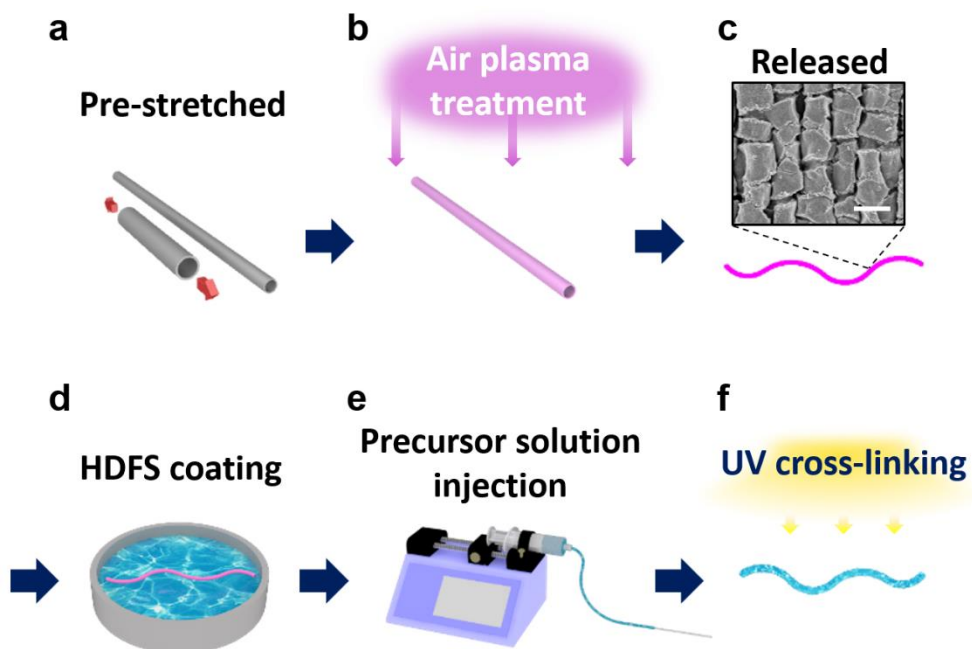


Fig. 4.4 Fabrication process of an ISW. **(a-f)** Pre-stretched silicone tubes **(a)** were treated with air plasma **(b)** and released to obtain wrinkled surfaces **(c)**. Treated tubes were immersed in a solution with HDFS for self-assembly monolayer coating **(d)** [108]. Organogel precursor solution was injected into the tube **(e)** followed by 365 nm UV irradiation in inert condition for 5 minutes **(f)**. Scale bar, 1  $\mu\text{m}$ .

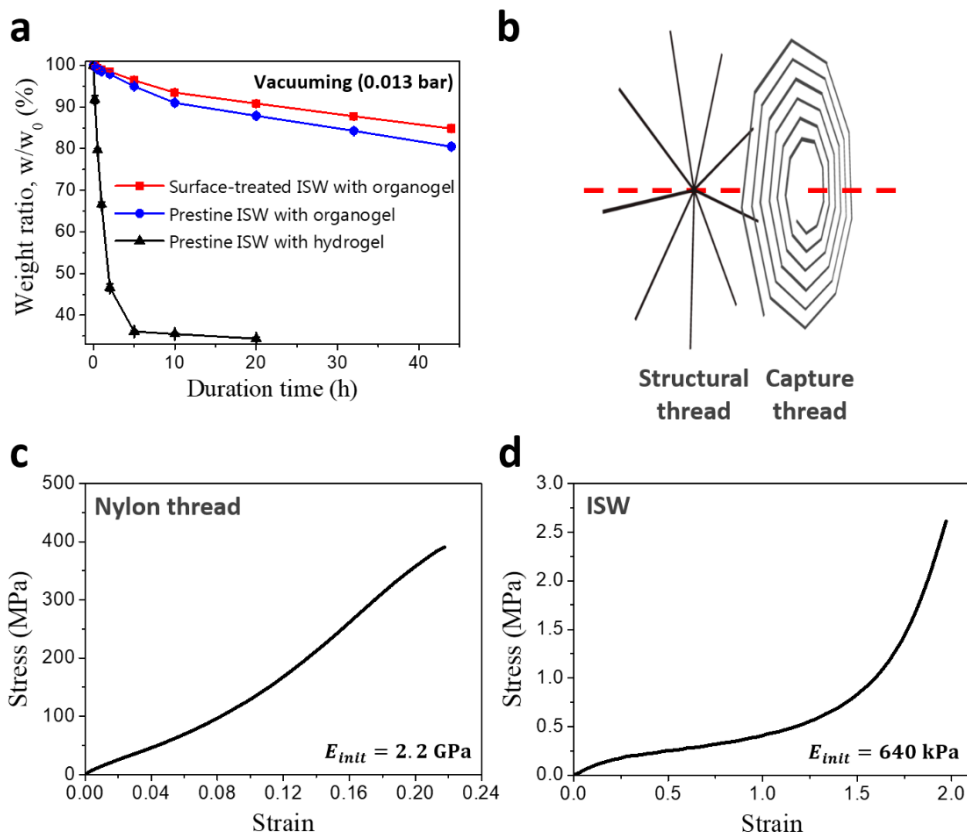


Fig. 4.5 **(a)** Anti-dehydration capability of ISWs under harsh conditions. Organogel with a vapor pressure of 0.5 kPa evaporates relatively slower than hydrogel with a vapor pressure of 2.3 kPa [90]. Surface treatment prevented evaporation of organogel by lowering the vapor permittivity of silicone rubber [108]. **(b)** Exploded view of orb spiderwebs. Spiders spin adhesive, stretchable, and translucent capture thread on strong structural thread. **(c, d)** Stress-strain curve of tensile test. (c) Stiffness and extensibilities of nylon thread were 2.2 GPa and 0.21, respectively. (d) Stiffness and extensibilities of ISW were 640 kPa and 1.9, respectively. Error bars represent SD ( $n=3$ ).

## 4.2. Experimental section

### 4.2.1. Materials and specimen preparation.

Unless otherwise specified, ISWs were fabricated using a PAAm organogel containing LiCl. Acrylamide (AAm; Sigma, A8887) and N,N-methylenebisacrylamide (MBAAm; Sigma, M7279) were used as monomers and cross-linkers for the organogel, respectively. EG (Dae-Jung, 4026-4404) was used as a liquid constituent. LiCl (Sigma, L4408) was used as an ionic charge carrier. Lithium phenyl-2,4,6-trimethylbenzoylphosphinate (LAP; Sigma, 900889) was used as a photo initiator. Silicone tubes with inner diameters of 500  $\mu\text{m}$  and outer diameters of 600  $\mu\text{m}$  (Axel, 1-8194-05) were used as dielectrics in ISWs. HDFS (JSI Silicone Co, H5060.1) was used as surface fluorination agent. Ethyl cyanoacrylate (Henkel, Loctite 406) and a primer (Henkel, Loctite SF770) were used to bond ISWs to nylon threads with a diameter of 0.52 mm (Ourix, Shock Leader) [109]. Platinum electrodes were used to connect the organogel with electrical circuits.

### 4.2.2. Preparation of organogel precursor solution.

Unless otherwise specified, the ionic organogel was synthesized by dissolving AAm and LiCl in EG. The molar concentrations of the AAm and LiCl solutions were 3.5 and 1.5 M, respectively. MBAAm [0.124 weight % (wt %)] and LAP (0.012 wt %) with respect to the weight of AAm were added.

### 4.2.3. Fabrication of ISWs.

Unless otherwise specified, surface etching of prestrained (150%) silicone tubes was conducted using an air plasma processing system (FEMTO SCIENCE, COVANCE-IMPR) under conditions of 200 W, 1 hour, and 15 sccm (standard cubic centimeters per minute). The silicone tubes were immersed in a solution of HDFS and hexane mixed at a ratio of 1:500. Self-assembled monolayer formation took

place for 20 min. Treated ISWs were then washed with hexane for 10 min. Organogel precursor solution was injected into surface-treated silicone tubes, followed by 365-nm ultraviolet irradiation (CL-1000L, UVP) under inert conditions for 5 min. Pretreatment using a primer was carried out on ISWs at the intersection with nylon thread to promote wetting of the adhesive [109]. A pair of ISWs was bonded to nylon threads using ethyl cyanoacrylate. A stereomicroscope (Stereo Discovery V12, Zeiss) was used to observe the fabricated ISW.

#### 4.2.4. Characterization and measurement of electrostatic adhesion capturing

For all measurements of electrostatic adhesion force, a universal testing machine (Instron, 3343) with a static load cell (Instron, 2530-50N) was used at a fixed receding rate of 3 mm/min. Targets and ISWs were fixed in place with a custom acrylic holder. Unless otherwise specified, the adhesion force of ISWs was measured using aluminum as a target under 5 kV of applied voltage. ISWs were connected to a power source via Pt electrodes. A function generator (Agilent, 33612A) with a high-voltage amplifier (Trek, 30/20A) was used as a power source for electrostatic adhesion capturing. The leakage current was measured using a multimeter (Agilent, 34461A). Adhesion force per unit area was calculated in a projection area in which the sample and target met.

#### 4.2.5. Demonstration of stretchable electrostatic adhesion net

Four pairs of ISWs were fixed parallel to the holders. The gaps between each pair were 1 cm, whereas the gap between threads in a pair was 3 mm. The ISW was manually stretched from 8 to 12 cm under the applied voltage. To release the target, 3 kV of AC voltage with an offset of 1.5 kV and a frequency of 30 Hz were

applied to the ISW. The targets consisted of aluminum at sizes of 5 cm by 5 cm by 0.1 cm (6.8 g) and 10 cm by 5 cm by 0.1 cm (13.6 g).

#### 4.2.6. Test of contamination

Contamination was tested using a cubic-shaped acrylic system (1.73 L). ISWs were set at the center of the system. Each ISW was kept under adhesion ON-state and OFF-state, respectively. Ten grams of silica powder with an average particle diameter of 50  $\mu\text{m}$  was then scattered using a fan for 50 s, and adhesion force was measured every 10 s during this time. An inverted microscope (Olympus Korea, CKX41- A32PH standard) was used to observe contamination on the surface of the ISWs.

#### 4.2.7. Characterization and measurement of electrostatic induction sensing

Unless otherwise indicated, ISWs were connected to an external load of 5 gigohms. An electrometer (Keithley, 6517A) was used to measure induced voltage across the external load. A pushing tester (Labworks, LW139.138-40) with a linear power amplifier (Labworks, PA-138) was used to provide vertical linear motion of the targets. A glass target was charged by rubbing with PFA. The targets moved in a sinusoidal pattern with a frequency of 1 Hz. The reference distance and amplitude were 1 and 0.75 cm, respectively. All measurements of electrostatic induction sensing were conducted in a Faraday cage to prevent ambient electrical noise. To show interactions with a computer, LabView (National Instruments) was used for programming.

#### 4.2.8. Characterization and measurement of electrostatic vibration

cleaning

A function generator (Agilent, 33612A) with a high-voltage amplifier (Trek, 30/20A) was used as a power source to provide sinusoidal high voltages. To measure the vibration amplitude of ISWs, a highspeed camera (Phantom, V611-32G-MAG) that could run up to 6242 frames per second was used. Contact angles of deionized water on ISW were measured with a contact angle analyzer (FEMTOFAB, Smart Drop) at room temperature. An x-ray photoelectron spectrometer (Kratos, AXIS-HSi) was used to characterize functionalized ISWs. A field-emission scanning electron microscope (Carl Zeiss, Sigma) was used to observe surface morphology of ISWs. To investigate cleaning capability of ISW, 10 g of silica powder and a 5  $\mu$ l water droplet were used as contaminants. The frequency of the applied voltage was swept from 45 to 100 Hz for 20 s.

#### 4.2.9. Recording of slingshot cleaning by a spider

The slingshot cleaning behavior of a *C. japonica* specimen was recorded in Galsan-dong, Seosan-si, Chungnam, South Korea.

### 4.3. Results and discussion

#### 4.3.1. Capturing by electrostatic adhesion

Spiders firmly capture various types of prey using their adhesive and stretchable webs. To emulate the capturing capability of these webs, electrostatic adhesion capturing was realized through the mechanism shown in Fig. 4.6 [110, 111]. In the OFF-state ( $V_{\text{applied}} = 0$ ), the two threads remain separated (Fig. 4.6a). When a high voltage was applied, the ions were aligned along the organogel/silicone rubber interface of each thread, resulting in Maxwell stress between the threads (Fig. 4.6b) [86]. As the threads moved closer, generation of a stronger electric field led to

polarization in a target. The charge induced by polarization was attracted by the external electric field, and electrostatic adhesion occurred between the ISW and the target (Fig. 4.6c). Electrochemical reactions at the interface between an organogel and the metal electrode can be an issue [86]. However, the electrostatic adhesion is based on a capacitive system. No electrochemical reaction occurs in the ISW even if high voltage is applied. At equilibrium state, the input voltage between the two threads is carried entirely by the two EDL and the dielectric,  $V_{applied} = 2V_{EDL} + V_D$ , where  $V_{EDL}$  is the voltage across EDL and  $V_D$  is the voltage across dielectrics. According to the applied voltage, the three capacitors meet the same amount of charge,  $c_D A_D V_D = c_{EDL} A_{EDL} V_{EDL}$ , where  $A_{EDL}$  is area of the EDL,  $A_D$  is area of the dielectric,  $c_{EDL}$  is areal capacitance of the EDL, and  $c_D$  is areal capacitance of the dielectrics. In this study, the ratio between voltage was on the order of  $V_{EDL}/V_D \sim 10^{-5}$ , because the ratio between area was on the order of  $A_{EDL}/A_D \sim 0.01$  and ratio between areal capacitance was on the order of  $c_{EDL}/c_D \sim 10^7$ . Thus, voltage across the EDL  $V_{EDL}$  was well below 1 V when the applied voltage is on the order of  $V_{applied} \sim 10$  kV and no electrochemical reaction occurred except for the electrochemical reaction caused by minute leakage current, which was less than 2.3 nA/cm (Fig. 4.7a) [86]. Although unwanted electrochemical reactions may be negligible, the ISWs can undergo breakdown if the electric field across dielectrics exceeds the dielectric strength of silicone rubber (50 to 100 kV/mm) [92]. To address this safety issue, the leakage current was continuously measured to allow for immediate shut down of the applied voltage when a sudden increase in leakage current was sensed (Fig. 4.7b, c). To obtain a reproducible measurement of the electrostatic adhesion force, a universal testing machine with a custom acrylic holder was used (see Experimental section for details). As the applied voltage increased from 2 to 9 kV, the adhesion force per unit

area improved from 0.1 to 0.3 kPa and 0.2 to 1.1 kPa when the target was poly(methyl methacrylate) (PMMA) and aluminum, respectively (Fig. 4.8a). The adhesion force was investigated with a variety of target materials—such as metals, ceramics, polymers, and natural materials—under a constant applied voltage of 5 kV (Fig. 4.8b). The highest adhesion force of 0.9 kPa was measured for metals, which have the highest dielectric constant, followed by ceramics (0.7 kPa) and polymers (0.25 kPa). This was because the higher the dielectric constant of the targets, the larger the polarization in the target under the same electric field. The conductivity of the organogel can be controlled by ion concentration. Figure 4.8c shows the effects of LiCl concentrations ranging from 0.15 mM to 1.5 M on the adhesion force. Ion concentration in the gel did not influence the adhesion force. The forces generated by electrostatic adhesion were investigated at varying tilt angles (Fig. 4.9a). The adhesion force increased by up to 6.5-fold when the ISW was tilted  $80^\circ$  from the horizontal, suggesting that ISWs can achieve substantial strength when tilted at a large angle [112, 113]. All components of the ISW are made of soft materials and can therefore be stretched. When a 50% strain was applied, adhesion force increased by 37%, as shown in Fig. 4.9b. A decrease in thickness of the silicone rubbers caused by stretching led the gels in a pair of ISWs to be closer to each other. This contributed to the generation of a stronger electric field, thus enhancing the electrostatic adhesion force. To demonstrate capturing capability, four pairs of ISWs were fixed at 1-cm intervals in a zigzag pattern and tilted approximately  $80^\circ$  relative to the horizontal (Fig. 4.9c). Because of the simple structure, 0.2 g of ISWs was able to capture 6.8 g of an aluminum plate. The ISWs readily expanded to 50% of strain in the longitudinal direction and were able to capture a heavier target (13.6 g). Because the

stretched ISWs were under tension, they showed less deflection when capturing a target.

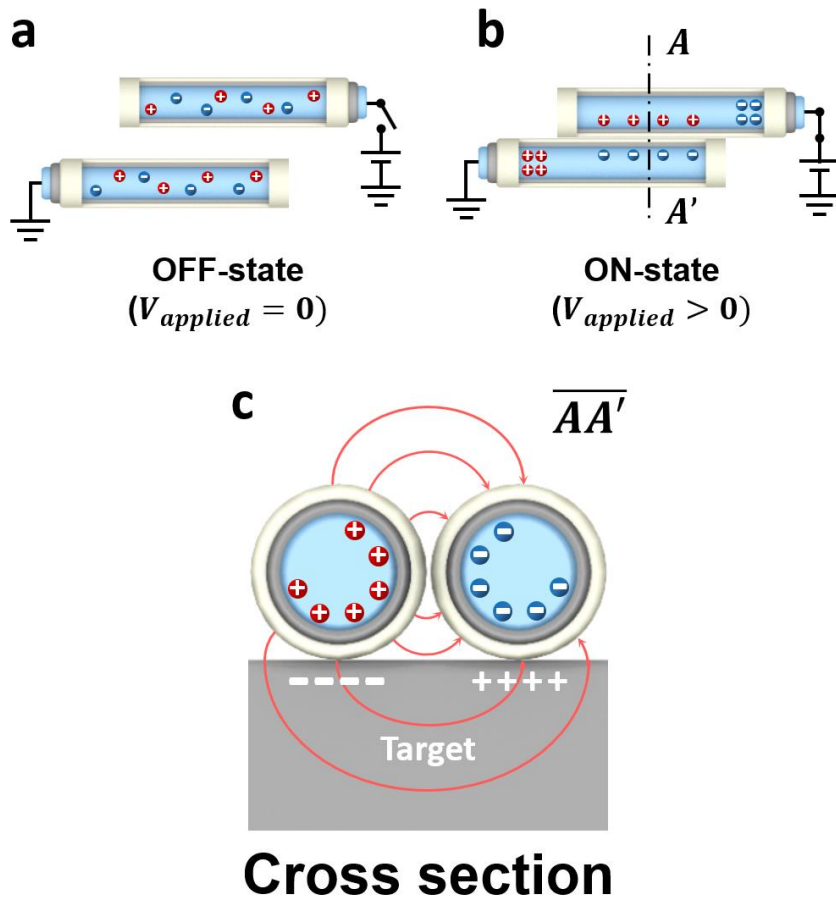


Fig. 4.6 (a-c) Schematic diagrams illustrating the working mechanism of electrostatic adhesion capturing in the OFF-state ( $V_{\text{applied}} = 0$ ) (a) and ON-state ( $V_{\text{applied}} > 0$ ) (b) with a cross-sectional view (c). The electric field generated by the potential difference between a pair of ISWs induces polarization in a target, leading to electrostatic adhesion capture.

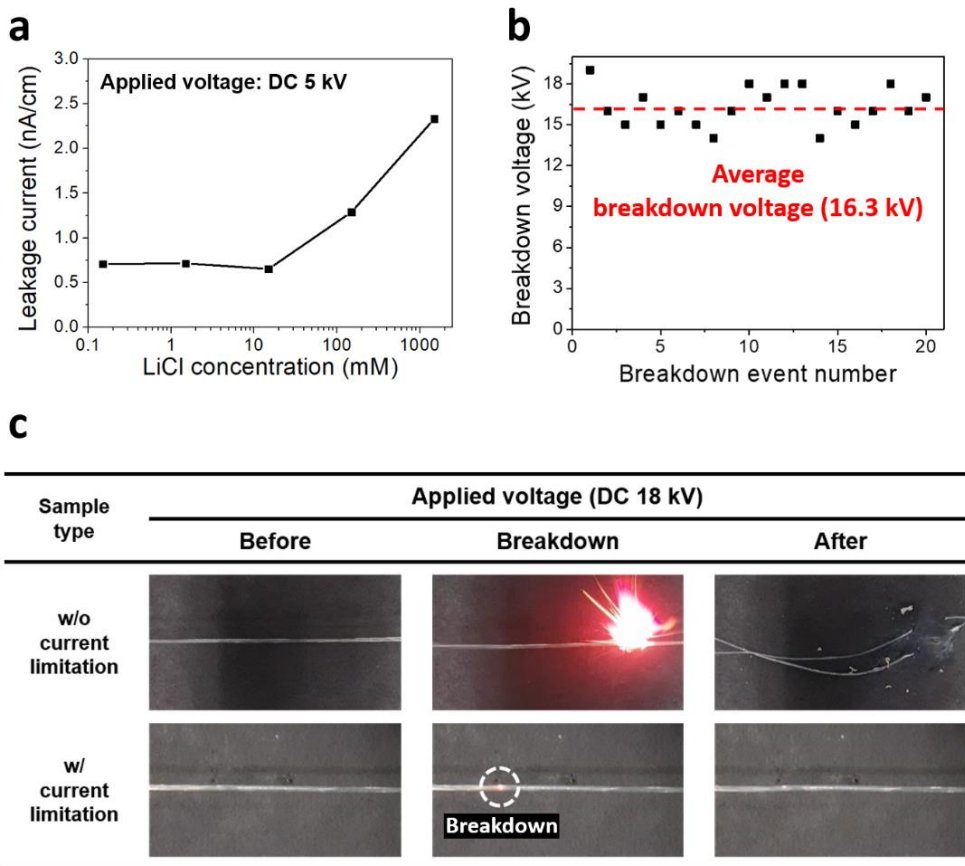


Fig. 4.7 **(a)** Leakage current of ISW. In a wide range of LiCl concentrations from 0.15 mM to 1.5 M, there was insignificant leakage current. **(b)** Breakdown voltages of ISW. Maximum applied voltages that ISW can endure were measured. The average breakdown voltage was measured as 16.3 kV. **(c)** Dielectric breakdown behavior of ISW. When breakdown occurs, sudden increase of the leakage current causes the destruction of ISW. Therefore, leakage current was measured, so that the applied voltage could be shut down when increase of leakage current is detected.

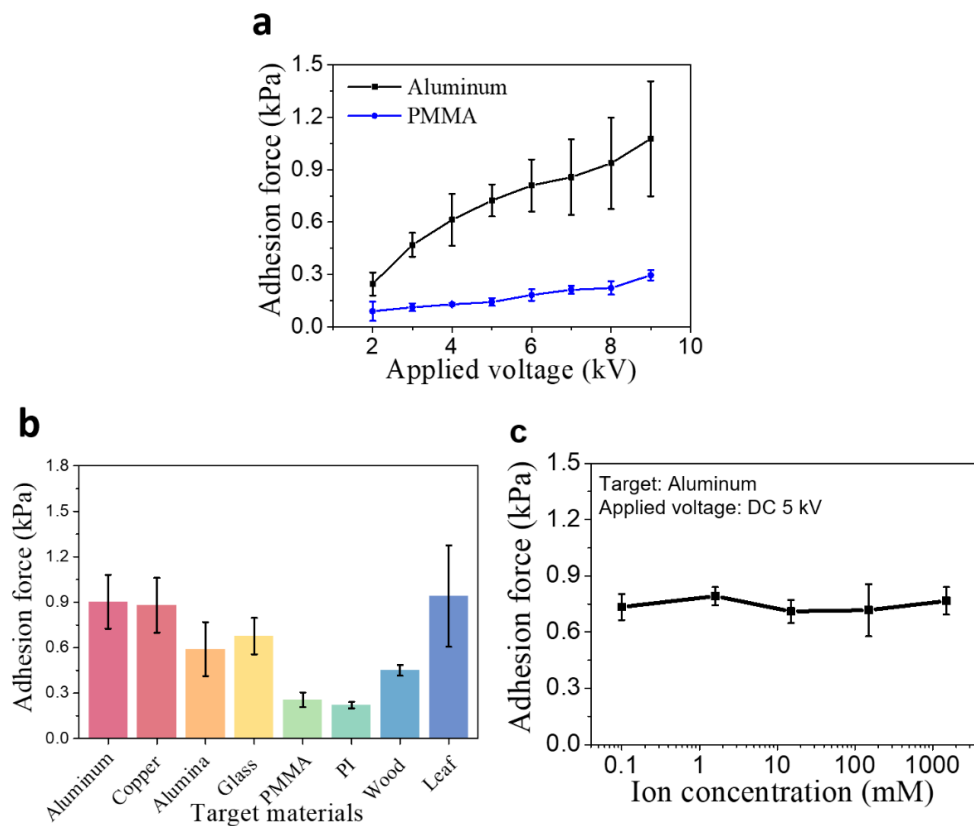


Fig. 4.8 (a-c) Adhesion force was investigated as a function of applied voltages (a), target materials (b), and ion concentrations in the organogel (c). Error bars in the figures represent SD (n = 5).

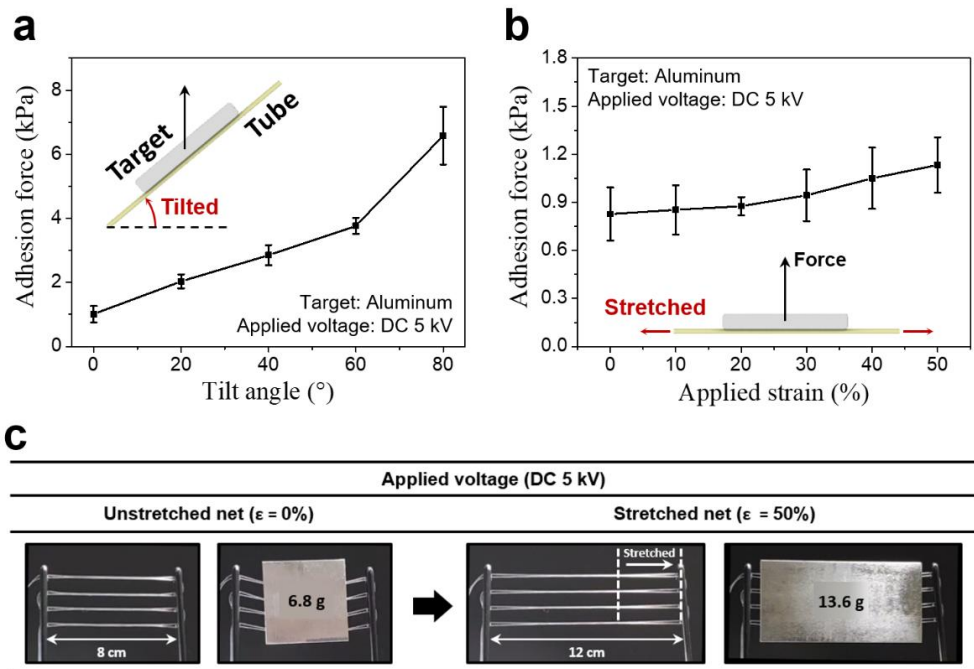
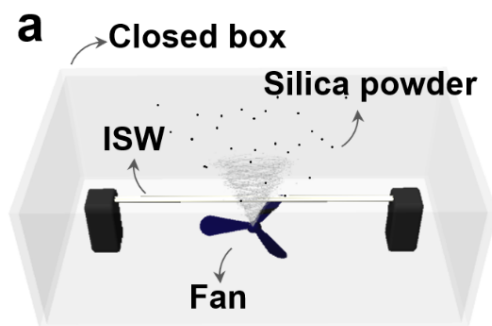


Fig. 4.9 (a, b) Adhesion force was investigated as tilt angle (a) and applied strain (b). (c) Four pairs of ISWs capturing a 6.8 g aluminum plate. When 50% strain was applied, the ISWs captured a 13.6 g aluminum plate. Error bars in the figures represent SD (n = 5).

#### 4.3.2. Sensing by electrostatic induction

One of the major concerns for spiders capturing prey is contamination of webs due to their strong adhesion force. Similar to spiderwebs, the adhesion force of an ISW can attract undesirable contaminants. For example, an air circulation system that scatters dense particles of dust can accelerate contamination (Fig. 4.10a and Experimental section for details), and the electrostatic adhesion force of an ISW in the ON-state was substantially reduced to 1.8% after 50 s. Meanwhile, an ISW in the OFF-state still maintained 58.5% of its initial adhesion force because an ISW in the OFF-state was less contaminated compared with an ISW in the ON-state as shown in magnified images (Fig. 4.10b, c). To minimize contamination, spiders use a sensing strategy that allows them to build minimal webs. Inspired by this strategy, ISWs were equipped with a sensing capability that allowed them to turn on electrostatic adhesion only when a target is nearby. In this way, ISWs can minimize contamination by reducing the operating time of electrostatic adhesion. As described in Fig. 4.11a, b, making contact with the surroundings can charge the target through contact electrification [114-116]. Approach of a charged target induces a voltage in the ISWs. Thus, measuring the voltage across an external load allows the relative distance between the ISW and the target to be measured. A target with no surface charge cannot be sensed. However, approaching targets can be sensed in most cases because they will be charged not only when they come into contact with other types of materials—including solids, liquids, and vapors— but also when they come into contact with the same type of material they are made of [117-120]. Meanwhile, static objects around an ISW do not affect its sensing capability, because voltage is induced only when objects move (Fig. 4.11c-f). Because electrostatic induction sensing converts the mechanical energy of a target to an electrical signal, it has the advantage

of negligible power consumption compared with existing proximity sensing technologies [121]. A pushing tester was used to reproducibly control the distance and approaching speed of the targets (Fig. 4.12a). Static charges were created on the surface of a target by rubbing a glass with various charging materials (see Experimental section for details). The sensing capability was tested with various gap distances ( $d$ ), ranging from 0.5 to 1.5 cm, under a sinusoidal wave of 1 Hz (Fig. 4.12b). These measured voltages closely traced the position of the target. Because switching from sensing mode to capturing mode takes time, it is essential to sense the approach of a target before contact occurs and then turn on electrostatic adhesion in advance. To obtain the highest sensitivity, the induced voltages were measured with various external loads. The induced voltage was enhanced with increasing resistance of the external load under various target approach speeds of a target (Fig. 4.12c). The induced voltage was measured when the target was charged by various materials, such as alumina, aluminum, PMMA, leaf, copper, polyimide, and perfluoroalkoxy alkane (PFA) (Fig. 4.12d). Perceptible values of  $0.11 V_{pp}$  were measured even when the target was charged with alumina, which is known to have an electron affinity similar to that of the target [122]. A circuit was fabricated to demonstrate how an ISW could sense an approaching target and then turn on a power source using a preprogrammed computer (Fig. 4.13a). When the induced voltage exceeded a threshold voltage of 0.1 V for sensing, the computer allowed the power source to operate. As shown in Fig. 4.13b, c, a green light-emitting diode (LED) was turned on when an ISW sensed the approach of a target.



**Accelerated contamination test system**

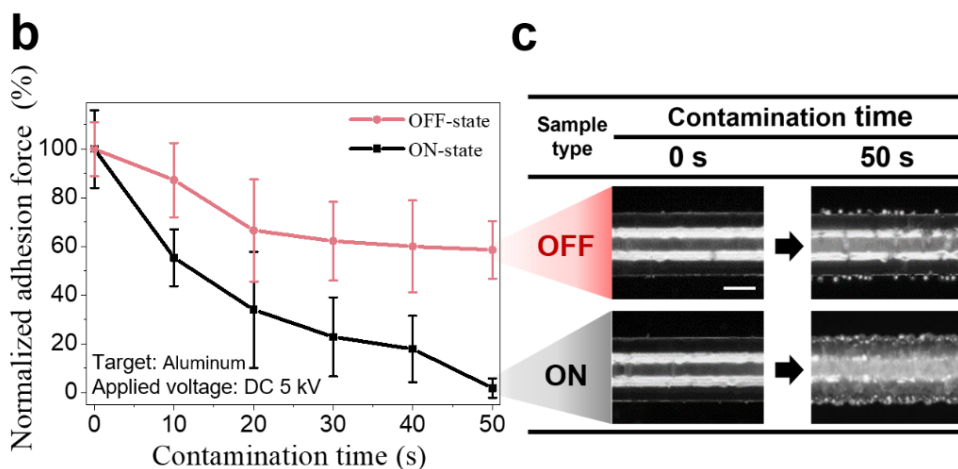


Fig. 4.10 (a) Air circulation system that scatters dense dust to accelerate contamination. (b) Normalized electrostatic adhesion forces of ISWs after exposure to contaminants in the ON-state and OFF-state. (c) Contaminated surfaces of ISWs. Scale bar, 150  $\mu\text{m}$ . Error bars represent SD ( $n = 5$ ).

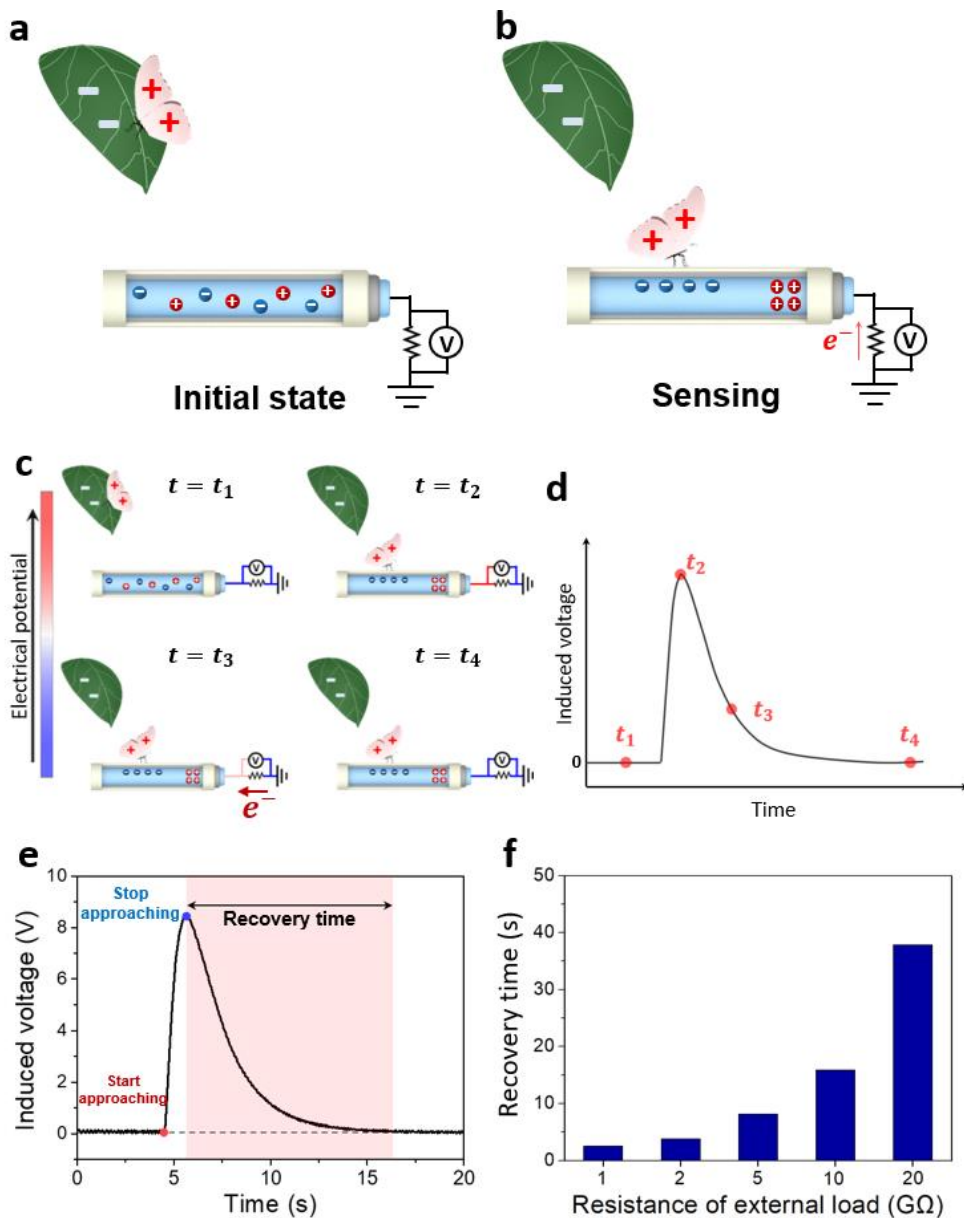


Fig. 4.11 (a, b) Schematic diagrams showing the working mechanism of electrostatic induction sensing. (c, d) Schematic describing a detailed sensing mechanism (c) and graph of induced voltage over time (d). Even if charged objects exist around the ISW, they do not affect the sensing capability of ISW unless they move. (e, f) Experimental results describing the effect of static objects around the ISW. (e) Recovery time is the time required for the induced voltage to converge to zero after the approaching object stopped. (f) As the resistance of external load increased from 1 to 20 gigohm, recovery time increased from 2.5 to 37.9 s.

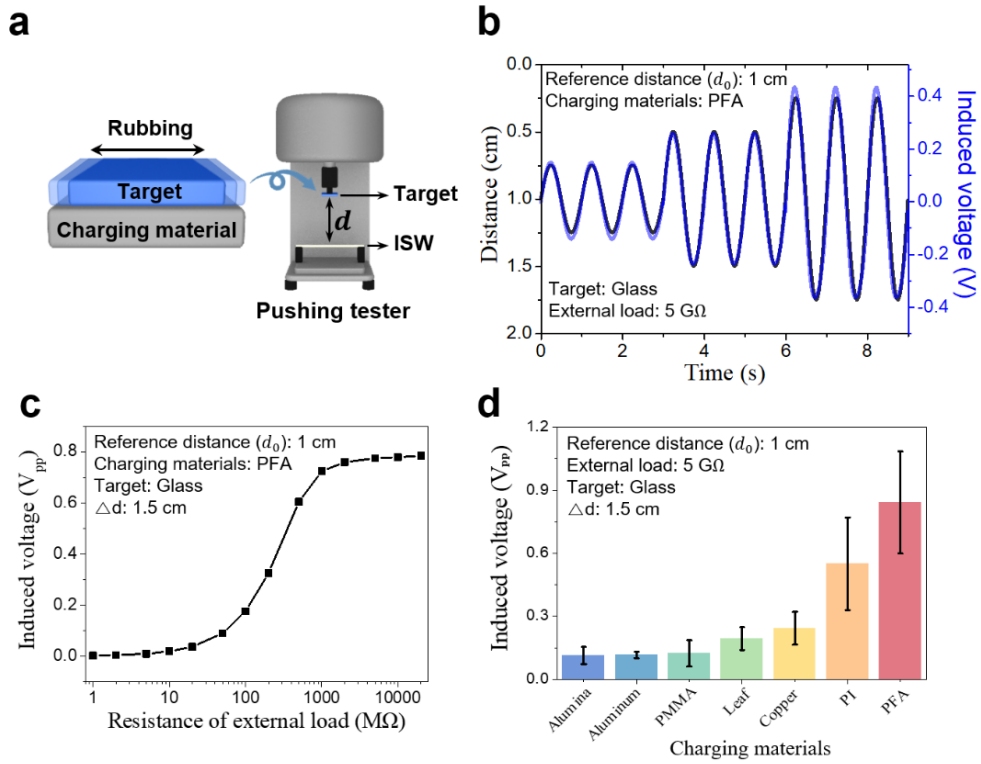


Fig. 4.12 (a) A pushing tester providing consistent control of the moving speed and gap distance for electrostatic induction sensing. (b) Induced voltage in ISWs is investigated as a function of the gap distance between an ISW and a target. (c, d) Peak-to-peak voltages induced by a glass target were measured using an external load with resistance ranging from 1 megohm to 20 gigohms (c) and various charging materials (d). Error bars represent SD ( $n = 5$ ).

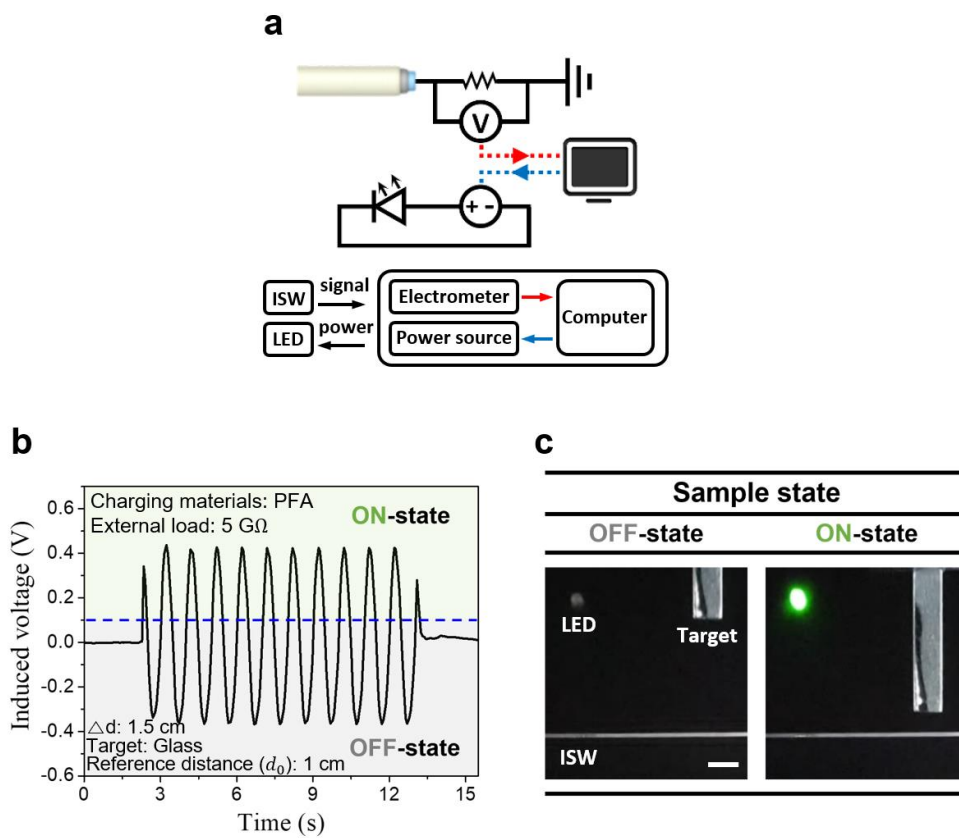


Fig. 4.13 **(a)** A block diagram showing how the ISW senses the approach of a target and then interacts with a preprogrammed computer. **(b, c)** A green LED was turned on when the induced voltage exceeded a threshold voltage (0.1 V). Scale bar, 5 mm.

#### 4.3.3. Cleaning by electrostatic vibration.

A spider can pull and release its web in a manner similar to a slingshot to clean contamination. An ISW emulates a spider's cleaning strategy to recover its capturing capability by eliminating contaminants. As shown in Fig. 4.14, vibration cleaning based on the electrostatic attraction between ISWs was proposed. In the initial state ( $V_{\text{applied}} = 0$ ), the two threads are separated (Fig. 4.14a). When a high voltage is applied, the threads attract each other by Maxwell stress (Fig. 4.14b) [86, 123]. As the applied voltage approaches zero again, the threads are released (Fig. 4.14c). Thus, alternating attraction and release caused a vibration in the ISW. When the vibration frequency matched the resonant frequency of the ISW, the vibration amplitude was maximized and contaminants could bounce off by their inertia.

The amplitude of electrostatic vibration was investigated using different frequencies of applied voltage ranging from 20 to 116 Hz, as shown in Fig. 4.15a (see Experimental section for details). When the length of the threads was 6 cm, resonance occurred at 46 Hz (mode number,  $n = 1$ ) and 92 Hz ( $n = 2$ ). When the length of the threads decreased from 6 to 3 cm, the resonant frequencies of the first and second mode increased from 46 to 97 Hz and from 92 to 195 Hz, respectively, as shown in Fig. 4.15b. Therefore, to clean ISWs of various lengths, it is necessary to sweep the entire frequency range containing all resonant frequencies. To verify the cleaning effect by vibration, recovery of the adhesion force was investigated after the surface of an ISW was sufficiently contaminated (Fig. 4.15c). During 60 s of vibration cleaning including three cycles of frequency sweeps, the adhesion force was restored to 98.7% of the initial force. Insets show the surface of the ISW before and after vibration cleaning. Compared with other contaminants, a droplet of water is more difficult to remove due to its high surface tension.

A liquid droplet hanging on a substrate can be detached when an external body force exceeds the adhesion force due to surface tension, which can be written as  $F_{ext} > \pi L \gamma \sin \theta$ , where  $L$  is the length of the contact line,  $\gamma$  is the surface tension, and  $\theta$  is the contact angle. When the vibration frequency matches the resonant frequency of the ISW, the vibration amplitude is maximized. Thus, when resonance frequency is included in the range of frequency sweep, most droplets will bounce off by their inertia [124]. However, if the detachment condition is not satisfied, not all pendant droplets are detached during the frequency sweep. The adhesion force is mitigated by increasing the contact angle, then decreasing the length of contact line via surface treatment over the silicone rubber. To clean a droplet of water by electrostatic vibration, the surface of the ISW was physically and chemically treated (see Experimental section for details). Perfluorination of ISWs using HDFs can lower surface energy [85, 108]. X-ray photoelectron spectroscopy (XPS) was implemented to characterize the functionalized ISWs (Fig. 4.15d). The spectral peak of fluorine 1s orbital was observed, confirming the presence of fluorine on the ISW after HDFs treatment. To improve the hydrophobicity of ISWs, microwrinkles were formed by air plasma treatment of prestretched ISWs (Fig. 4.18e) [125, 126]. Through HDFs treatment, the static contact angle of water was improved from 122° to 141.3°. Microscale wrinkles with a HDFs treatment maximized the static contact angle from 141.3° to 153.3° (Fig. 4.18f). Figure 4.16 shows the cleaning capabilities of pristine and surface-treated ISWs using a frequency sweep of the applied voltage. Droplets of water were initially suspended from each ISW. A droplet on a surface-treated ISW was cleaned during the vibration, whereas a droplet on a pristine ISW was not cleaned off.

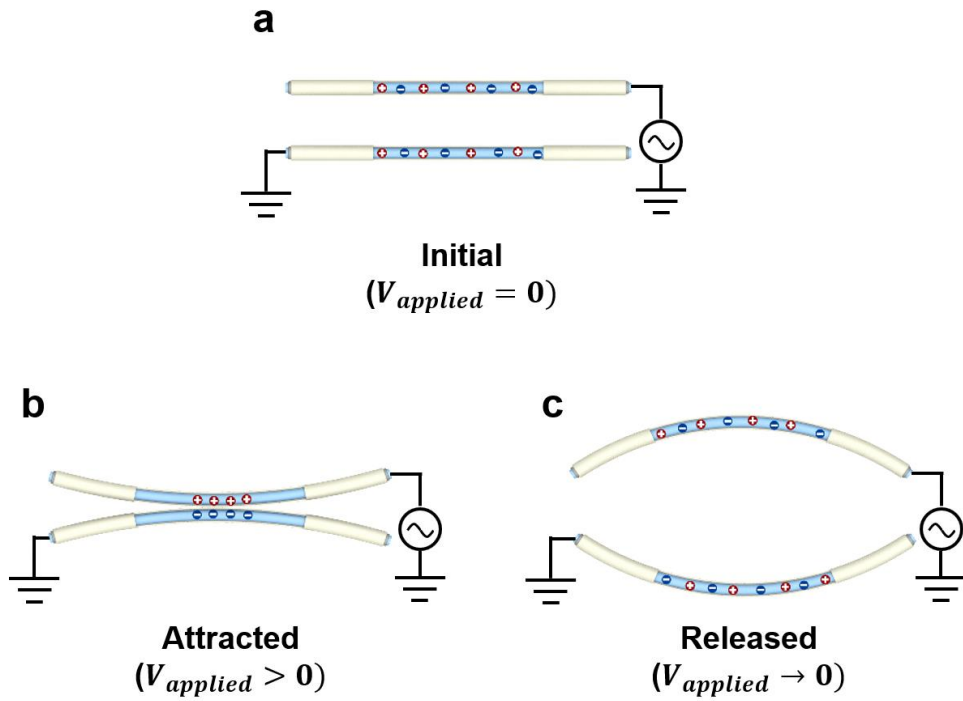


Fig. 4.14 (a-c) Schematic diagrams showing the working mechanism of electrostatic vibration cleaning in the initial (a), attracted ( $V_{\text{applied}} > 0$ ) (b), and released ( $V_{\text{applied}} \rightarrow 0$ ) (c) states.

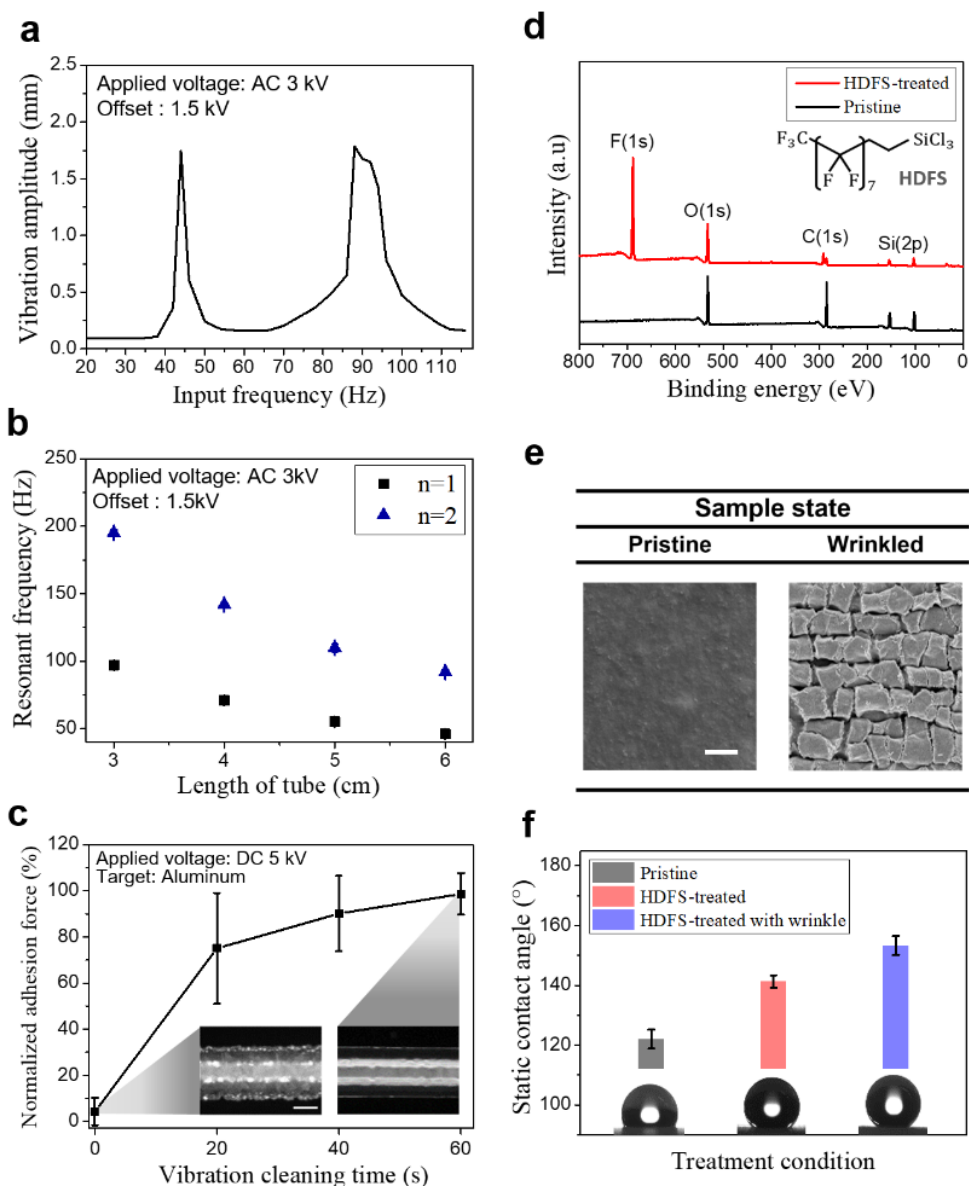


Fig. 4.15 (a) To determine a resonant frequency of the ISW, the frequency of the applied voltage was swept from 20 to 116 Hz. (b) Resonant frequencies were measured using different length threads. (c) The adhesion force of a contaminated ISW was recovered as vibration cleaning removed contaminants. Error bars represent SDs,  $n = 5$ . Scale bar, 300  $\mu\text{m}$ . (d) An x-ray photoelectron spectrometer (XPS) was used to characterize the HDFS on surfaces of ISWs. (e) Wrinkles were formed on the surface of ISWs to enhance their hydrophobicity. Scale bar, 1  $\mu\text{m}$ . (f) Static contact angles depending on surface treatment. Error bars represent SDs,  $n = 3$ .

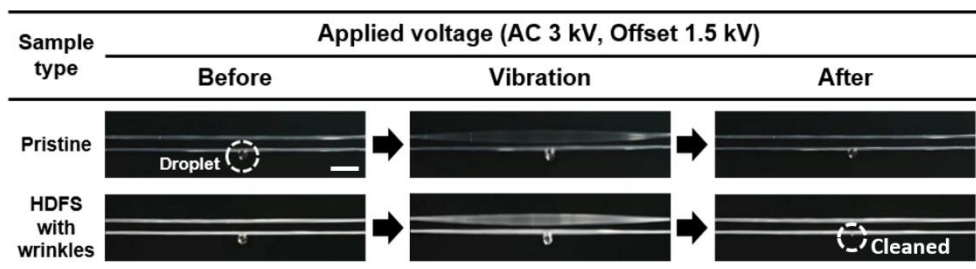


Fig. 4.16 Cleaning capabilities of pristine and surface-treated ISWs. A droplet hanging on surface-treated ISWs was removed by vibration, whereas a droplet remained on the pristine ISWs.

#### 4.3.4. Multi-functional ionic spiderweb robots.

An ISW was fabricated in the form of an orb web, as shown in Fig. 4.17a. A pair of threads was fixed on nylon threads as a framework (Fig. 17b). The distance between the pairs was 1 cm ( $d_o$ ), and the distance between threads in a pair was 3 mm ( $d_i$ ). The ISW exhibits passive camouflage in diverse environments (such as a forest, fallen leaves, a brick wall, and the floor of a building) because it is transparent and thin, as shown in Fig. 4.17c. In an attempt to enhance the adhesion force, the ISW was tilted to  $80^\circ$  from the horizontal. In the initial state, the ISW was contaminated with dust, such as polyurethane particles (Fig. 4.17d, i). During cleaning, a frequency of the applied voltage was swept from 30 to 60 Hz for 200 s, and the dust that covered the ISW was notably cleaned (Fig. 4.17d, ii). After the cleaning, the ISW was turned to sensing mode with no applied voltage. When an approaching target caused the induced voltage to exceed the threshold voltage of 1 V, the ISW was rapidly converted to capturing mode (Fig. 4.17d, iii). Various types of materials—such as a leaf (0.4 g), PMMA (3.1 g), glass (8.5 g), and aluminum (11 g)—were tightly captured by the electrostatic adhesion of the ISW (Fig. 4.17d, iv). After performing the mission, the targets were released by application of 30 Hz of AC voltage to the ISW (Fig. 4.17d, v).

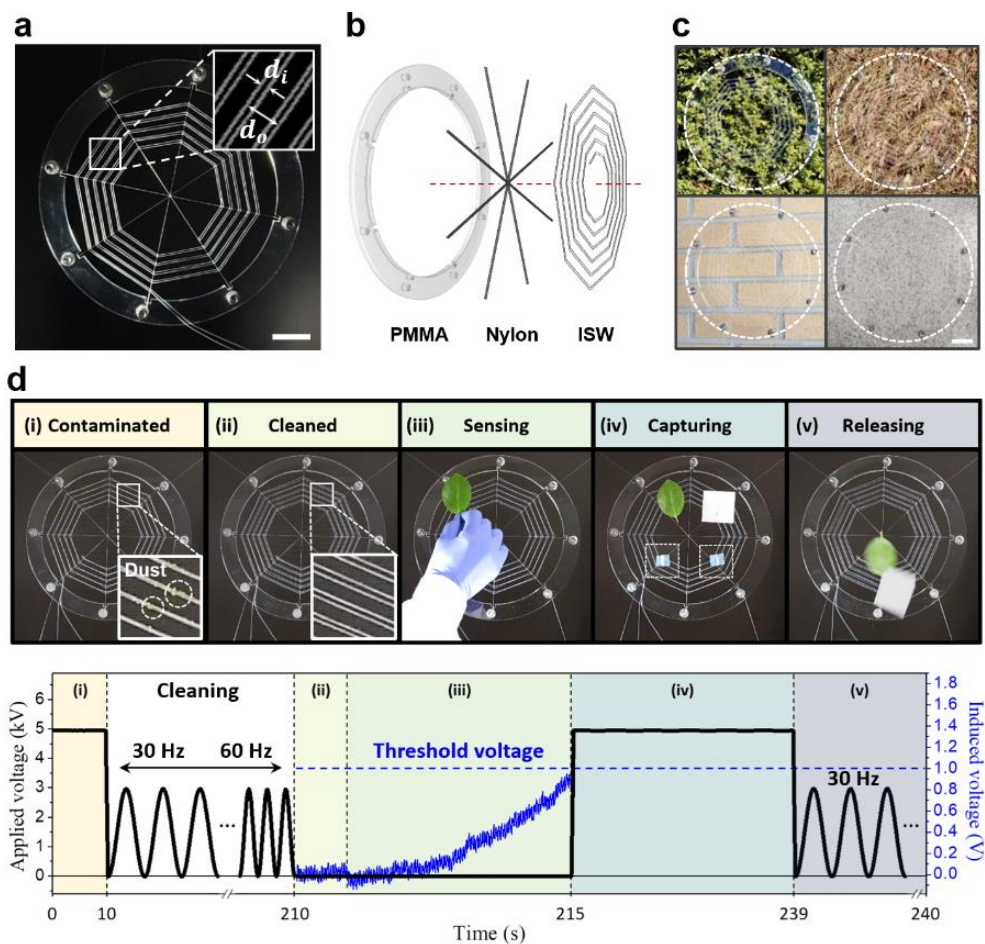


Fig. 4.17 Ionic spiderwebs. **(a, b)** ISW woven in the form of an orb web **(a)** and exploded view **(b)**. Scale bar, 3 cm. **(c)** ISWs are passively camouflaged in a variety of environment such as a forest, fallen leaves, a brick wall, and the floor of a building. Scale bar, 4 cm. **(d)** An ISW is initially covered with dust **(i)**. The dust is removed **(ii)**. The ISW senses the approach of a target and then converted to capturing mode **(iii)**. Leaf, PMMA, glass, and aluminum were sequentially captured by the ISW **(iv)**. The targets were released from the ISW **(v)**.

## 4.4. Conclusion

Inspired by how spiders capture their prey in spiderwebs, we emulate the abilities to capture, sense, and clean in our ISWs. Through electrostatics, all of these features were realized with a single pair of threads consisting of ionically conductive organogel encapsulated by a silicone rubber, which is a structure of TENGs. A potential issue of electrochemical reactions in ionic conductors was investigated in detail. The ISWs developed in this study robustly captured various types of targets, including an aluminum with a 68-fold greater mass. An ISW's stretchability enhanced its capturing capability by reducing the thickness of the silicone rubber. The sensing capability of the ISW allowed it to turn on electrostatic adhesion only when a target was nearby to avoid undesirable contamination. This contributed to the maintenance of the adhesion force, which was 32.5 times higher than that of an ISW without sensing capability. The cleaning capability of the ISW, which was reinforced by surface modifications, ensured the removal of inevitable contaminants. With electrostatic vibration cleaning, an ISW was able to recover its adhesion force up to 98.7%. Our approach is potentially applicable to other existing robotic components based on electrostatics, such as electrostatic adhesion grippers, dielectric elastomer actuators, and capacitive tactile sensors. They are expected to equip additional functionalities and broaden the scope of applications potentially without major structural changes. The proposed ISWs offer a design principle for soft robots that can achieve complementary interactions between each robotic component by emulating synergic functions of nature.

## Chapter 5. Conclusion

In this dissertation, introducing hydrogels into the research field of triboelectronics was studied to maximize the potential of TENGs and broaden the range of TENG applications. Hydrogels were highlighted as fascinating materials based on its high ion conductivity, stretchability, and transmittance to overcome the challenges of existing TENGs. Elastic solid structure and high ion solubility potentially enable hydrogels to act as promising soft ionic conductors in TENGs. Softness of hydrogels contributed TENGs to be compliantly applied on human body as wearable electronics. Based on the stretchability of hydrogels, TENGs were able to broaden the range of its application without additional modification of its structures. Furthermore, high transparency of the hydrogel allowed optical information to be transmitted through TENGs.

First, highly transparent (99.6%) and stretchable (330%) TENGs were developed by introducing hydrogels as ionic conductors into TENGs. Working mechanism of the hydrogel based TENG was suggested in detail. Potential issues of electrochemical reactions in hydrogels and relatively low hydrogel conductivity were investigated. The TENGs could be fabricated by chemically anchoring hydrogels on contact materials. Surface functionalization on the generator improved power generation and made the generator electrically and optically stable based on the self-cleaning effect. The attractive features open up exciting opportunities for TENGs as wearable electronics.

Second, soft ionic proximity sensors were demonstrated based on triboelectronics. While conventional proximity sensors have been suffered from lack of softness due to their working mechanism and structures, we suggested soft proximity

sensors by applying hydrogels and triboionics. Electric field-based working mechanism allowed the sensors to equip the through-wall sensing capability. Network of hydrogels in the sensor could detect the relative positions of nearby objects in a non-contact manner by comparing electric fields that originate from the objects. To accurately detect the relative position of an object, hydrogels were applied as shield layers to prevent electrical noise. The sensors expand the way in which humans can perceive space by providing a new sensory modality that did not evolve naturally in human beings.

Last, multi-functional ionic soft robots were demonstrated based on triboionics. Working mechanisms of each function including adhesion, sensing, and vibrational cleaning, were studied in detail to combine the mutually complementary functions into a single unit with a simple structure. All of the functions could be realized based on a structure of TENGs without additional assembly. Thanks to high stretchability of ionic conductors, the robots could be expanded to capture objects 68 times heavier than the robot. Furthermore, adhesion capability of the robots was boosted by vibrationally cleaning contamination and preventing contamination based on sensing capability. The approach pushes the boundaries of TENGs in an attempt to equip additional functions without modification of its simple structure.

## Reference

- [1] Wang, Z. L., Chen, J. & Lin, L. Progress in triboelectric nanogenerators as a new energy technology and self-powered sensors. *Energy Environ. Sci.* 8, 2250–2282 (2015).
- [2] Fan, F. R., Tang, W. & Wang, Z. L. Flexible nanogenerators for energy harvesting and self-powered electronics. *Adv. Mater.* 28, 4283–4305 (2016).
- [3] Fan, F.-R., Tian, Z.-Q. & Wang, Z. L. Flexible triboelectric generator. *Nano Energy* 1, 328–334 (2012).
- [4] Cheng, X. et al. Wearable electrode-free triboelectric generator for harvesting biomechanical energy. *Nano Energy* 12, 19–25 (2015).
- [5] Fan, X. et al. Ultrathin, rollable, paper-based triboelectric nanogenerator for acoustic energy harvesting and self-powered sound recording. *ACS nano* 9, 4236–4243 (2015).
- [6] Li, S. et al. All-elastomer-based triboelectric nanogenerator as a keyboard cover to harvest typing energy. *ACS nano* 10, 7973–7981 (2016).
- [7] Lee, Hae-Ryung, Chong-Chan Kim, and Jeong-Yun Sun. Stretchable ionics—a promising candidate for upcoming wearable devices. *Advanced Materials* 30.42 (2018): 1704403.
- [8] Larson, Christina, et al. Highly stretchable electroluminescent skin for optical signaling and tactile sensing. *science* 351.6277 (2016): 1071-1074.
- [9] C. Yang, Z. Suo, Hydrogel ionotronics, *Nat. Rev. Mater.* 3 (2018) 125.
- [10] H. Yuk, B. Lu, X. Zhao, Hydrogel bioelectronics, *Chem. Soc. Rev.* 48 (2019) 1642e1667.
- [11] J.-Y. Sun, X. Zhao, W.R. Illeperuma, et al., Highly stretchable and tough hydrogels, *Nature* 489 (2012) 133e136.
- [12] C. Keplinger, J.-Y. Sun, C.C. Foo, et al., Stretchable, transparent, ionic conductors, *Science* 341 (2013) 984e987.
- [13] A. Boydston, B. Cao, A. Nelson, et al., Additive manufacturing with stimuli-responsive materials, *J. Mater. Chem.* 6 (2018) 20621e20645.
- [14] M.C. Koetting, J.T. Peters, S.D. Steichen, et al., Stimulus-responsive hydrogels: theory, modern advances, and applications, *Mater. Sci. Eng. R Rep.* 93 (2015) 1e49.
- [15] D. Rus, M.T. Tolley, Design, fabrication and control of soft robots, *Nature* 521 (2015) 467e475.
- [16] Haight, R., Haensch, W. & Friedman, D. Solar-powering the internet of things. *Science* 353, 124–125 (2016).
- [17] Chung, J. et al. A glasses-type wearable device for monitoring the patterns of food intake and facial activity. *Sci. Rep.* 7, 41690 (2017).
- [18] Kang, D. et al. Ultrasensitive mechanical crack-based sensor inspired by the spider sensory system. *Nature* 516, 222–226 (2014).

- [19] Sun, J. Y., Keplinger, C., Whitesides, G. M. & Suo, Z. Ionic skin. *Adv. Mater.* 26, 7608–7614 (2014).
- [20] Gaikwad A. M., et al A high areal capacity flexible lithium-ion battery with a strain-compliant design. *Adv. Energy Mater.* 5, 1401389 (2015).
- [21] Wang Z. L. On Maxwell’s displacement current for energy and sensors: the origin of nanogenerators. *Mater. Today* 20,74–82 (2017).
- [22] Beeby, S. P., Tudor, M. J. & White, N. Energy harvesting vibration sources for microsystems applications. *Meas. Sci. Technol.* 17, R175 (2006).
- [23] Wang, Z. L., Chen, J. & Lin, L. Progress in triboelectric nanogenerators as a new energy technology and self-powered sensors. *Energy Environ. Sci.* 8, 2250–2282 (2015).
- [24] Fan, F. R., Tang, W. & Wang, Z. L. Flexible nanogenerators for energy harvesting and self-powered electronics. *Adv. Mater.* 28, 4283–4305 (2016).
- [25] Fan, F.-R., Tian, Z.-Q. & Wang, Z. L. Flexible triboelectric generator. *Nano Energy* 1, 328–334 (2012).
- [26] Cheng, X. et al. Wearable electrode-free triboelectric generator for harvesting biomechanical energy. *Nano Energy* 12, 19–25 (2015).
- [27] Fan, X. et al. Ultrathin, rollable, paper-based triboelectric nanogenerator for acoustic energy harvesting and self-powered sound recording. *ACS nano* 9, 4236–4243 (2015).
- [28] Li, S. et al. All-elastomer-based triboelectric nanogenerator as a keyboard cover to harvest typing energy. *ACS nano* 10, 7973–7981 (2016).
- [29] Fan, F.-R. et al. Transparent triboelectric nanogenerators and self-powered pressure sensors based on micropatterned plastic films. *Nano Lett.* 12, 3109–3114 (2012).
- [30] Khan U., Kim T. H., Ryu H., Seung W., Kim S. W. Graphene tribotronics for electronic skin and touch screen applications. *Adv. Mater.* 29, 1603544 (2017).
- [31] Chen X., et al. Tunable optical modulator by coupling a triboelectric nanogenerator and a dielectric elastomer. *Adv. Funct. Mater.* 27, 1603788 (2017).
- [32] Shin, S.-H. et al. Triboelectric charging sequence induced by surface functionalization as a method to fabricate high performance triboelectric generators. *ACS nano* 9, 4621–4627 (2015).
- [33] Zhao, X. Multi-scale multi-mechanism design of tough hydrogels: building dissipation into stretchy networks. *Soft Matter* 10, 672–687 (2014).
- [34] Darnell, M. C. et al. Performance and biocompatibility of extremely tough alginate/polyacrylamide hydrogels. *Biomaterials* 34, 8042–8048 (2013).
- [35] Qiu, Y. & Park, K. Environment-sensitive hydrogels for drug delivery. *Adv. Drug Deliv. Rev.* 53, 321–339 (2001).
- [36] Sun, J.-Y. et al. Highly stretchable and tough hydrogels. *Nature* 489, 133–136 (2012).

- [37] Keplinger, C. et al. Stretchable, transparent, ionic conductors. *Science* 341, 984–987 (2013).
- [38] Kim, C.-C., Lee, H.-H., Oh, K. H. & Sun, J.-Y. Highly stretchable, transparent ionic touch panel. *Science* 353, 682–687 (2016).
- [39] Yuk, H., Zhang, T., Parada, G. A., Liu, X. & Zhao, X. Skin-inspired hydrogel–elastomer hybrids with robust interfaces and functional microstructures. *Nat. Commun.* 7, 12028 (2016).
- [40] Gong, J. P. Materials both tough and soft. *Science* 344, 161–162 (2014).
- [41] Lee, J. H., Hinchet, R., Kim, S. K., Kim, S. & Kim, S.-W. Shape memory polymer-based self-healing triboelectric nanogenerator. *Energy Environ. Sci.* 8, 3605–3613 (2015).
- [42] Lee, K. Y. et al. Hydrophobic sponge structure-based triboelectric nanogenerator. *Adv. Mater.* 26, 5037–5042 (2014).
- [43] Im, M., Im, H., Lee, J.-H., Yoon, J.-B. & Choi, Y.-K. A robust superhydrophobic and superoleophobic surface with inverse-trapezoidal microstructures on a large transparent flexible substrate. *Soft Matter* 6, 1401–1404 (2010).
- [44] Liu M., Chen Q. Characterization study of bonded and unbonded polydimethylsiloxane aimed for bio-micro-electromechanical systems-related applications. *J. Micro/Nanolithography MEMS MOEMS* 6, 023008 (2007).
- [45] Schneider, F., Fellner, T., Wilde, J. & Wallrabe, U. Mechanical properties of silicones for MEMS. *J. Micromech. Microeng.* 18, 065008 (2008).
- [46] Zhang, X.-S. et al. High-performance triboelectric nanogenerator with enhanced energy density based on single-step fluorocarbon plasma treatment. *Nano Energy* 4, 123–131 (2014).
- [47] Kim, Y. et al. Robust superhydrophilic/hydrophobic surface based on selfaggregated Al<sub>2</sub>O<sub>3</sub> nanowires by single-step anodization and self-assembly method. *ACS Appl. Mater. Interfaces* 4, 5074–5078 (2012).
- [48] Bae, J. et al. Flutter-driven triboelectrification for harvesting wind energy. *Nat. Commun.* 5, 4929 (2014).
- [49] Han, C. B. et al. Removal of particulate matter emissions from a vehicle using a self-powered triboelectric filter. *ACS nano* 9, 12552–12561 (2015).
- [50] J. M. Loomis, R. L. Klatzky, Functional equivalence of spatial representations from vision, touch, and hearing: Relevance for sensory substitution. (2008).
- [51] N. Qian, Binocular disparity and the perception of depth. *Neuron* 18, 359-368 (1997).
- [52] J. K. D. Stephens. (Google Patents, 1968).
- [53] T. Pallejà, M. Tresanchez, M. Teixidó, J. Palacin, Bioinspired electronic white cane implementation based on a LIDAR, a tri-axial accelerometer and a tactile belt. *Sensors* 10, 11322-11339 (2010).

- [54] R. O’Keeffe et al., in 2018 IEEE 68th Electronic Components and Technology Conference (ECTC). (IEEE, 2018), pp. 533-538.
- [55] D. Tudor, L. Dobrescu, D. Dobrescu, in 2015 E-Health and Bioengineering Conference (EHB). (IEEE, 2015), pp. 1-4.
- [56] M. Bousbia-Salah, A. Redjati, M. Fezari, M. Bettayeb, in 2007 IEEE International Conference on Signal Processing and Communications. (IEEE, 2007), pp. 1003-1006.
- [57] G. Harnwell, Submarine Physics. American Journal of Physics 16, 127-139 (1948).
- [58] J. Hecht, Lidar for self-driving cars. Optics and Photonics News 29, 26-33 (2018).
- [59] C. Yang, Z. Suo, Hydrogel ionotronics. Nature Reviews Materials 3, 125 (2018).
- [60] H. R. Lee, C. C. Kim, J. Y. Sun, Stretchable Ionics—a promising candidate for upcoming wearable devices. Advanced Materials 30, 1704403 (2018).
- [61] Y. Lee, W. Song, J.-Y. Sun, Hydrogel soft robotics. Materials Today Physics 15, 100258 (2020).
- [62] X. Liu, J. Liu, S. Lin, X. Zhao, Hydrogel machines. Materials Today, (2020).
- [63] J.-Y. Sun et al., Highly stretchable and tough hydrogels. Nature 489, 133-136 (2012).
- [64] C. Keplinger et al., Stretchable, transparent, ionic conductors. Science 341, 984-987 (2013).
- [65] C. Larson et al., Highly stretchable electroluminescent skin for optical signaling and tactile sensing. science 351, 1071-1074 (2016).
- [66] J. Odent et al., Highly elastic, transparent, and conductive 3D-printed ionic composite hydrogels. Advanced Functional Materials 27, 1701807 (2017).
- [67] Y. Lee et al., Ionic spiderwebs. Science Robotics 5, eaaz5405 (2020).
- [68] Y. Lee, S. H. Cha, Y.-W. Kim, D. Choi, J.-Y. Sun, Transparent and attachable ionic communicators based on self-cleanable triboelectric nanogenerators. Nature communications 9, 1-8 (2018).
- [69] J. Y. Sun, C. Keplinger, G. M. Whitesides, Z. Suo, Ionic skin. Advanced Materials 26, 7608-7614 (2014).
- [70] C.-C. Kim, H.-H. Lee, K. H. Oh, J.-Y. Sun, Highly stretchable, transparent ionic touch panel. Science 353, 682-687 (2016).
- [71] H. Yuk, T. Zhang, G. A. Parada, X. Liu, X. Zhao, Skin-inspired hydrogel–elastomer hybrids with robust interfaces and functional microstructures. Nature communications 7, 1-11 (2016).
- [72] Q. Liu, G. Nian, C. Yang, S. Qu, Z. Suo, Bonding dissimilar polymer networks in various manufacturing processes. Nature communications 9, 1-11 (2018).
- [73] P. Le Floch et al., Wearable and washable conductors for active textiles. ACS applied materials & interfaces 9, 25542-25552 (2017).

- [74] J. Yang, R. Bai, B. Chen, Z. Suo, Hydrogel adhesion: A supramolecular synergy of chemistry, topology, and mechanics. *Advanced Functional Materials* 30, 1901693 (2020).
- [75] D. Wirthl et al., Instant tough bonding of hydrogels for soft machines and electronics. *Science advances* 3, e1700053 (2017).
- [76] A. K. Mishra et al., Autonomic perspiration in 3D-printed hydrogel actuators. *Science Robotics* 5 (2020).
- [77] T. Wallin, J. Pikul, R. Shepherd, 3D printing of soft robotic systems. *Nature Reviews Materials* 3, 84-100 (2018).
- [78] Y.-W. Kang, J. Woo, H.-R. Lee, J.-Y. Sun, A mechanically enhanced electroactive hydrogel for 3D printing using a multileg long chain crosslinker. *Smart Materials and Structures* 28, 095016 (2019).
- [79] S. C. Ligon, B. Husar, H. Wutzel, R. Holman, R. Liska, Strategies to reduce oxygen inhibition in photoinduced polymerization. *Chemical reviews* 114, 557-589 (2014).
- [80] H. Baytekin et al., The mosaic of surface charge in contact electrification. *Science* 333, 308-312 (2011).
- [81] D. Clarke, H. Whitney, G. Sutton, D. Robert, Detection and learning of floral electric fields by bumblebees. *Science* 340, 66-69 (2013).
- [82] H. H. Zakon, Electric fields of flowers stimulate the sensory hairs of bumble bees. *Proceedings of the National Academy of Sciences* 113, 7020-7021 (2016).
- [83] C.-C. Kim et al., An Implantable Ionic Wireless Power Transfer System Facilitating Electrosynthesis. *ACS nano* 14, 11743-11752 (2020).
- [84] D. Rus, M. T. Tolley, Design, fabrication and control of soft robots. *Nature* 521, 467–475 (2015).
- [85] Y. Lee, S. H. Cha, Y.-W. Kim, D. Choi, J.-Y. Sun, Transparent and attachable ionic communicators based on self-cleanable triboelectric nanogenerators. *Nat. Commun.* 9, 1804 (2018).
- [86] C. Keplinger, J.-Y. Sun, C. C. Foo, P. Rothmund, G. M. Whitesides, Z. Suo, Stretchable, transparent, ionic conductors. *Science* 341, 984–987 (2013).
- [87] C.-C. Kim, H.-H. Lee, K. H. Oh, J.-Y. Sun, Highly stretchable, transparent ionic touch panel. *Science* 353, 682–687 (2016).
- [88] J.-Y. Sun, C. Keplinger, G. M. Whitesides, Z. Suo, Ionic skin. *Adv. Mater.* 26, 7608–7614 (2014).
- [89] S. I. Rich, R. J. Wood, C. Majidi, Untethered soft robotics. *Nat. Electron.* 1, 102–112 (2018).

- [90] D. Y. Kim, S. Choi, H. Cho, J.-Y. Sun, Electroactive soft photonic devices for the synesthetic perception of color and sound. *Adv. Mater.* 31, e1804080 (2019).
- [91] C. Larson, B. Peele, S. Li, S. Robinson, M. Totaro, L. Beccai, B. Mazzolai, R. Shepherd, Highly stretchable electroluminescent skin for optical signaling and tactile sensing. *Science* 351, 1071–1074 (2016).
- [92] J. Shintake, S. Rosset, B. Schubert, D. Floreano, H. Shea, Versatile soft grippers with intrinsic electroadhesion based on multifunctional polymer actuators. *Adv. Mater.* 28, 231–238 (2016).
- [93] S. W. Cranford, A. Tarakanova, N. M. Pugno, M. J. Buehler, Nonlinear material behavior of spider silk yields robust webs. *Nature* 482, 72–76 (2012).
- [94] F. G. Omenetto, D. L. Kaplan, New opportunities for an ancient material. *Science* 329, 528–531 (2010).
- [95] R. F. Foelix, *Biology of Spiders* (Georg Thieme Verlag, 1979).
- [96] T. A. Blackledge, M. Kuntner, I. Agnarsson, in *Advances in Insect Physiology* (Elsevier, 2011), vol. 41, pp. 175–262.
- [97] L. Römer, T. Scheibel, The elaborate structure of spider silk: Structure and function of a natural high performance fiber. *Prion* 2, 154–161 (2008).
- [98] C. L. Craig, Orb-web visibility: The influence of insect flight behaviour and visual physiology on the evolution of web designs within the Araneoidea. *Anim. Behav.* 34, 54–68 (1986).
- [99] W. M. Masters, H. Markl, Vibration signal transmission in spider orb webs. *Science* 213, 363–365 (1981).
- [100] P. Fratzl, F. G. Barth, Biomaterial systems for mechanosensing and actuation. *Nature* 462, 442–448 (2009).
- [101] T. Eisner, R. Alsop, G. Ettershank, Adhesiveness of spider silk. *Science* 146, 1058–1061 (1964).
- [102] T. A. Blackledge, C. M. Eliason, Functionally independent components of prey capture are architecturally constrained in spider orb webs. *Biol. Lett.* 3, 456–458 (2007).
- [103] W. M. Barrows, The reactions of an orb-weaving spider, *Epeira scolopetaria* Clerck, to rhythmic vibrations of its web. *Biol. Bull.* 29, 316–332 (1915).
- [104] W. Nentwig, Why do only certain insects escape from a spider's web? *Oecologia* 53, 412–417 (1982).
- [105] H.-R. Lee, C.-C. Kim, J.-Y. Sun, Stretchable ionics—A promising candidate for upcoming wearable devices. *Adv. Mater.* 30, e1704403 (2018).
- [106] C. Yang, Z. Suo, Hydrogel ionotronics. *Nat. Rev. Mater.* 3, 125–142 (2018).

- [107] H. Yuk, B. Lu, X. Zhao, Hydrogel bioelectronics. *Chem. Soc. Rev.* 48, 1642–1667 (2019).
- [108] S. J. Clarkson, M. J. Owen, S. D. Smith, M. Van Dyke, M. Brook, J. Mabry, *Progress in Silicones and Silicone-Modified Materials* (ACS Publications, 2013).
- [109] D. Wirthl, R. Pichler, M. Drack, G. Kettlguber, R. Moser, R. Gerstmayr, F. Hartmann, E. Bradt, R. Kaltseis, C. M. Siket, S. E. Schausberger, S. Hild, S. Bauer, M. Kaltenbrunner, Instant tough bonding of hydrogels for soft machines and electronics. *Sci. Adv.* 3, e1700053 (2017).
- [110] M. A. Graule, P. Chirarattananon, S. B. Fuller, N. T. Jafferis, K. Y. Ma, M. Spenko, R. Kornbluh, R. J. Wood, Perching and takeoff of a robotic insect on overhangs using switchable electrostatic adhesion. *Science* 352, 978–982 (2016).
- [111] G. Gu, J. Zou, R. Zhao, X. Zhao, X. Zhu, Soft wall-climbing robots. *Sci. Robot.* 3, eaat2874 (2018).
- [112] V. Cacucciolo, J. Shintake, H. Shea, in 2019 2nd IEEE International Conference on Soft Robotics (RoboSoft) (IEEE, 2019), pp. 108–113.
- [113] J. W. Hutchinson, Z. Suo, in *Advances in Applied Mechanics* (Elsevier, 1991), vol. 29, pp. 63–191.
- [114] H. H. Zakon, Electric fields of flowers stimulate the sensory hairs of bumble bees. *Proc. Natl. Acad. Sci. U.S.A.* 113, 7020–7021 (2016).
- [115] V. M. Ortega-Jimenez, R. Dudley, Spiderweb deformation induced by electrostatically charged insects. *Sci. Rep.* 3, 2108 (2013).
- [116] F.-R. Fan, Z.-Q. Tian, Z. L. Wang, Flexible triboelectric generator. *Nano Energy* 1, 328–334 (2012).
- [117] G. Xue, Y. Xu, T. Ding, J. Li, J. Yin, W. Fei, Y. Cao, J. Yu, L. Yuan, L. Gong, J. Chen, S. Deng, J. Zhou, W. Guo, Water-evaporation-induced electricity with nanostructured carbon materials. *Nat. Nanotechnol.* 12, 317–321 (2017).
- [118] J. Nie, Z. Wang, Z. Ren, S. Li, X. Chen, Z. L. Wang, Power generation from the interaction of a liquid droplet and a liquid membrane. *Nat. Commun.* 10, 2264 (2019).
- [119] H. T. Baytekin, A. Z. Patashinski, M. Branicki, B. Baytekin, S. Soh, B. A. Grzybowski, The mosaic of surface charge in contact electrification. *Science* 333, 308–312 (2011).
- [120] M. M. Apodaca, P. J. Wesson, K. J. M. Bishop, M. A. Ratner, B. A. Grzybowski, Contact electrification between identical materials. *Angew. Chem. Int. Ed.* 49, 946–949 (2010).
- [121] M. S. Sarwar, Y. Dobashi, C. Preston, J. K. M. Wyss, S. Mirabbasi, J. D. W. Madden, Bend, stretch, and touch: Locating a finger on an actively deformed transparent sensor array. *Sci. Adv.* 3, e1602200 (2017).

- [122] Y. J. Kim, J. Lee, S. Park, C. Park, C. Park, H.-J. Choi, Effect of the relative permittivity of oxides on the performance of triboelectric nanogenerators. *RSC Adv.* 7, 49368–49373 (2017).
- [123] E. Acome, S. K. Mitchell, T. G. Morrissey, M. B. Emmett, C. Benjamin, M. King, M. Radakovitz, C. Keplinger, Hydraulically amplified self-healing electrostatic actuators with muscle-like performance. *Science* 359, 61–65 (2018).
- [124] N. M. Farhan, H. Vahedi Tafreshi, Universal expression for droplet–fiber detachment force. *J. Appl. Phys.* 124, 075301 (2018).
- [125] A. Tuteja, W. Choi, J. M. Mabry, G. H. McKinley, R. E. Cohen, Robust omniphobic surfaces. *Proc. Natl. Acad. Sci. U.S.A.* 105, 18200–18205 (2008).
- [126] A. Marmur, The lotus effect: Superhydrophobicity and metastability. *Langmuir* 20, 3517–3519 (2004).

## Abstract in Korean

전자제품이 우리 생활에 깊숙이 자리잡으며 우리 몸에 착용할 수 있는 웨어러블 디바이스에 대한 관심이 급격하게 증가해왔다. 그와 함께 웨어러블 디바이스의 응용성을 더욱 확장시키기 위해 디바이스들보다 가볍고 신축성 있게 만들기위한 노력들이 이어지고 있다. 그 중, 일상에서 발생하는 사람의 움직임을 전기에너지로 변환하여 웨어러블 디바이스의 전력원으로 이용하는 ‘디바이스의 자가발전화’에 대한 접근이 주목받고 있다.

최근, 대전과 정전기 유도 현상을 기반으로 기계적 마찰을 전기에너지로 변환하는 정전발전이 새로운 해결책으로 관심을 끌고 있다. 정전발전은 간단한 구조와 가벼운 무게, 그리고 높은 에너지 변환 효율을 앞세워 웨어러블 디바이스의 지속가능한 전력원으로 빠르게 성장하고 있다. 그와 함께 정전발전 디바이스가 인체 부착형 디바이스로 이물감 없이 적용되기 위해 정전발전 디바이스의 신축성 소재에 대한 연구 필요성이 대두되고 있다. 그간 전기적 안정성 문제로 주목받지 못하던 하이드로젤은 정전발전 분야에 신축성 소재로서 역할이 가능할 것으로 예상된다. 다량의 물로 구성된 고분자인 하이드로젤은 이온을 머금을 수 있어서 전기전도성을 떨 뿐만 아니라 탄성력을 지녀서 정전발전 디바이스의 신축성 소재로 적용될 가능성이 높게 평가된다.

이 논문에서는 하이드로젤을 정전발전 디바이스에 안정적으로 적용하여 정전발전 분야가 그간 겪던 문제들을 극복하고 정전발전 분야의 응용범위를 확장시키기 위한 방향을 제시하고자 한다. 투명하고

늘어나는 정전발전 디바이스, 소프트한 인체 부착형 근접 센서 및 다기능성 소프트 로봇 제작을 통해 하이드로젤과 정전발전의 호환 가능성에 대해 분석하고 하이드로젤 기반의 이온닉스가 정전발전 분야에 적용되었을 때 발생할 수 있는 시너지에 대해 논의할 것이다.

첫 번째 장에서는 하이드로젤을 정전발전 디바이스의 전도체 층으로 활용하여 개발한 투명하고 늘어나는 정전발전 디바이스에 대해 논의할 것이다. 적용 과정에서 발생할 수 있는 하이드로젤의 전기화학적 이슈에 대해 분석함으로써 하이드로젤과 정전발전 디바이스의 호환 가능성에 대해 제시하고 하이드로젤 기반의 정전발전 작동 메커니즘을 제시한다. 기존 정전발전 디바이스 내 절연 소재와 하이드로젤의 안정적인 결합을 위해 화학적인 접착을 하여 정전발전 디바이스의 기계적 안정성을 확보하였다. 또한 표면 코팅을 통해 정전발전 디바이스의 발전 성능을 향상시켰을 뿐만 아니라 표면 에너지를 낮추어 광학적으로도 안정한 디바이스를 제작하였다. 본 연구를 통해 정전발전 분야가 하이드로젤을 활용하여 시너지 효과를 일으키고 웨어러블 일렉트로닉스 분야에 기여할 수 있는 새로운 방향을 제시하였다.

두 번째 장에서는 기존 근접 센서의 작동 원리와 구조상 소프트해질 수 없었던 문제를 해결하기 위해 하이드로젤 소재와 정전발전 원리를 적용하여 개발한 소프트한 이온성 근접 센서에 대해 논의할 것이다. 제작된 센서는 정전발전 원리를 기반으로 하여 주변 물체의 접근을 센싱하고, 센서의 네트워크화를 통해 접근 뿐만 아니라 센서 주변 물체의 상하좌우 움직임까지 파악하였다. 정전 발전 원리상

전기장을 감지하므로 벽(부도체) 뒤에 위치한 물체 움직임까지도 센싱할 수 있었다. 또한, 전기장이 도체를 통과하지 못하는 특성에서 착안하여 하이드로젤이 전기장 쉴드로써 적용되었을 때 전기 노이즈를 차단할 수 있음을 증명하였다. 본 연구는 사람이 가지지 못한 전기장 감지 능력을 센서로 실현하여 시각에 의존할 수 없는 상황에서 사람의 인지 수단을 더욱 확장시킬 것으로 기대된다.

세 번째 장에서는 정전발전 구조에 이온성 소재를 적용하여 개발한 정전발전 기반의 센싱 뿐만 아니라, 접착, 액츄에이션까지 가능한 소프트한 이온성 다기능 로봇에 대해 논의할 것이다. 접착과 센싱, 액츄에이션의 작동 원리를 제시하였으며 각 기능들이 도출해내는 상호 보완적인 시너지 효과를 증명하였다. 센싱을 통해 오염을 예방하고 불가피한 오염은 액츄에이션을 통해 자가 세척하여 안정적인 접착능력을 유지할 수 있었다. 이온성 소재의 신축성 덕분에 로봇이 늘어난 후에는 자체 하중보다 68 배 더 무거운 물체를 들어올릴 수 있었다. 본 연구를 통해, 소프트로봇의 단순한 구조와 다기능성을 동시에 확보할 수 있는 방향을 제시함으로써 소프트로봇 분야에 끼칠 막대한 파급력이 기대된다.

**Keyword:** 정전발전, 하이드로젤, 소프트 이오닉스, 소프트 로봇

**Student Number:** 2016-33811

## 감사의 글

제가 연구했던 정전발전 디바이스는 주변 물체가 다가와 접촉을 해주어야만 작동할 수 있습니다. 제 아무리 잘 만든 디바이스도 주변 물체가 없다면 아무 쓸모 없는 디바이스입니다. 정전발전 디바이스가 주변 물체의 존재에 의해 비로소 작동할 수 있었듯이, 제 박사 학위 과정도 주변 분들에게서 많은 도움을 주신 덕분에 그 끝을 내다볼 수 있게 되었습니다. 제 4년 반 간의 성과가 담긴 박사학위 졸업 논문의 마무리를 감사한 분들과 함께하고자 합니다.

먼저, 지도교수님이신 선정윤 교수님께 감사의 말씀을 드리고 싶습니다. 지난 5년 간 평생 가져가게 될 제 연구 기반을 손이 아프도록 같이 다져주셨습니다. 교수님과 미팅 후 오피스에서 문을 닫고 나오는 길에는 항상 한없이 작아지고 아직 많이 부족하다는 생각이 들었습니다. 교수님과 같은 훌륭한 지도교수님의 지도를 받을 수 있어서 든든하고 행복했습니다. 졸업 요건이 갖추어져서 졸업은 하게 되었지만 다방면으로 여전히 배울 점이 너무 많습니다. 만약 졸업 요건에 ‘학생들을 대하는 모습은 지도교수님 만큼 가져야한다.’는 요건이 있었다면 우리 MFSM 연구실은 아마 가장 졸업하기 힘든 연구실이었을 것입니다. 5년간 항상 긍정적으로 부드럽게 대해 주셔서 감사했습니다. 학회나 타연구실에서 제 소개를 할 때 “선정윤 교수님 연구실

학생입니다”라는 말을 할 수 있어서 행복했습니다. 미래가 더 기대되는 국가대표 연구자이시자 참된 스승이신 선정운 교수님. 다시 한 번 감사드립니다.

‘연구’라는 매력에 빠질 수 있게 롤모델이 되어주신 석사과정 지도교수님 최덕현 교수님께 감사의 말씀드립니다. 진학 상담 관련하여 공대 식당에서 처음 뵙게 된 날, 교수님의 열정적인 모습에 매료되어 “그냥 교수님 따라 갈게요”라는 말이 몇 번이나 입 끝까지 차올랐었습니다. 교수님의 사람을 끌어당기는 열정적인 모습 꼭 배우고 싶습니다. 뿐만 아니라 석사과정동안 교수님의 전폭적인 지원으로 ‘정전발전 분야의 중심에서 연구한다’는 자부심을 가질 수 있었습니다. 그 덕분에 석사과정 동안 공부한 것들을 박사과정에서 잘 활용할 수 있었습니다. 경희대학교 기계공학과 최덕현 교수님 연구실에서 공부했다는 것이 어디를 가든 자랑스러웠습니다. 제가 꿈을 꿀 수 있게 시작부터 지금까지 이끌어주고 계신 최덕현 교수님. 감사합니다.

지난 박사과정 동안 가장 많이 배운 곳은 강의실도, 교수님 오피스도 아닌 연구실이었던 것 같습니다. 빠르게 자리 잡을 수 있게 도와주신 선배들께 감사드리며 가르쳐줄 것보다 배울 점이 더 많았던 후배들에게 감사의 말씀을 드립니다. 랩멤버들이 없었다면 구멍 뱅뱅 뚫린 박사학위논문을 가지고 만족스러워하고 있었을 것입니다. 연구실 멤버들을 떠올려보면 다들 어느 한 방면으로는 꼭 특출 난 점이 있는

훌륭한 사람들인 것 같습니다. 그런 멤버들과 같은 소속으로 있다는 것이 저를 더 열심히 하게끔 자극해 주었고 부족한 제 능력을 돌아보게 만들어 주었습니다. 추억 메이트이자 비밀스런 남자 석현이형, 걸바속속 진우형, 잔소리가 그리운 총찬이형, 성실함의 끝판왕 용우형, 우리 연구실이 바이오 연구도 할 수 있게 고생해준 정박사님, MFSM 의 시작 해령이, 차근차근 조용하게 강한 도운이, 오랜 시간 함께하진 못했지만 각자의 길에서 더 잘하고 있을 재성이, 현희, 상욱이, 세상이 깨끗해지는 순수함 성수형, 넘치는 끼 감추느라 고생 많은 진우(박), 두 소속으로도 힘들 텐데 열심히 하고 있는 혜원이 재호, 막차메이트 용우(강), 나보다 남을 생각할 줄 아는 순한 보물 순보, 저 세상 창의력을 가진 재만이, MFSM 간판 현욱이, 천재현재, 나의 부족한 백그라운드를 한없이 채워준 원준이, 삼성우먼 미지, 짧았지만 뒷자리에서 함께했던 수호형, 밤의 사나이 기민이, 더 친해지고 싶은 호준이형, 민규는 ...?, 뭐든 열심히 하는 모습이 멋있는 윤혁이, 연구도 수업도 열심히 임하는 솔지, MFSM 의 뒤를 봐줄 법조인 인혁이, 꾸준한 모습이 멋있는 창서, MFSM 을 이끌어갈 마가, 성유, 시환이. 모두들 감사했습니다. 우리 MFSM 멤버들과 함께한 날들을 돌아보고 앞으로 함께할 날들을 그려보면 무서울 게 없을 것 같습니다.

마지막으로, 가족들에게 감사의 말씀을 드리고 싶습니다. 항상 저를 믿고 제 선택을 따라 주시는 아버지. 아버지의 교육 덕분에 항상 오만을 경계할 수 있었고 선택 하나하나를 허투루 할 수 없었습니다.

연구의 많은 아이디어들을 낼 수 있었던 것도 항상 뭐든 찾아서 공부하시는 아버지의 영향을 받은 것 같습니다. 한평생 가족들 뒷바라지 해주시는 어머니. 어머니 덕분에 제가 이렇게 건강할 수 있었고 뒷받침된 체력으로 서울대에서도 뒤쳐지지 않고 성실하게 열심히 할 수 있었습니다. 일을 손에서 놓지 않으시는 어머니를 보며 저도 성실해질 수 있었던 것 같습니다. 감사합니다. 우리 가족을 생기 있게 꾸며주는 큰누나, 작은누나, 그리고 항상 든든한 매형들. 감사합니다. 누나들과 매형들 덕분에 제 일에 더 집중할 수 있었습니다. 저는 우리 가족들이 도와주신 결과로 가족들을 대표해서 학위를 받는 것 같습니다. 감사합니다. 곧 인생의 반려자가 될 가영이. 항상 내 편이 되어주고 연구가 잘 되든 안되든 옆에서 자기 일처럼 희로애락을 같이 해줘서 고마웠습니다. 가영이 아버님, 어머님에게도 항상 응원 해주셔서 감사하다는 말씀드리고 싶습니다. 다시 한번 모든 분들께 감사드리며 앞으로 받은 도움들을 어떻게 되돌려드릴 수 있을지 고민하며 살아가도록 하겠습니다. 감사합니다.

2021년 1월

이영훈 올림.